Surface-Enhanced Raman Spectroscopy as a Probe to Understand Plasmon-Mediated Photochemistry

A DISSERTATION

SUBMITTED TO THE FACULTY OF THE

UNIVERSITY OF MINNESOTA

BY

James L. Brooks

IN PARTIAL FULFILLMENT OF THE REQUIREMENTS

FOR THE DEGREE OF

DOCTOR OF PHILOSOPHY

Advisor

Renee R. Frontiera

September 2019

Acknowledgements

During my time at the University of Minnesota, I have been constantly surrounded by support from my mentors, colleagues, friends, and family, to whom I have many thanks to give.

First and foremost, I am grateful to have worked for my advisor, Renee Frontiera. Renee, thank you for accepting someone who knew very little about spectroscopy into your research group. Thank you for the non-stop support and inspiration - you have a special skill of motivating your students during both times of success and failure. You have taught me how to carefully critique my research, which is something I will continue to carry with me throughout my professional career.

I would like to acknowledge and sincerely thank all of my colleagues from the Frontiera Lab. This work would not have been possible without all of the conversations, apple fritters, and laughs we shared. I am fortunate that you all put up with my endless sarcasm and countless bad jokes. It is clear that the future of this group is bright, and I cannot wait to see all of your accomplishments in the coming years.

To my friends, thank you for being a reliable source of enjoyment and entertainment. From playing card/board/video games to simply getting drinks together during happy hour, I will forever be grateful for our shared experiences.

Nobody has been more important to the pursuit of my doctoral degree than my family. I cannot begin to express my thanks to my parents, who have constantly provided unwavering support and love during every step of this educational journey. Drew and

Elizabeth, I am grateful for our relationships and thank you for always being a stable outlet for fun. Lastly, Beth, I cannot thank you enough for your endless kindness, inspiration, and love the past few years - I cannot wait to start our next adventure together in Texas.

Abstract

The development of plasmonic nanostructures as light-activated photocatalysts has proven to be a promising research avenue due to their ability to access and drive unfavorable chemical reactions. Theses chemical reactions are fueled by the presence of surface plasmons, which are the collective oscillation of the free electron density on the material's surface. Once a surface plasmon is photoexcited, their initial energy rapidly decays into multiple different pathways, such as enhanced electromagnetic fields, an abundance of hot carriers, and dramatically elevated local thermal environments. To better understand the various chemistries that are enabled by plasmonic materials and the associated mechanisms driving these processes, we have employed surface-enhanced Raman spectroscopy to interrogate a plethora of plasmon-molecule coupled systems.

Our initial studies investigated the relationship between the plasmonic local fields and a well-established plasmon-driven photochemical reaction. We found that there were no observable correlations between the two in our studies and identified a competing degradation pathway for the studied analytes. In addition to exploring well-studied plasmon-induced chemical photoreactions, we have highlighted two new reactions that were accessed on the gold film-over-nanosphere substrates. First, we were able to induce and subsequently monitor a selective intramolecular methyl migration on N-methylpyridinium using surface-enhanced Raman spectroscopy. This work emphasizes the growing potential of initiating highly-selective chemistries with plasmonic materials for synthetic or redox purposes. The second previously unreported plasmon-driven reaction involves the double cleavage of the C-N bond on a pair of viologen derivatives. While these viologens have traditionally been employed as robust redox species, the unique and highly-powerful plasmonic local fields allowed the viologens to access an entirely new reaction pathway to transform into 4,4’-bipyridine.

Lastly, we discuss our experimental approaches towards transiently studying the mechanism behind plasmon-mediated hot electron transfer. Using ultrafast surface-enhanced Raman spectroscopy, we interrogated the transient dynamics that occurred between surface plasmons and a bevy of electron accepting chemical adsorbates. Ultimately, the primary goal of this work is to provide a quantitative description of the transient interactions, which will assist in increasing the reported efficiencies and yields of plasmon-mediated chemical reaction and inspire the rational design of plasmonically-powered devices.

Table of Contents

List of Tables

Chapter 2: Toward a Mechanistic Understanding of Plasmon-Mediated Photocatalysis

List of Figures

Chapter 2: Toward a Mechanistic Understanding of Plasmon-Mediated Photocatalysis

Chapter 3: Competition Between Reaction and Degradation Pathways in Plasmon-Driven Photochemistry

Chapter 4: Plasmon-Mediated Intramolecular Methyl Migration

Chapter 5: Plasmon-Driven C-N Bond Cleavage Across a Series of Viologen Derivatives

Chapter 6: Ultrafast Surface-Enhanced Raman Spectroscopy to Study Hot Electron Transfer in Plasmonic Materials

Chapter 7: Prospects

Appendix A: Supporting Information for Manuscript: Competition Between Reaction and Degradation Pathways in Plasmon-Driven Photochemistry

Appendix B: Supporting Information for Manuscript: Plasmon-Mediated Intramolecular Methyl Migration

Appendix C: Supporting Information for Manuscript: Plasmon-Driven C-N bond Cleavage Across a Series of Viologen Derivatives

Appendix D: Supporting Information for Chapter 6: Ultrafast Surface-Enhanced Raman Spectroscopy to Study Hot Electron Transfer in Plasmonic Materials

List of Abbreviations

4-ATP	4-aminothiolphenol
4-MP	4-methylpyridine
4-NBT	4-nitrobenzenethiol
ALD	atomic layer deposition
AlNC	aluminum nanocrystal
AuFON	gold film-over-nanospheres
AuNP	gold nanoparticle
AuNR	gold nanorod
BPE	*trans*-1,2-bis(4-pyridyl)ethylene
BPY	4,4’-bipyridine
BV	benzyl viologen
CV	cyclic voltammetry
DMAB	4,4’-dimercaptoazobenzene
EF	enhancement factor
EV	ethyl viologen
FRET	Förster resonance energy transfer
HDD	hard disk drive
LSPR	localized surface plasmon resonance
MV	methyl viologen

NIR	near infrared
NMP	n-methylpyridinium
NOPA	non-colinear optical parametric amplifier
OKE	optical Kerr effect
PICTT	plasmon-induced metal-to-semiconductor interfacial charge transfer transitions
PIRET	plasmon-induced resonance energy transfer
pMA	*p*-mercaptoaniline
SE-CARS	surface-enhanced coherent anti-Stokes Raman spectroscopy
SECM	scanning electrochemical microscopy
SE-FSRS	surface-enhanced femtosecond stimulated Raman spectroscopy
SERS	surface-enhanced Raman spectroscopy
SM-SERS	single molecule surface-enhanced Raman spectroscopy
STM	scanning tunneling microscopy
TA	transient absorption
TCNQ	tetracyanoquinodimethane
TERS	tip-enhanced Raman spectroscopy
TiNFON	titanium nitride film-over-nanospheres

Chapter 1

Introduction

1.1 Motivation

The recent development of plasmonic materials as light-activated photocatalysts has proven to be promising due to their ability to drive unfavorable chemical reactions. Plasmon-mediated photochemistry relies on the presence of surface plasmons to generate highly localized fields,[1-2] hot electrons and holes,[3-4] dramatically elevated thermal environments,[5-7] and/or modified potential energy surfaces.[8-9] Significant progress has been made in recent years towards successfully using plasmonic materials as a tunable solar-driven photocatalytic device.[10-13] However, while there has been a concerted effort towards accessing industrially-relevant plasmonically-powered catalytic reactions, the corresponding efficiencies and yields have been suboptimal. To fully realize the true potential of plasmonic materials, we believe that the plasmonics community needs to collectively develop a better understanding of the underlying mechanisms fueling plasmonic photocatalysis.

One of the more encouraging applications of plasmonic materials is their aptitude to achieve a high-level of chemical selectivity when inducing certain chemical reactions.[14-16] It is our belief that further expanding upon the list of accessible selective plasmon-mediated chemical reactions is of high importance. While there have been recent advances in plasmon-mediated selective chemistry, there is still a substantial lack of precedent in using plasmonic photocatalysts as an alternative tool to carry out relevant synthetic or redox chemistries with a high level of selectivity.

To provide a more detailed understanding of these plasmonically-powered processes, we believe that approaching them from a molecular perspective may prove fruitful. Surface-enhanced Raman spectroscopy (SERS) is a vibrationally selective technique that exploits the fundamental principles of plasmonics, as it is intimately dependent on the local fields produced by the plasmonic materials.[17] SERS is capable of spectroscopically monitoring the structure of a chemical adsorbate as it undergoes a plasmon-mediated transformation. As the reaction proceeds, the resulting SER spectra contains a bevy of information related to the reactant and corresponding photoproduct.[18-20] Throughout this thesis, we have employed SERS as our definitive experimental method to initiate and spectroscopically characterize both well-studied and unreported plasmon-mediated reactions.

Additionally, to further understand the underlying transient mechanism behind a hot electron-driven photochemical reaction, we have employed ultrafast SERS to interrogate plasmonic systems. Ultrafast SERS is an ultrafast pump-probe Raman technique that collects an evolving molecular fingerprint during a pico- to femtosecond timescale.[21] Theoretically, this experimental technique will be capable of tracking the hot electrons as they transfer to a targeted molecule, generating a transient anionic intermediate species. With a better understanding of the transient hot electron transfer mechanism, the plasmonic community can begin to achieve a rational design of plasmonically-powered photocatalysts.

1.2 Outline

Throughout this thesis, we have provided a detailed description of our attempts of using both steady-state and ultrafast SERS to better understand plasmon-mediated photochemical reactions.

Chapter 2 is an extensive review discussing the present-day state of plasmon-mediated catalysis. We highlight the note-worthy findings in the field and provide a detailed commentary on where the collective understanding is most lacking. Furthermore, we provide a robust description of the multiple experimental approaches being used to develop a detailed mechanistic description of plasmon-driven catalytic reactions.

In Chapter 3, we used SERS to examine the relationship between the local electric fields found in plasmonic materials and their ability to drive a well-studied photochemical dimerization reaction. We found that there was no observable correlation between the local field's intensity and the reaction's rate. Additionally, there was a direct competition between the photoreaction pathways with a destructive photodegradation pathway. The results in this work highlight the importance of carefully considering the relevant rates and accessibility of the various photoinduced processes when initiating plasmonic chemical conversions.

Chapter 4 discusses our work towards using SERS to mediate a new selective chemical reaction on plasmonic materials. Specifically, we were able to induce an intermolecular methyl migration on N-methylpyridinium to form 4-methylpyridine on a gold film-over-nanosphere substrate. This work further demonstrated the untapped potential of using plasmonic materials as a means to carry out selective synthetic and/or redox reactions and serves as an additional contribution to the repository of plasmon-mediated chemical reactions.

Our work presented in Chapter 5 introduces an unreported plasmon-driven N-bound substitute cleavage on viologen derivate. With SERS, we were able to spectroscopically observe the formation of 4,4’-bipyridine. Here, by introducing the viologen derivatives to the unique local fields provided by plasmonic gold film-over-nanospheres, we were able to access an entirely new reaction pathway for the viologen species.

In Chapter 6, we shift our focus towards employing ultrafast SERS to transient track the generation of hot electron-induced intermediate species. We detail our pump-probe spectroscopic attempts towards studying this ultrafast phenomenon and provide a brief discussion pertaining to the transient photophysical responses we saw in the plasmon-molecule systems that we experimentally interrogated.

Lastly, in Chapter 7 we provide a discussion on promising experimental modifications that may prove to be instrumental for advancing the work presented in Chapter 6. Here, we introduce our attempts of developing a modified sample holder that is capable of rapidly displacing our non-solution phase substrates during an ultrafast SERS experiment. Additionally, we present our preliminary work towards the development of an alternative titanium nitride film-over-nanosphere substrate for ultrafast surface-enhanced Raman spectroscopic measurements.

Chapter 2

Toward a Mechanistic Understanding of Plasmon-Mediated Photocatalysis

Reprinted with permission from the manuscript by James L. Brooks, Emily L. Keller, Christopher L. Warkentin, Dayeeta Saha, and Renee R. Frontiera *Nanophotonics* 2018, 7(11), 1697-1724

2.1 Overview

One of the most exciting new developments in the plasmonic nanomaterials field is the discovery of their ability to mediate a number of photocatalytic reactions. Since the initial prediction of driving chemical reactions with plasmons in the 1980s, the field has rapidly expanded in recent years, demonstrating the ability of plasmons to drive chemical reactions, such as water splitting, ammonia generation, and CO_2 reduction, among many other examples. Unfortunately, the efficiencies of these processes are currently suboptimal for practical widespread applications. The limitations in recorded outputs can be linked to the current lack of a knowledge pertaining to mechanisms of the partitioning of plasmonic energy after photoexcitation. Providing a descriptive and quantitative mechanism of the processes involved in driving plasmon-induced photochemical reactions, starting at the initial plasmon excitation, followed by hot carrier generation, energy transfer, and thermal effects, is critical for the advancement of the field as a whole. Here, we provide a mechanistic perspective on plasmonic photocatalysis by reviewing select experimental approaches. We focus on spectroscopic and electrochemical techniques that provide molecular-scale information on the processes that occur in the coupled molecular-plasmonic system after photoexcitation. To conclude, we evaluate several promising techniques for future applications in elucidating the mechanism of plasmon-mediated photocatalysis.

2.2 Introduction

The growing necessity for clean and renewable forms of energy production has had a significant effect on developing new technologies capable of achieving environmentally-conscious and energetically-efficient methodologies for driving industrial catalytic reactions. Photocatalysis, which relies on harvesting an abundance of photons from an external source, has been repeatedly demonstrated as a plausible option for driving energetically-demanding chemical reactions. The concept of directly converting solar energy to chemical energy has proved promising, as it negates the need of devoting a high amount of electrical or other forms of energy to carry out the process.[22] Initially, the groundbreaking research performed by Fujishima and Honda in 1972 ushered in a wave of studies focused on implementing semiconducting materials for solar-driven photocatalysts.[23] However, semiconducting materials generally absorb in the ultraviolet, a relatively inefficient region in the solar spectrum, and despite extensive research, photoconversion efficiencies have remained below the limit needed for widespread application. Present day catalyst design has been focused on implementing materials capable of harvesting the most abundant region of the solar spectrum, the visible region.[24] Still, the current options for photocatalysts leave much to be desired regarding their efficiencies and energetic demands that are required to power them.

In the development of industrially-relevant photocatalytic processes, challenges impeding their progress must be considered. Many of the desirable catalytic processes have large energetic barriers, require the transfer of multiple electrons, and frequently require bimolecular collisions on the catalyst surface. Therefore, these reactions typically require high temperature, high pressure, and lots of time to produce desired products. For example, steam methane reforming, a key method in hydrogen production and the Fischer-Tropsch process, is highly endothermic and requires reaction conditions exceeding 1000 K at high pressure (15-30 atm).[25] Other key industrial catalytic reactions require high specificity to produce products with high purity, as in the hydrogenation of acetylene to ethylene, a key feedstock for many industrial products. In addition to meeting strict reaction conditions, the scale of such processes must continually rise to meet increasing global demands. **Table 2.1** provides a glance at the relative scale of several important industrial catalytic processes, which reflects the vast amount of capital invested in the development of the necessary infrastructure for their implementation. In view of these challenges, for photocatalytic processes to be competitive with standard industrial practices, highly efficient and robust catalysts that can maintain their catalytic activity under harsh reaction conditions are required. The application of photocatalytic processes will likely require integration into existing infrastructure and must prove to be financially viable at large scales to be competitive and comply with ever expanding global consumer demands. Additionally, significant research effort has been directed toward implementing photocatalysts into energy-demanding situations that don't require mass scale production. For example, photocatalysts have the potential to be utilized in the production of electricity on an individual household scale. Regardless, the development of plasmonic photocatalysts could eventually leave a dramatic impact on both large- and small-scale catalytic processes.

Table 2.1 List of plasmon-mediated industrially-relevant catalytic processes

Process	Endo/Exo	Standard Catalyst	Approx. Production Scale (Megaton per year)	Plasmon-mediated (Prominent Catalyst)
Acetylene Hydrogenation	Exothermic	Pd/Al_2O_3	N/A	Yes, AlNC-Pd NP [14]
Haber-Bosch Process (Ammonia Generation)	Exothermic	Fe/K_2O	200 [26]	Yes, Au NP coupled systems [27,28]
Reverse Water-Gas Shift Reaction	Endothermic	Cu	N/A	Yes, Au NP/TiO_2[16]
Steam Methane Reforming	Endothermic	Ni/Al_2O_3	215 (H_2) [29, 30]	Yes, Au-Pt NP [31]
Water Electrolysis	Endothermic	Ni & Pt	20 (H_2) [30]	Yes, Au NR/TiO_2[10]

Significant progress has been made in the recent years towards the application of plasmonic materials as catalysts for driving chemical reactions, highlighted by examples in **Table 2.1**.[5, 10, 14, 16, 27-28, 31-36] These materials are considered promising candidates for driving highly selective chemical processes due in part to their ability to host surface plasmons. The extinction spectrum of a plasmonic material can be finely tuned to match the output of the solar spectrum by changing the size or shape of the nanomaterial. Plasmonic materials harvest energy from resonant photons and partition it into multiple different pathways. Once generated, the surface plasmon produces highly enhanced localized electromagnetic fields, creates elevated thermal environments, ejects highly energetic hot carriers, and/or modifies the potential energy landscape of a nearby molecular species.[37-39] Each of these possible pathways of energy partitioning may contribute to mediating a catalytic process, with the preferential pathway heavily dependent on the targeted chemical reaction and the plasmonic substrate's design. Due to the complexity of these potential pathways, designing a plasmonic system capable of achieving optimal turnover numbers and yields is a non-trivial task. Ultimately, to make a significant leap in device fabrication, in the absence of an unpredicted technological development, it is imperative to study the individual mechanistic contributions and dynamics during the energy transformation post plasmon excitation. With this highly pertinent information in hand, plasmonic substrates may be designed to preferentially dictate the flow of energy as the surface plasmon decays and efficiently channel it into mediating a chemical reaction. Herein, we have thoroughly discussed and reviewed the leading spectroscopic and electrochemical techniques used to explore the mechanism behind plasmon-mediated photocatalysis.

One of the most promising aspects of plasmon-mediated photocatalysis is the ability to achieve a high level of chemical selectivity. Chemical selectivity is used to quantify how successful a given catalytic system is at producing the desired product over undesired byproducts. In many commercial catalytic systems, the chemical selectivity of the catalyst can be quite poor due to the existence of a number of competing chemical processes, requiring expensive separation processes. However, plasmonic materials are suitable materials for achieving high selectivity as compared to most thermally-activated catalytic processes, as they may be specifically designed to selectively generate charge carriers containing the required energies.[14] It is crucial to employ a system capable of producing highly-selective products to reach a level of optimization for achieving practical applications of plasmonic photocatalysts. Once fully optimized, one can envision the prospect of a tunable solar-driven photocatalytic device capable of selectively driving a wide range of chemical reactions.

Throughout this review, we have provided a discussion and critique of the current literature that is focused on studying plasmon-mediated photocatalysis from a molecular viewpoint. Probing the interactions between strongly coupled molecule-plasmon systems may help provide a beneficial insight into better understanding the non-trivial mechanism driving fundamental plasmonic processes. While a singular technique may not entirely provide a definitive description of plasmon-molecule interactions on its own, the collective knowledge garnered from various experimental approaches may produce a cohesive picture of how surface plasmons and molecules behave as the plasmon decays, leading to a rational design of highly optimized and selective plasmonic photocatalysts.

The goal of this review is to provide a narrative centralized on highlighting the capabilities and future promise of a number of advanced experimental methods employed to study the transient energetic dynamics of plasmonic materials and their effect on mediating catalytic processes. Ultimately, we aim to recognize the current challenges found in the field of plasmon-mediated photocatalysis, to discuss the notable scientific efforts to better understand the interactions between plasmons and molecules, and to provide an evaluation on the future landscape for applied plasmonic photocatalysts. We begin with a review of the relevant plasmon dynamics and possible energetic decay pathways, highlight a number of exceptional experimental studies that were successful in further explaining the intricate details found in plasmonic systems, and conclude with an outlook on the future of plasmon-mediated photocatalysis.

2.3 Fundamentals of Plasmon Generation and Decay

2.3.1 Surface Plasmons

Plasmons are the collective oscillation of the free charge density within a material with negative real and small positive imaginary dielectric components, which include materials such as gold, silver, aluminum, titanium nitride,[40] metal oxides,[41] and copper chalcogenides,[42] among a growing list of many others. Surface plasmons are confined to the surface of nanostructured materials.[43] After photoexcitation, the free electron charge density begins to oscillate at the surface of the plasmonic material, leading to the focusing of the far-field radiation to highly localized and dramatically-enhanced nanoscale electromagnetic fields. Materials that support surface plasmons have the ability to amplify an electromagnetic wave from free space within an effective volume well below the diffraction limit,[44] allowing for a wide-range of applications, including fueling photocatalytic reactions,[5, 10, 14, 32-35, 45-47] increasing the efficiency of photovoltaics,[48-54] and serving as vehicles for photothermal therapy.[55-61]

2.3.1.1 Plasmonic Energy Partitioning

A coherent surface plasmon can be generated by introducing an incident photon source that is on-resonant with the nanoparticle's extinction spectrum. The wavelength of light used to interact with the particles is much larger than the size of the material itself and produces a coherent oscillation of the electron density locally confined to the nano-sized particle. After the surface plasmon has been photoexcited, its energy may rapidly decay through either radiative or non-radiative pathways. The surface plasmon only maintains its

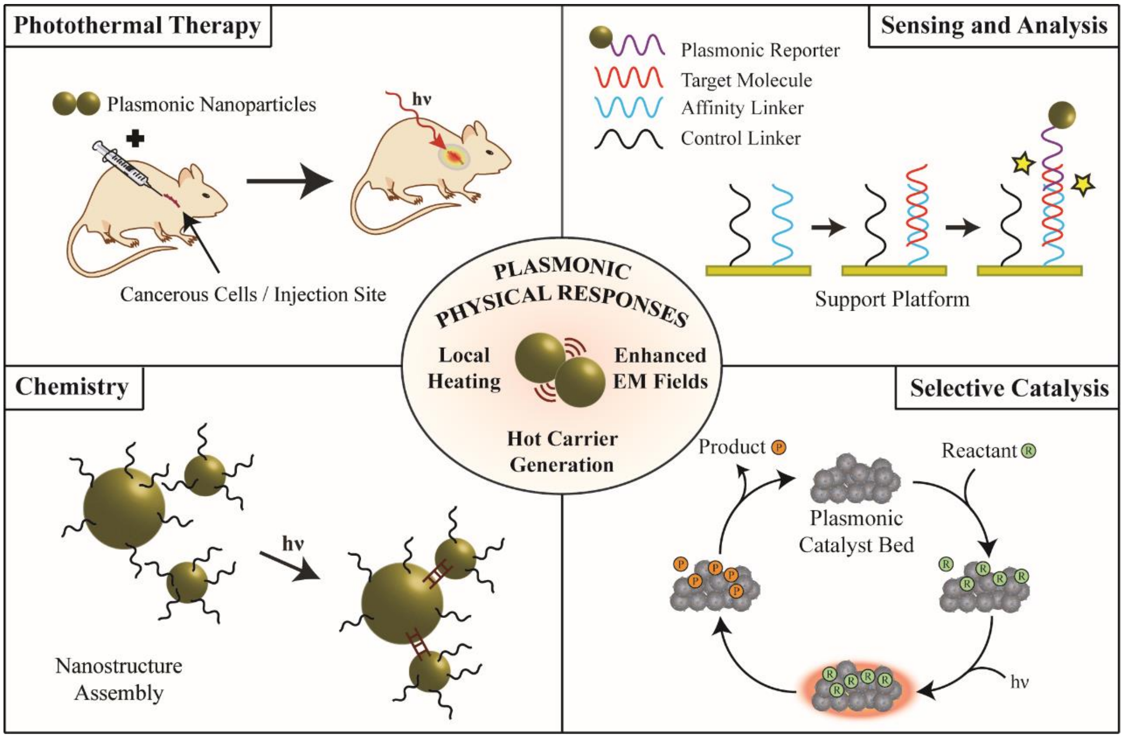

Figure 2.1 Present-day applications for plasmonic materials. (Top left) Plasmonic nanoparticles have been employed to target cancerous cells within live organisms. Once photoexcited, the plasmonic energy is intentionally converted into a thermal energy to annihilate the targeted cells. (Top right) Sensing platforms constructed with plasmonic materials are used to detect specific analytes at an ultra-low concentration. (Bottom left) Nano-level architectural design can be achieved by inducing chemical reactions that link two or more individual nanoparticles to assemble a new plasmonic structure. (Bottom right) Plasmonic nanostructures are capable of mediating highly-selective catalytic processes.

coherence for 1-10 fs and begins to convert its energy into multiple pathways as it decays.[62] However, depending on the substrate's composition, shape, and size, multiple distinct chemical and physical processes may be triggered as the plasmon relaxes. The following sections will detail the various decay pathways the plasmon may undergo as it loses coherence and relaxes. Once the plasmonic energy is dispersed through the preferential pathways, the energy can be used to power a plethora of applications (**Figure 2.1**).

2.3.1.2 Enhanced Electromagnetic Fields

Surface plasmons give rise to dramatically enhanced electromagnetic fields near the surface of the nanostructure.[44] The plasmonic nanoparticles can be specifically engineered to host various nanoscale physical structures that allow for extreme light concentration to subwavelength dimensions, resulting in highly localized electric fields. Resonant interactions between the oscillating free electron density near the surface of the nanostructure and the incident electric field produce these exponentially decaying fields. The regions of amplified electromagnetic fields, typically form between the crevice of two or more physical

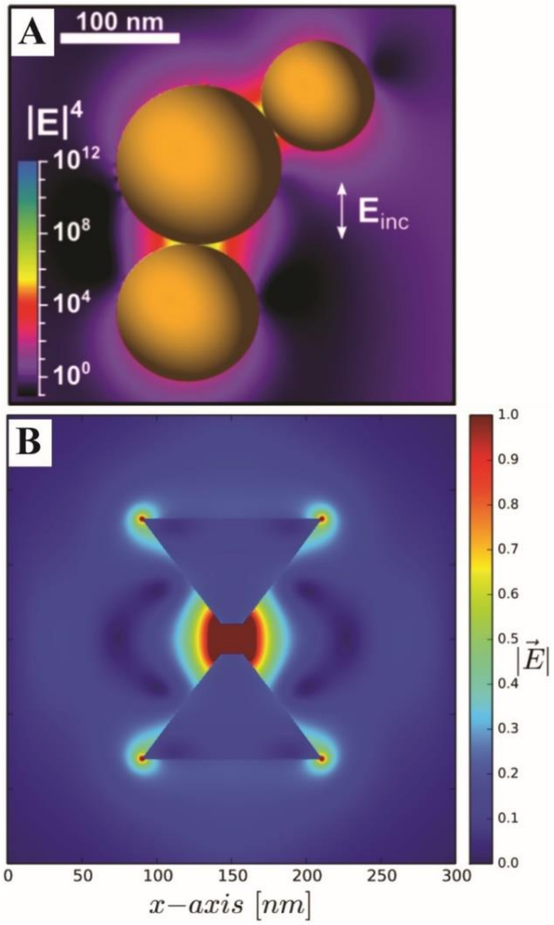

Figure 2.2 Calculated electric field enhancements for gold (A) nanoparticle oligomers[63] and (B) bow-tie antennas.[64] The maximized field enhancement for both systems is produced at the interfaces between the nanoparticles and the regions containing sharp structural features. Part A reprinted with permission from ref. 63. Copyright 2013 American Chemical Society. Part B adapted with the permission from ref. 64, OSA Publishing.

feature or at a sharp, distinct edge on the surface. Examples of a plasmonic field enhancement can be seen in constructs such as the nanoparticle oligomer and bow-tie antenna substrates shown in **Figure 2.2**.[63-64] When positioned within a region of dramatically enhanced electromagnetic fields, a molecule may experience dramatically enhanced scattering due to the subwavelength confinement of electromagnetic light. This phenomenon led to the development of multiple surface-dependent processes and applications, such as surface-enhanced Raman,[65-66] infrared,[67-68] and fluorescence[69-70] spectroscopies, and the invention of light-harvesting plasmonic photovoltaics.[48-54] Once photoexcited, the coherent electromagnetic field decays rapidly and effectively acts like an AC field being driven by the photoexcitation source, making it unlikely to have a direct impact on the photocatalytic reaction pathway.

2.3.1.3 Hot Carrier Generation

After the surface plasmon loses coherence, the non-radiative decay pathway produces a distribution of hot carriers that may be utilized in initiating photocatalytic reactions. This multistep decay process occurs primarily via Landau damping,[71] where energy is transferred from a coherent plasmon to individual electron-hole pair excitations. Initially, the hot carrier distribution is nonthermal and contains charged species far from the Fermi level of the material.[3, 72] Then, hot electrons and holes rapidly thermalize, reaching a Fermi-Dirac distribution that corresponds to a high effective electron temperature. This initial thermalization is carried out through a redistribution of the energy via electron-electron scattering interactions during the next several hundred femtoseconds (1 fs – 100 fs).[73-74] During this time the hot electrons and holes may contain energies ranging from the Fermi level to the work function. These charge carriers are sufficient in quantity and lifetime to initiate external chemical processes (**Figure 2.3**).[3] The hot carriers further dephase through an additional relaxation mechanism consisting of electron-phonon interactions over a timescale of 1 – 10 ps.[75-76] It is during these two time intervals that the charge carriers may contain sufficient energy to transfer to a nearby chemical species to initiate a single or multi-step chemical reaction.

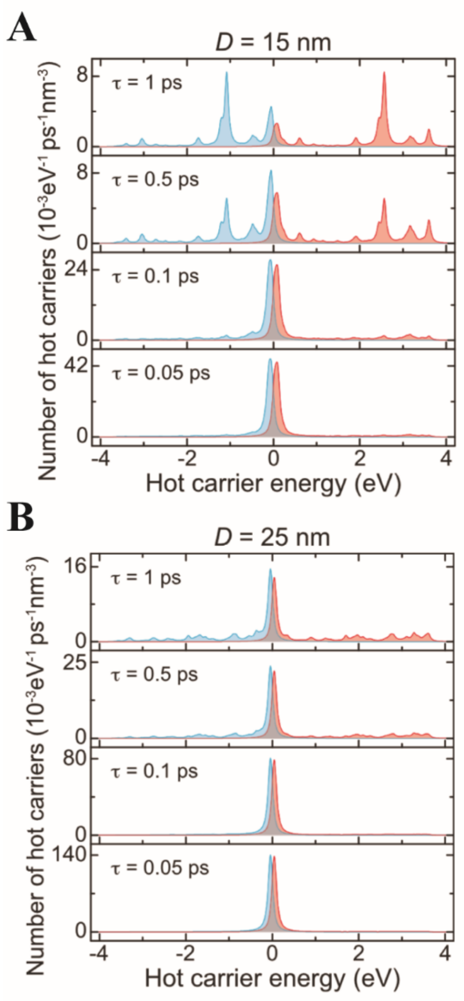

Figure 2.3 Theoretical modeling of the hot carrier distribution as a function of their energy in silver nanoparticles with diameters of (A) 15 and (B) 25 nm. An abundance of hot electrons (red) and holes (blue) are generated via plasmon decay in the 15 nm particle while the hot carrier generation is significantly diminished in the 25 nm particle. Figure reprinted with permission from ref. 3. Copyright 2015 American Chemical Society.

The ultrafast time scales described above can present challenges in using plasmonic substrates to drive photocatalytic processes. A large majority of industrial significant catalytic processes rely on bimolecular reactions that are induced through collisions in the gas phase. However, due to the extremely short lifespans of plasmonic hot carriers, current reaction activities and turnover frequencies are limited by the low probability of interactions between molecules in free space and the hot carriers generated near the surface. Plasmon-mediated catalysis would be more efficient if the reactants can be pre-loaded onto the surface, as is common in most heterogeneous catalytic processes, dramatically increasing the likelihood of inducing the interactions between the hot carriers and targeted reactants. Unfortunately, achieving controlled pre-loading is quite difficult for the most prevalent plasmonic materials (Au and Ag).[1] Coupling these plasmonic materials with more reactive metals may be the most promising route for achieving high efficiency catalysis.[14]

2.3.1.4 Localized Heating

After the electrons have undergone the fast electron-electron and electron-phonon scattering events (10 fs - 10 ps) and have reached a thermalized distribution, the remaining energy is transferred to the localized environment (both solvent and adsorbed molecules) in the form of heat.[37-38] Plasmonic photothermal heating has received a considerable amount of attention in the past due to its potential of utilizing plasmonic nanoparticles as an excellent agent for delivering thermal energy in a highly localized manner.[5-6, 77] In fact, an exciting field utilizing photoinduced plasmonic heating is plasmonic photothermal therapy.[55-61] This form of cancer therapy employs nanoparticles with plasmons specifically tailored to the near-infrared to minimize absorption by any tissue above the nanoparticles. The particles are targeted at cancerous cells and irradiated with an external near-infrared light source to initiate a phase of cell death via localized thermal heating and induce tumor remission. In addition to photothermal therapy, localized plasmonic heating has also been applied in other applications such as drug delivery and release,[78] steam generation,[79] photothermal therapeutics,[80] and growth manipulation of nanoscale structures.[81-82]

Localized plasmonic heating has also been demonstrated as a fundamental mechanism for carrying out or assisting certain catalytic reactions.[5, 36] A surplus of localized heat is typically a vital condition for a variety of endothermic reactions. During the plasmon decay process, the formation of highly-localized thermal environments, both on the nanoparticle's surface and surrounding medium, can be an excellent source of thermal heat transferred to a nearby molecular species. In fact, localized heating is one of the few benefits of the lossy nature of plasmons.[83] While working in tandem with the plasmonic hot carriers, the released thermal energy could play an integral role in reducing energetic barriers preventing a reaction from taking place. A consideration of the interplay between local heating and hot carrier generation is necessary for successfully mediating a photocatalytic process.

2.3.1.4 Modified Molecular Potential Energy Surfaces

Another aspect of plasmonic photocatalysis is the formation of new energy levels as a molecule adsorbs to the surface of a plasmonic material. In this scenario, the strong coupling between the plasmon and molecule may lead to an alteration to the molecular resonances. An analogous effect was discussed by Boerigter *et al.* in 2016.[8, 84] Boerigter's work described new hybridized metal-adsorbate states that form as a result of molecular chemisorption to a metal surface, producing a new charge transfer pathway from the nanoparticle to the molecule. These chemical interactions on the surface resulted in a highly-modified coupled system that allowed for resonant energy transfer between the plasmon and adsorbate. A more detailed discussion of this study is provided in the surface-enhanced Raman spectroscopy section further on in this review. This proposed pathway was successful in providing empirical evidence of the effects of molecule-surface interactions on plasmonic photocatalysis. In 2018, Kazuma *et al.* were successful in identifying a plasmon-induced single molecule dissociation of dimethyl disulfide ($(CH_3S)_2$) on Ag and Cu surfaces with scanning tunneling microscopy (STM).[84] Here, the authors found that the dissociation was mediated by an energy transfer from the localized surface plasmon to the adsorbed molecular species. The direct adsorption of the $(CH_3S)_2$ onto the metal substrates resulted in the LUMOs of $(CH_3S)_2$ to be weakly hybridized with the metal. The weak hybridization significantly reduced the likelihood of excited state relaxation to the ground state, which gave rise to an accessible dissociative potential energy surface. There is a substantial literature within the surface science community that has detailed the interactions between molecular adsorbates and surfaces, which may be quite helpful for further understanding the interplay between surface and plasmonic effects on the electronic states of adsorbed molecules.[85-89] The resulting from these studies ultimately laid a groundwork for understanding surface and molecular plasmonic effects. However, a discussion into these interactions is beyond the scope of this review. Due to this complexity of the coupled molecular-plasmonic system, a variety of technical approaches are needed to examine the transient mechanisms relevant to plasmonic photochemistry.

2.4 Select Methods to Elucidate the Mechanism of Plasmon-Mediated Photocatalysis

2.4.1 Spectroscopy

2.4.1.1 Surface-Enhanced Raman Spectroscopy

One of the more effective and frequently used techniques to explore plasmon-molecule interactions is surface-enhanced Raman spectroscopy (SERS). SERS is a vibrationally-sensitive technique that exploits the fundamental nature of plasmonic systems by enhancing the Raman-scattered signal generated by molecules positioned within the substrate's regions of most dramatic field enhancement, which are known as hot spots in the SERS community.[17, 90] SERS is an excellent method for probing and monitoring plasmon-mediated photoreactions in situ and in real-time due to its remarkably high signal enhancement, which can enable microsecond acquisition times.[91] These experiments are typically highly sensitive to the signal arising from the most enhanced hot spots on the plasmonic substrates.[92] Traditionally, the nanostructures are noble metals (e.g. gold and silver) that have been specifically fabricated or synthesized to host sharp, nanoscale features that couple together to form hot spots.

The magnitude of a collected signal can be quantified by calculating a SERS enhancement factor (EF) for the plasmonic substrate used in the experiment. The SERS EF can be calculated by the following equation [93]:

$$EF = \frac{I_{SERS}/N_{surf}}{I_{NRS}/N_{vol}}$$

where I_{SERS} and I_{NRS} are the Raman intensities on the SERS substrate and under normal conditions, respectively. N_{surf} is the number of molecules probed on the substrate and N_{vol} is the number of molecules probed during the normal Raman collection. This equation is evaluated at a set excitation wavelength for a specific Raman-active vibrational mode. Multiple assumptions, such as the molecular probe's surface coverage and estimated Raman cross-sections, can be made during these calculations and may lead to discrepancies in the values reported throughout literature. Understanding SERS EFs is essential for appropriately evaluating the work performed within this field, as it can be a useful metric of the localized electric fields experienced by the molecular probes.[20] However, it is important to note that the EF in nearly all SERS experiments are ensemble-averaged. This ensemble averaging can include contributions from hot spots with EFs ranging across ~6 orders of magnitude, although the strongest enhancing sites produce a vast majority of the collected Raman signal. Fang *et al.* published an exceptional study that examined the distribution of individual hot spots and how they contribute to the overall SERS intensity.[92] They found that fewer than 0.01% of probed hot spots in a single SERS exposure account for nearly 25% of the collected SERS signal. Therefore, the reported SERS EFs in most publications are typically a lower bound to overall signal magnitude due to the assumption that every adsorbed molecule contributes to the SERS signal. There is currently a huge focus in the literature on developing new SERS substrates,[94-100] but until atomically-defined nanostructures are available in geometries large enough to support a surface plasmon, they will fundamentally be limited by this ensemble-averaging, making absolute quantitative analysis difficult.

In fact, SERS has a myriad of advantages for examining the mechanism behind plasmon-mediated photocatalysis. Being a vibrationally-sensitive spectroscopic technique, a SER spectrum offers much more detail and information about the molecular probe's structure than electronic spectroscopic techniques. SERS is capable of discerning any minor alterations to the molecule's orientation on the surface through discrete changes in the spectra. Also, the rapid decay of the electromagnetic fields near the plasmonic nanostructure's surface ensures that the signals are generated from molecules on or near (r^{-10} distance dependence for spherical nanoparticles) the surface,[17, 101-102] making it a highly selective technique. The selectivity of SERS ensures the probed molecules are the most susceptible to interactions with any plasmon-induced effects.

However, the inherent limitations of SERS must also be addressed. The selectivity of this technique comes with a cost: the molecular probe typically contains specific functional groups that have a strong affinity to the surface. Certain chemical moieties (thiols, amines, N-heterocyclic carbenes) undergo chemisorption on to the surface of traditional plasmonic metals and may be confined within the intense electromagnetic fields produced during excitation. Another constraint is the limited options currently available for surface plasmon-hosting substrates. The most commonly used substrates are gold (Au), silver (Ag), copper (Cu), and more recently, aluminum (Al) due to their enhancement capabilities which cover most of the visible and near-infrared spectrum. Nevertheless, the dramatic signal enhancement found in a wide-range of Au and Ag substrates has resulted in these metals being the leading materials for exploring plasmon-mediated reactions with SERS.

One of the most interesting aspects of using SERS to study surface plasmons and their subsequent dynamic processes is how the technique is capable of simultaneously initiating a photocatalytic reaction while also probing the vibrational features of reacting adsorbates. The most meticulously studied chemical reaction using SERS is the dimerization of both 4-nitrobenzenethiol (4-NBT) and 4-aminothiolphenol (4-ATP) to 4,4'-dimercaptoazobenzene (DMAB),[20, 103-109] which will be a common reaction discussed throughout this review. Most variants of SERS techniques collect signals that effectively describe how the molecules are behaving in the steady-state regime, which can contain data rich with information about reaction yields, efficiencies, and rates. However, this experimental constraint may be viewed as a limitation as it doesn't allow for an analysis pertaining to the transient dynamics that occur during a chemical reaction.[3] To address this concern, multiple research groups are aggressively attempting to develop ultrafast SERS techniques that can monitor the step-by-step mechanism of various plasmonic dynamics.

An elegant study published by Boerighter *et al.* used SERS to examine the mechanism of charge transfer from a plasmonic system to adsorbates.[8] Their findings suggest that by considering the effects of molecular adsorption on the flow of charge within the plasmonic nanostructure, the yield of extracted hot electrons potentially could be substantially higher than the theoretical yields derived from traditional metal-centric models. The conventional models describe the process of charge excitation in plasmonic nanoparticles and the subsequent transfer to an adsorbed species, which disregards any potential influence the adsorbate may have on the transient dynamics. Here, the authors propose an alternative mechanism for charge transfer that introduces a new pathway capable of a direct and on-resonant charge transfer into the high-energy adsorbate states (**Figure 2.4A-B**). This alternative mechanism circumvents the ‘losses’ that occur during the electron-electron and electron-phonon thermalization pathways that are present in the present-day mechanism.[83] The experimental work to support this proposal examined the anti-Stokes and Stokes scattered photons to simultaneously measure the vibrational temperatures within the chemical adsorbates and metal nanoparticle (**Figure 2.4C-D**). During these studies, they found that methylene blue experienced an elevated vibrational temperature when excited by 785 nm photons and not 532 nm photons. These results hint at the possibility of an observed charge transfer between the metal and adsorbate during 785 nm excitation, which is resonant with the proposed hybrid metal-adsorbate states that are formed upon chemisorption.

The conclusions proposed in this work suggest that the community may need to direct more attention towards the effects of molecular adsorption and hybridized states on plasmonic charge transfer leading to photocatalysis. The hybridized metal-adsorbate states formed during chemisorption may give rise to the possibility of a direct, ultrafast pathway from the metal to the adsorbate at the interface between the two materials.

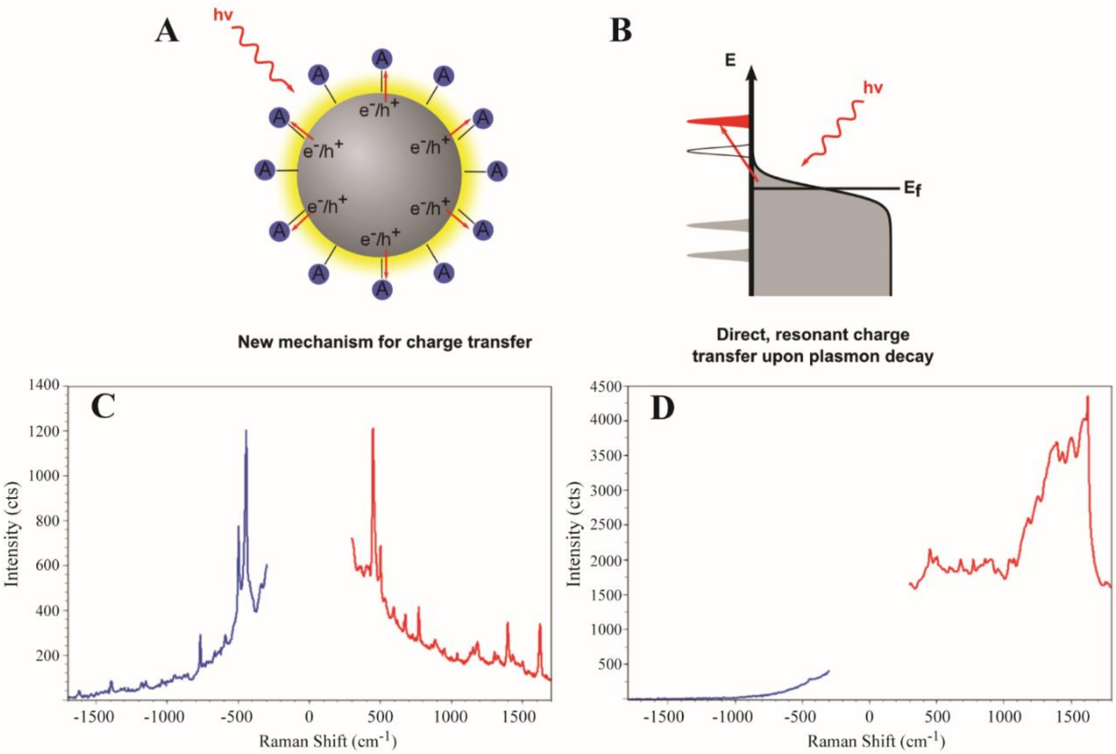

Figure 2.4 The formation of an alternative pathway of resonant energy transfer for plasmonic charge carriers into the high energy states of the molecular adsorbates. (A) This pathway is generated when an adsorbate or semiconductor interacts with the metal's surface and can circumvent the thermalization of hot electrons before transfer occurs. (B) Density of states visualization of proposed mechanism of direct, resonate transfer. (C,D) Data representing the anti-Stokes (blue) and Stokes (red) spectra collected with (C) 785 nm and (D) 532 lasers. There is a noticeable increase in the 785 nm anti-Stokes signal due to a resonant charge transfer into the adsorbates. Figure reprinted with permission from ref. 8. Copyright 2016 American Chemical Society.

Initiating and monitoring chemical reactions across a wide-range of localized field enhancements may provide helpful insights towards optimizing plasmon-mediated photochemistry. Recently, Brooks *et al.* published a study that looked into the effect of field enhancement on the plasmon-mediated dimerization reaction of 4-NBT to DMAB.[20] The ensemble-averaged field enhancement was effectively tuned at multiple different spatial locations across a heterogenous gold film-over-nanosphere substrate. Changes in the localized surface plasmon resonance (LSPR) for each probed region were present due to the random variation of nanosphere packing defects, producing a range of EFs from 5×10^6 to 3×10^7. Interestingly, no identifiable correlations were found between the reaction rate or yield with an increased plasmonic field enhancement, suggesting that plasmon-driven processes are not rate-limiting for this reaction (**Figure 2.5**). The photoreaction rate is likely limited by the local concentration of protons used in the initial reduction of 4-NBT. Additionally, this work found that the presence of alternative plasmon-induced processes, such as a molecular degradation and/or atomic-level substrate alteration, may dramatically impede the reaction's rate or potentially hinder the overall molecular conversion.

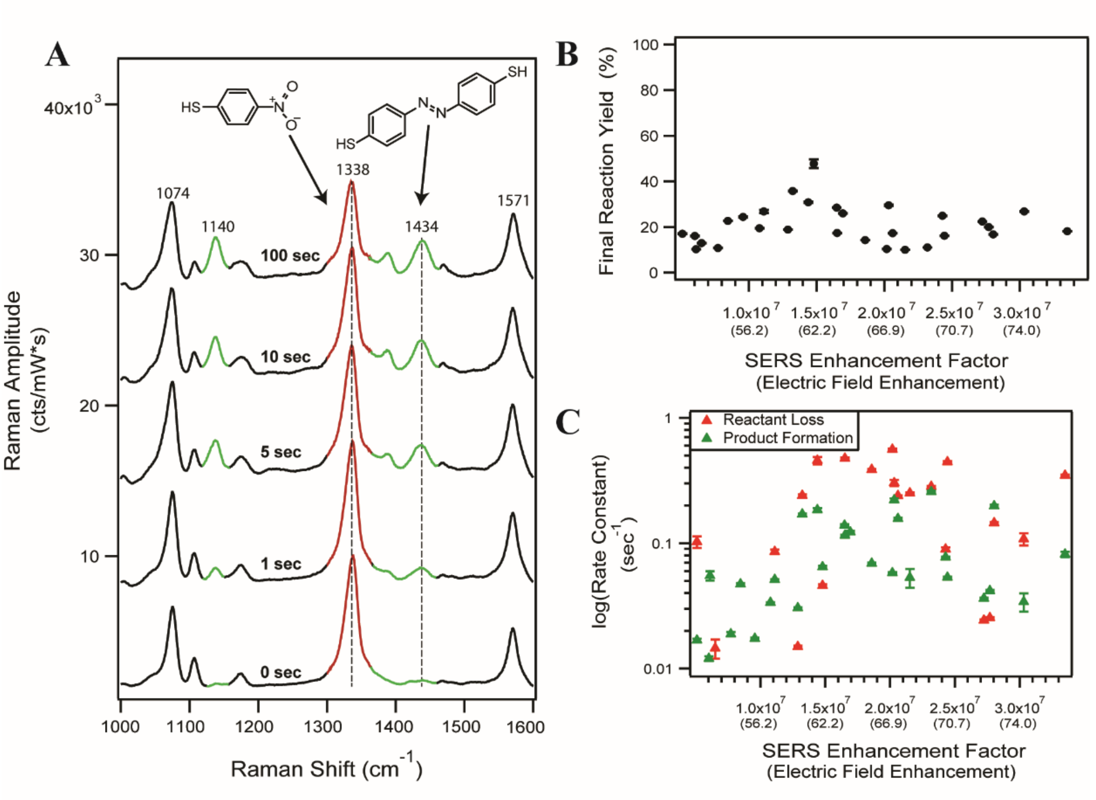

Figure 2.5 (A) Plasmon-mediated dimerization of 4-nitrobenznethiol to 4,4'-dimercaptoazobenzene tracked with SERS. (B) Plot of the final reaction yield's dependence on the ensemble SERS field enhancement. The final reaction yield is a ratio of the final amplitudes of the product and reactant peaks. (C) Comparison of the rate constants for the reactant loss (red) and product formation (green) against the ensemble SERS field enhancement. Figure reprinted with permission from ref. 20. Copyright 2016 American Chemical Society.

These findings argue that plasmon-mediated chemical processes are not always most effectively powered in the strongest regions of field enhancement. Having a firm grasp on the energy partitioning after plasmon excitation for a specific plasmonic system is a necessity for optimizing the targeted output. Redirecting the flow of energy away from the undesired pathways (e.g. local environmental heating, molecular cleavage/dissociation, alternative chemical reactions, etc.) and towards the preferred chemical reaction or catalytic process is the ideal, yet nontrivial, solution for producing plasmonic systems suitable for integration into energetically-demanding industrial processes. SERS can also quantify the spectral relationship between the far-field LSPR and near-field Raman scattering events that occur during the typical SERS experiment. Work performed by Kleinman *et al*. provided a unique viewpoint on how to consider the interplay between far-field and near-field scattering in hot spot dominated SERS collections.[63] They found that the presence of hot spots in single particle SERS studies can clearly modify the optimal excitation wavelength for maximized SERS enhancement. To study these far-field and near-field interactions, they developed a correlated LSPR-transmission electron microscopy surface-enhanced Raman excitation spectroscopy technique. Their results clearly identify that the spectral dependence in individual nanoantennas, which are aggregated nanoparticles encapsulated within a silica coating, and their SERS intensity is dramatically dominated by near-field Raman scattering produced within the hot spots between the two or three aggregated Au nanospheres. In fact, they found that the maximum enhancement was completely independent of the far-field LSPR spectra of both individual Au nanoantennas and an ensemble-averaged collection in their experiments. The maximum ensemble-averaged EF of 5.0×10^7 peaked at an excitation wavelength of 830 nm, even though the far-field LSPR scattering intensity was most intense at ~600 nm.

This report is an excellent example of carefully evaluating hot spot dominated systems and identifying how they can be optimally utilized for future experiments. As the authors appropriately describe, the commonly accepted assumption that the far-field spectral scattering determines the ideal excitation wavelength for SERS enhancement may not always hold true. This work clearly demonstrates the importance of utilizing complimentary computational modeling methods and experimental techniques[3-4] to develop a full description of the plasmonic modes, both bright and dark, for any given system.

2.4.1.2 Single-Molecule SERS (SMSERS)

The preceding section evaluated several SERS experiments that were all performed with a monolayer or near-monolayer of molecules residing on the plasmonic substrate's surface. Results collected with this level of molecular concentration have clearly been used to construct fully-developed and highly-impactful conclusions pertaining to a wide-range of photochemical and catalytic reactions. However, as the name implies, an ensemble-averaged measurement can only describe the physical nature of the adsorbed molecules as a whole, which can hinder identification of clear structure-function relationships. For instance, ensemble-averaged studies are limited to gathering information that is generated from a remarkably wide-range of localized field enhancements, rather than exploring the sensitive behavior of individual molecules as they interact with their highly-specific and unique local environment. Single-molecule SERS (SMSERS) was first reported in two pioneering articles in 1997[96, 110] and the field has vastly grown since its discovery.[111-116]

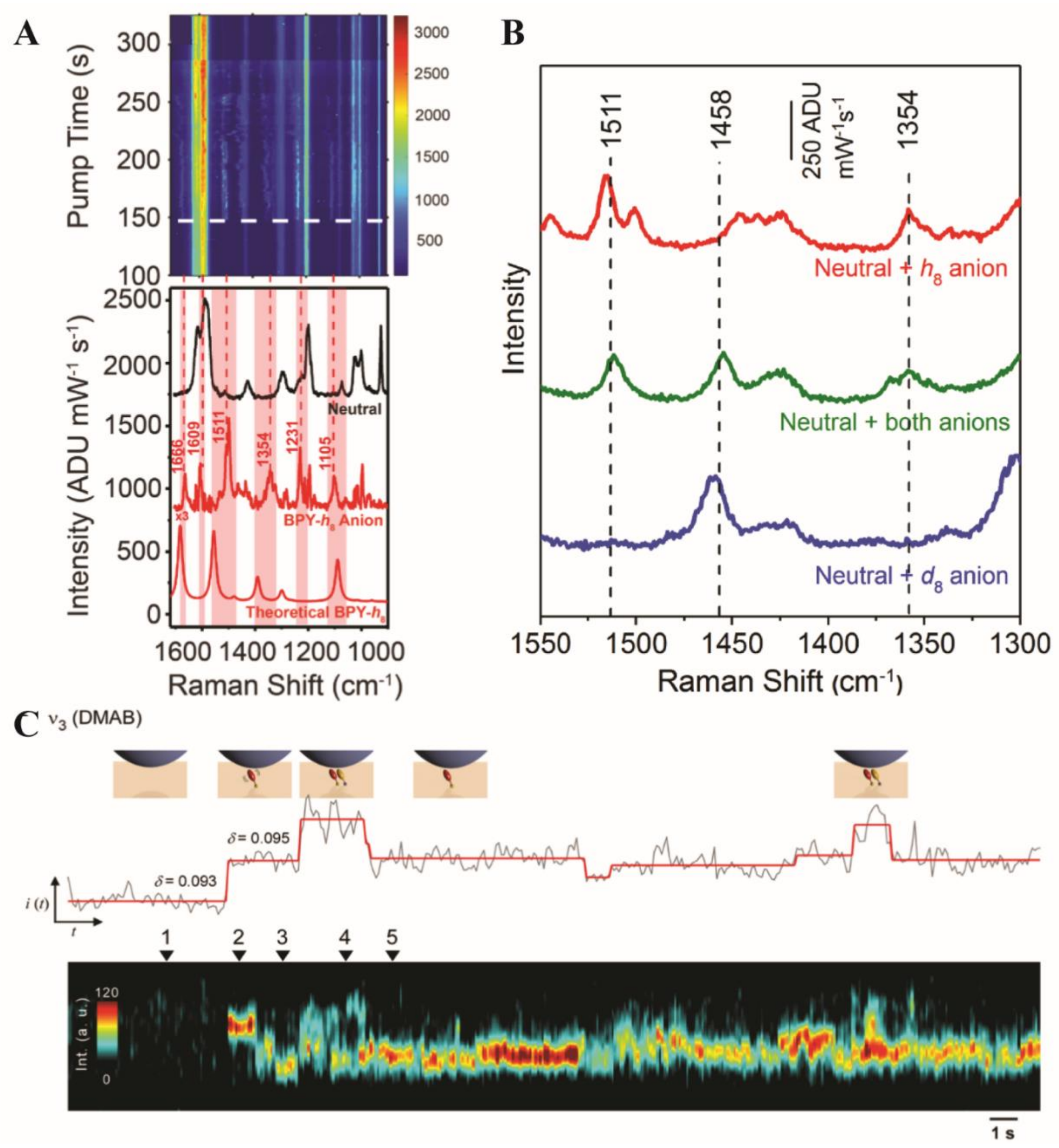

Figure 2.6 Time-dependent single-molecule SER spectra demonstrating the (A-B) anion formation event for BPY on a gold nanoantenna substrate with the associated isotopologue analysis to confirm single molecule limit and (C) single-molecule step transitions following the formation of DMAB in real-time. Part A-B and C reprinted with permission from ref. 117 and 118, respectively. Copyright 2017 and 2016 respectively, American Chemical Society.

Several studies have been key in the development of SMSERS over the last 20 years. A bi-analyte method was developed by the Etchegoin lab in 2006 by statistically comparing the unique spectral information collected from two distinct molecules.[113] A year later, the Van Duyne group developed a similar method that used two isotopologues of a single chemical species.[114] When working in ultra-low concentrations of both molecular species, on average only one variant of the isotopologues is adsorbed to the metal within the effective probing area. Each isotopologue produces a vibrational spectrum containing Raman bands that make it easily distinguishable from the other. Since then, similar techniques have been used to study single molecule dynamics on plasmonic substrates. Recently, SMSERS has been utilized in the detection of plasmon-driven electron transfer. In 2017, Sprague-Klein *et al.* presented a study where 4,4'-bipyridine (BPY-h_8) and its deuterated isotope (BPY-d_8) were adsorbed between gold nanosphere oligomers and subjected to a single particle pump-probe experimental probing technique.[117] The single particles were exposed to a 532 nm pump CW laser to excite the monomer plasmon while simultaneously being probed by a 785 nm CW laser for the signal collection. They observed a delayed (>2 min) plasmon-mediated charge transfer of surface electrons from the gold oligomers to produce long-lived BPY radical anion products (**Figure 2.6A-B**). The authors suggested an accumulation of surface electrons was required before a neutral BPY molecule could successfully accept a nearby hot electron. In fact, a low 3% yield of electron transfer to an adjacent BPY molecule was reported. A similar study was published in 2017 and was also successful in identifying hot electron-driven redox chemistry at a single molecule level using methyl viologen.[19]

Typical SMSERS signals are inherently intricate and difficult to analyze due to dramatic temporal and spectral fluctuations. These fluctuations are caused by several sources, including variations of molecular orientation in an isolated hot spot, atomic-scale surface modifications throughout prolonged photoexposure, and possible Brownian diffusion of the molecule.[114, 119-120] Recently, an innovative SERS-based method to suppress these issues was published by Choi *et al.*[118] Here, they explored a single-molecule catalytic reaction of 4-NBT to DMAB in real-time by monitoring discrete step-like transitions of the reaction's products. These experiments implemented a self-assembled silver nanoparticle-4-NBT-gold thin film substrate to induce and monitor the dimerization of 4-NBT to DMAB in the junctions between the nanoparticles and gold film, which were capable of reaching a SERS EFs of 1.7 x 10^8. Rather than attempting to isolate distinct SERS signals from their collected spectra, the authors developed an innovative method to identify discrete transitions tracking the formation and annihilation of individual DMAB molecules within a single, intense hot spot. **Figure 2.6C** depicts a time-resolved SERS trajectory of the DMAB species as they react within the nanoparticle-thin film junctions. In conjunction with computational modeling, the transitions present in time-dependent data are clear spectral evidence of a single-molecule plasmon-mediated photocatalytic reaction.

Developing new methods to monitor individual molecules as they undergo a chemical transformation is non-trivial. Choi *et al.*'s unique approach of data analysis was capable of extracting data rich with information describing the behavior of individual molecules in a highly complex environment.[118] They addressed the common difficulties found in single-molecule SERS experiments (spectral and temporal fluctuations) and designed a plasmonic system which systematically removed a majority of the randomness by ensuring the adsorbed molecules were situated in the center of well-characterized hot spots. If anything, these studies identify the need for a new class of intricately-designed plasmonic substrates that employ well-defined, easily accessible, and dramatically enhancing hot spots. Recent studies have done an excellent job of utilizing cucurbit[*n*]uril structures to generate well-defined hot spots for ensemble [121] and single molecule [122] SERS detection. Constructing a system that directs the flow of hot electrons to these regions of enhancement should provide a significant improvement to the present-day yields and efficiencies reported. This level of nanoscale design will allow the community to probe the globally relevant photochemical and catalytic reactions, which are currently limited by their low Raman cross-sections in the single-molecule regime.

The advancement of SERS and its ability to probe single molecules has left a clear impact on the field of plasmonics, and more specifically, plasmon-mediated photochemical processes. Having a technique that is inherently linked to surface plasmon generation has ignited a boom in publications heavily invested in better understanding the complex molecule-plasmon interactions. For example, SERS studies were crucial in the identification of the role metal-adsorbate hybridized states may play in modifying the preferred pathway of charge transfer from a plasmonic surface to the molecular probe. Implementing an equal level of well-defined experimental design may help in identifying new phenomena and SERS can continue to be utilized as an excellent technique for further elucidating the complex mechanism of plasmon-mediated photocatalysis.

2.4.1.3 Tip-Enhanced Raman Spectroscopy (TERS)

Another valuable vibrationally-sensitive method used to explore plasmon-mediated photocatalysis is tip-enhanced Raman spectroscopy (TERS). TERS is a spectroscopic technique capable of imaging physi- or chemisorbed molecules with nanoscale or even sub-molecular spatial resolution, while simultaneously providing the ability to manipulate the highly-localized environment surrounding the molecules. The concept of coupling scanning probe microscopy with surface-enhanced Raman spectroscopy (SERS) was first introduced in the 1980s.[123] This technique was successfully demonstrated in decades to follow by multiple independent research groups, each reporting Raman signatures belonging to surface-bound molecules positioned within plasmonic tip-enhanced localized fields.[123-126]

The power of TERS lies in its inherent ability to provide spatially-resolved and spectroscopic information pertaining to one[127-128] or many molecules positioned on a surface. TERS combines the advantages found in SERS and scanning probe microscopy to produce dramatic electromagnetic field enchantments capable of amplifying the chemically-sensitive Raman scattered photons while reaching sub-diffraction spatial resolution. This is achieved by replacing the nanoparticle substrates used in traditional SERS experiments with a sharp tip made of or coated with a plasmonic metal. These tips typically have an extremely sharp radius of curvature (below 50 nm) and can generate highly localized electromagnetic field enhancements in the effective volume between the tip apex and substrate used to host the molecular probes.[129] The sharp, needle-like tip apex serves as a physical point-source for the surface plasmon generation and can generate a localized field that rapidly decays as it extends away from the tip.[130] When the tip is brought within close proximity to a flat metal substrate, the highly-confined electromagnetic field is further amplified due to coupling between the tip and surface. This phenomenon, which is known as the gap-mode effect, is achievable when the tip is positioned approximately 1-2 nm away from the metal surface. The enhancement produced in this confined gap-mode effect experiences a d^{-10} distance dependence, where d is the distance between the tip apex and the flat metal surface.[131-132]

One of the more helpful aspects of TERS is its ability to selectively probe individual or multiple molecules at well-defined regions on a planar substrate, composed of both metallic and non-metallic materials.[133] In fact, if the proper molecular analytes are selected, TERS is capable of initiating and tracking plasmon-mediated catalytic reactions in real-time in a similar manner as SERS.[134-137] However, if the goal of the experiment is to study the effects of the tip alone, the technique can be modified to replace the metallic substrate with a material that doesn’t have the proper dielectric constants to host a surface plasmon. This removes the inherent requirement to have the molecules locally adhered to the plasmonic substrate and gives more flexibility in the experimental approaches the user may explore.

One key difference between SERS and TERS is that SERS signal is typically produced from the regions of highest field enhancement and is generally ensemble-averaged and much higher throughput. In TERS, the dramatically high spatial resolution provides a more detailed analysis of the studied environment. In a similar manner, the hot electrons (or holes) can transfer to the excited state of the adsorbed molecules and drive a chemical reaction. In this configuration, the tip may be selectively positioned over specific molecules or clusters for controlled transport of hot carriers to the desired molecules. When using scanning tunneling microscopy (STM)-TERS, the tip can also be utilized as an additional source of electrons with a tunable energy range, allowing for a more detailed analysis of the studied material or chemical reaction.

Unfortunately, a handful of complications may be present when attempting to mediate and characterize plasmon-driven chemical reactions with TERS. One of the more difficult challenges in performing TERS experiments is reproducibly fabricating the nanoscale plasmonic tips.[138] Presently, the most common method for tip fabrication is electrochemically etching silver and gold wires.[139] A solution based etching method such as this will produce tips that are highly-heterogenous in shape, especially near the tip apex. This lack of reproducibility introduces a wide-range of local environments for enhancing the collected Raman signal or mediating a chemical reaction, making it extremely difficult to produce consistent results across multiple tips. The tip stability can even be quite poor during the course of a typical TERS measurement, resulting in data that is potentially flawed or inconsistent in nature. Another challenge when approaching plasmon-mediated photocatalysis with TERS is quantifying any contributions that may arise from electrons tunneling from the metal tip to the adsorbed molecule. To work around this issue, users have also coated the plasmonic TERS tips with an ultrathin oxide film. The oxide layer protects and isolates the plasmonic tip away from the probed surface and minimizes undesirable interactions.[137]

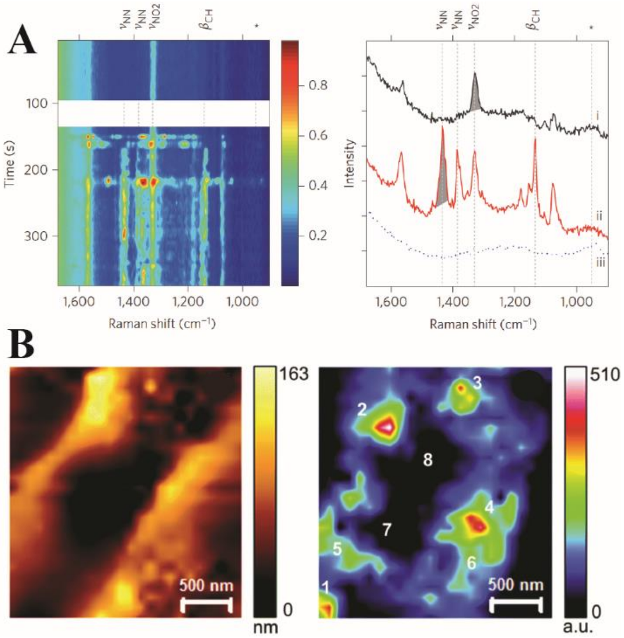

Figure 2.7 Plasmon-mediated photocatalytic reactions monitored with TERS. (A, left) Time-dependent TERS measurements before and after irradiation with 532 nm laser light. Raman signatures begin to appear in the TERS spectra after the tip is illuminated with a 532 nm excitation source. (A, right) Raman spectra corresponding to 4-NBT (black) and DMAB (red). (B, left) Topography image of the silver substrate and (right) TERS chemical reactivity map of DMAB after inducing dimerization of pMA. Part A reprinted by permission from Springer Nature: Nature Nanotechnology ref. 135, Copyright 2012. Part B reproduced from ref. 137 with permission of The Royal Society of Chemistry.

Plasmon-mediated photocatalytic reactions were first tracked with TERS in 2012. van Schrojenstein Lantman *et al.* published a report that monitored the well-studied dimerization reaction of 4-NBT to DMAB.[135] Here, the authors implemented a dual-wavelength approach to monitor the photocatalytic process. They employed a 633 nm excitation source to monitor the vibrational spectra corresponding to both 4-NBT and DMAB while short, discrete periods of 532 nm laser light were directed towards a silver-coated tip to initiate the dimerization. Using the 532 nm laser source alone to probe the surface-bound molecules resulted in an instantaneous conversion to DMAB and no relevant information could be extracted. However, by exciting the plasmon with short bursts of low power 532 nm laser light, they could significantly slow down the rate of the ensemble-averaged reaction and monitor the molecular conversion during a slower timescale. By starting with a stable spectrum of 4-NBT, the authors were able to produce time-dependent TERS measurements that tracked the growth and subsequent decay of the DMAB and 4-NBT, respectively (**Figure 2.7A**). Ultimately, this study demonstrated the feasibility of using TERS to study the molecular dynamics that are occurring at the nanoscale level, clearly highlighting the potential to employ TERS to extract information that may help describing the interactions between plasmons and molecules.

Kumar *et al.* also reported an impressive study that experimentally mapped out the catalytic activity in the photoinduced reaction with nanoscale spatial resolution using AFM-TERS.[137] The authors studied a similar dimerization reaction, where they reacted two *p*-mercaptoaniline (pMA) moieties together to form DMAB. To prevent the molecules from physically interacting with the tip, they protected a silver-coated tip with an ultrathin layer of alumina film. The alumina film prevented any interactions between the silver tip and thiol-containing molecules, which include chemisorption and unintentional spontaneous catalysis, and allowed for the acquisition of chemical reactivity maps with nanoscale resolution on nanostructured silver substrates. With the alumina-coated silver tip, they were able to probe a nanostructured silver substrate and identify the regions of greatest photocatalytic activity by monitoring the production of DMAB (**Figure 2.7B**). The experimental design allowed for probing conditions capable of achieving a spatial resolution of 20 nm, allowing the authors to map the chemical reactivity on individual plasmonic nanoparticles. This was the first reported publication that successfully mapped the substrate-dependent catalytic activity of a reaction in a TERS configuration. In addition, the TERS configuration allowed the users to identify the catalytically active and inactive regions on a plasmonic substrate with a 20 nm spatial resolution, which was unprecedented in the field of plasmonics.

Both of these studies are excellent examples of using TERS to induce a chemical process and monitor as the molecules undergo a physical transformation. The plasmonics community stands to gain valuable insights once TERS is able to study industrially relevant catalytic processes. However, it is clear that using TERS to reproducibly study alternative chemical reactions or heterogeneous catalytic processes will be challenging, and improvements in tip fabrication methods would be extremely useful for quantitative measurements.

2.4.1.4 Ultrafast SERS

Ultrafast SERS is a burgeoning field that combines plasmonic enhancements discussed in the previous sections with ultrafast time-resolved Raman spectroscopies to investigate the dynamics of plasmon-molecule coupled systems on picosecond (ps) and femtosecond (fs) timescales (**Figure 2.8A**). Here, in the first portion of this section, we use the term ultrafast SERS to refer to all pump-probe plasmon-enhanced Raman scattering spectroscopies with time resolution in the ps to fs range.

In recent years, these techniques have been applied toward understanding plasmon-molecule interactions[21, 140-142] and single-molecule dynamics.[143-144] The field of ultrafast SERS has been discussed at length in recent reviews.[145-146] Here, to fit the scope of this review, we will be highlighting and discussing the recent applications, developments, and challenges in ultrafast SERS as applied to plasmonic photocatalysis.

With a time resolution on the order of molecular vibrational periods, and thus the timescale of the nuclear motions involved in chemical reactions, ultrafast SERS has the capability to monitor key photophysical processes and reaction dynamics of such phenomena in real time, elucidating underlying mechanisms and providing a pathway toward their optimization. Of interest are the complex interactions between adsorbed molecules and plasmon generated phenomena: hot electrons and localized hot spots, which can be observed via transient changes in intensity and line shape in ultrafast SER spectra.[21, 140, 143, 147] In conjunction with complimentary spectroscopic techniques and theoretical modeling, ultrafast SERS has great potential as a tool for observing these interactions across a complete reaction coordinate, monitoring how energy partitions with variations in environment and plasmonic substrate morphology. Ultimately, the transient data extracted from ultrafast SERS studies may help to elucidate fundamental principles in plasmon coupled systems, leading to improved photocatalytic technologies and plasmonic substrates, as well as providing empirical data toward the development of a unified electromagnetic and chemical SERS theory.[148]

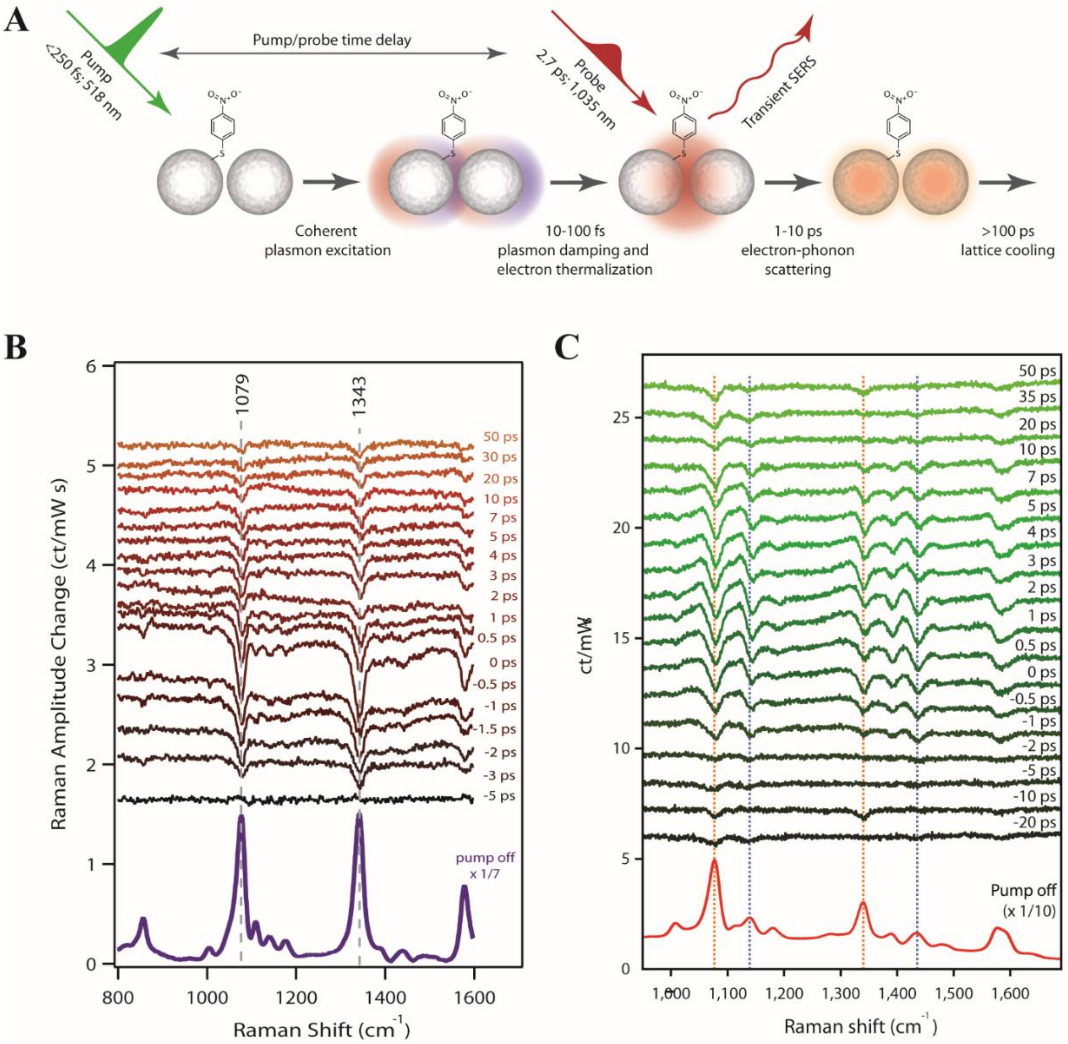

Figure 2.8 (A) Representation of the transient dynamics that ultrafast SERS is capable of measuring and tracking on aggregated AgNPs. (B) Ultrafast SER spectra describing the behavior of 4-NBT molecules as the AuNP's plasmon experiences a photo-induced energy shift. (C) Fano-like signatures indicate that the energy transfer between the plasmon and the adsorbates is an indirect mechanism. Parts A and C reprinted with permission from ref. 21 and part B modified with permission from ref. 140. Copyright 2016 and 2017 respectively, American Chemical Society.

A recent study by Keller *et al.* has shown promise towards the time-resolved quantification of hot electron generation at plasmonic surfaces.[140] In this study, Keller obtained ultrafast SER spectra of 4-NBT reporter molecules on 70 ± 10 nm gold nanoparticles. Peak depletions from 4-NBT ring breathing (1079 cm^{-1}) and NO_2 symmetric stretch (1343 cm^{-1}) vibrational modes were observed, maximized as the pump and probe pulses overlap and decayed over a period of 50 ps (**Figure 2.8B**). In accordance with transient absorption, electrochemical, and theoretical models, it was determined that the transient peak depletions were caused by a red shift in the structure's LSPR, resulting from delocalization of the hot electrons. The calculations suggested that the charge density shift resulted in the displacement of approximately 10^9 free electrons in the metal. While they did not directly observe the product of the hot electron-induced LSPR shift, they proposed that the charge delocalization may be due to a charge transfer between the hot electrons and adsorbed molecules, uneven distribution of the hot electrons across the probed regions, or potential electron-phonon interactions that result in the heating of the metal lattice. This study corresponds well with a similar study by Brandt *et al.*, which utilized the same ultrafast SERS methodology to probe the plasmon-driven photochemical dimerization of 4-NBT to DMAB on silver nanoparticles.[21] This study proposed a hot electron charge transfer mechanism for the dimerization, evidenced by transient Fano line shapes and transient changes in 4-NBT/DMAB signal amplitudes. Here, as seen in **Figure 2.8C**, the Fano features are attributed to the coupling of the broad AgNP emission and the narrower SERS photons. The relevant amplitudes of product and reactant in the transient spectra as compared to the ground state spectra proved that the nanoscale regions generating the broadband emission were most efficient at driving the photoreaction. Thus this work indirectly proved the role of localized hot electrons in driving the plasmon-induced process.

Together, these studies utilize the time resolution of ultrafast SERS to provide a description of charge delocalization and charge transfer from a plasmonic substrate to an adsorbed molecule. Interestingly, the Fano line shapes observed by Brandt, *et al*. were not apparent in the study by Keller *et al.*, suggesting a different mechanism of broadband light emission in gold and silver nanoparticles**.** These results not only display the capability of ultrafast SERS to observe and interpret changes to the coupled plasmon-molecule system in real time, but also highlights the dependence of ultrafast SERS measurements on the substrate composition. This is critical to the development of application specific ultrafast SERS substrates, where differentiation in the identity and morphology of the plasmonic substrate may allow tuning of interactions between scattered photons and other light-induced processes. Unfortunately, due to the fact that collected SERS signal is spontaneous, the aforementioned ultrafast SERS techniques are limited to probing transient dynamics that occur on the picosecond timescale, as with spontaneous Raman, the spectral resolution and temporal resolution are inversely related. This resolution is sufficient to resolve many of the nuclear structural changes, but unable to track the early plasmonic dynamics that occur after photoexcitation.

Other recent work has been devoted to the optimization of ultrafast SERS techniques that implement stimulated Raman spectroscopies to achieve femtosecond time resolution for probing the effects of photoexcited plasmons on proximal adsorbates. This is enabled through the use of surface-enhanced coherent anti-Stokes Raman scattering (SE-CARS) and surface-enhanced femtosecond stimulated Raman scattering (SE-FSRS) experiments.[141, 143] Both techniques are similar in experimental design, but involve different Raman scattering pathways to provide vibrational information describing the molecular analyte, optimally with time resolution in the 10 – 100 fs regime. Both spectroscopic techniques employ 2-3 laser pulses that interact at the sample of interest to produce the stimulated Raman signal. A CARS experiment is designed to generate a stimulated beam of blue-shifted signal (**Figure 2.9A**), while the four-wave mixing that is dominant in FSRS stimulates Stokes-shifted photons (**Figure 2.9B**). While both techniques are excellent in producing stimulated signals useful for both molecular imaging as well as time-resolved measurements, they are both generally limited to a high concentration of molecules or materials with large Raman cross-sections. To bypass this issue, multiple attempts have been made to locally enhance the Raman signal by the means of plasmonic surface enhancement.

Crampton *et al.* demonstrated the novelty of SE-CARS to study plasmonic materials and their enhancement capabilities.[143] In this study, the authors probed core-shell Au-silica dumbbells (Au@SiO_2-NTs) with *trans*-1,2-bis(4-pyridyl)ethylene (BPE) adsorbed at the nanojunction of the participating gold nanospheres (**Figure 2.9C**). The results highlight several conclusions regarding the development of surface enhanced non-linear spectroscopies. The enhanced local electric field results in a limited accessible power range between observation of signal and damage to the sample. Also, the stimulation of the Raman field in the SE-CARS process is easily saturated using relatively low pulse energies (100 fJ in a 100 fs pulse). The authors also found that when working in a few-molecule regime with SE-CARS, the time-domain and frequency-domain measurements are not direct Fourier transforms, with the time-domain measurements revealing more in-depth information on the molecular dynamics.

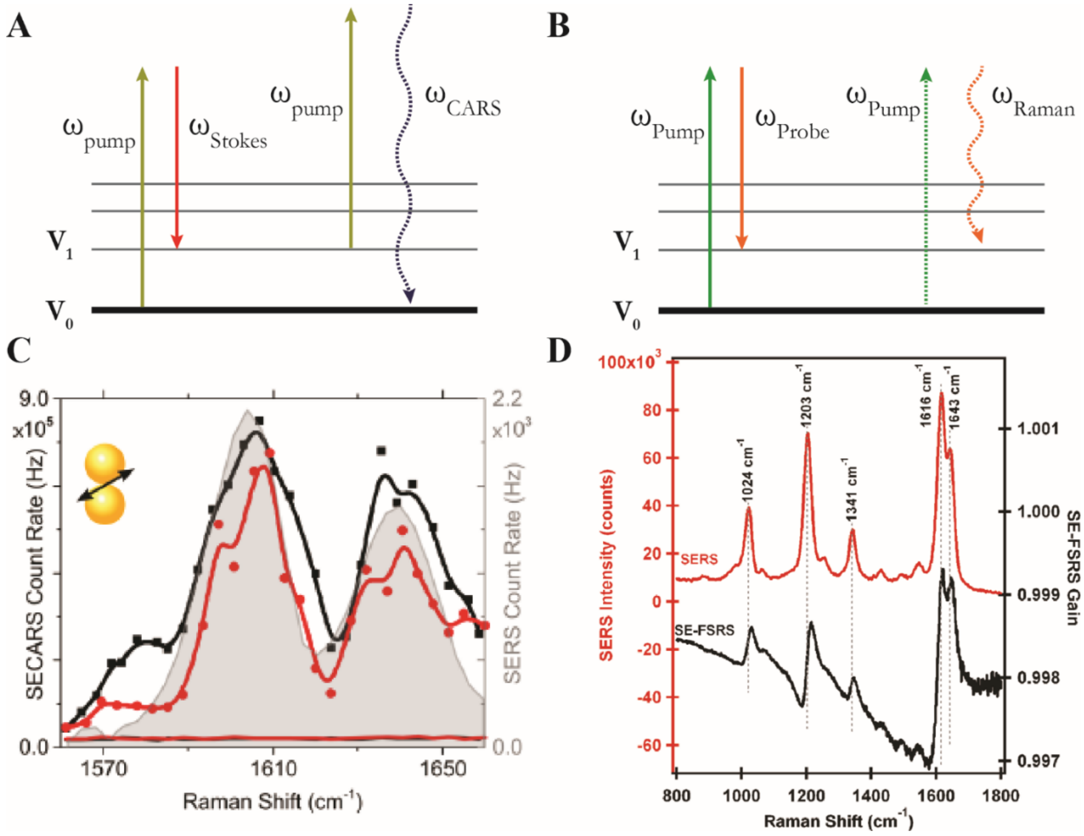

Figure 2.9 Energy diagram depicting the photon interactions leading to the generation of surface-enhanced (A) CARS and (B) FSRS signal. (B) Comparison of ps-SECARS spectra (red and black traces) and the cw-SERS spectra (grey, shaded peaks). (D) Raman spectra of BPE using cw-SERS (red) and SE-FSRS (black). Parts C and D reprinted with permission from ref. 143 and 149, respectively. Copyright 2016 and 2017 respectively, American Chemical Society.

An alternative stimulated Raman technique is SE-FSRS, which was first introduced in 2011 by Frontiera *et al.*[149] The SE-FSRS signals have Fano line shapes, which result from coupling between the broadband plasmonic response from colloidal nanoparticles and the narrowband vibrational coherences in the molecular adsorbates (**Figure 2.9D**).[147, 150-

[151] Interestingly, the vibrational coherence's dephasing time was independent of the coupling between the plasmon and molecule.[147] This initial study laid the groundwork for the future attempts towards applying and further understanding the mechanism behind SE-FSRS. Follow-up work by Gruenke *et al*. described the optimal concentration of particles and identified the path length dependence in SE-FSRS measurements.[141, 146] They emphasized that extinction and enhancement in SE-FSRS, and other SE resonance Raman techniques, must be appropriately balanced to achieve optimal signal intensity and signal to noise ratios, particularly in the transmission geometry used here. These studies serve to elucidate fundamental factors in designing efficient ultrafast SERS experiments. Understanding the factors that play a role in signal intensity, sensitivity, degradation, and interpretation are key to the development of a technique that can be readily adopted and applied by the scientific community at large. However, currently both the SE-CARS and SE-FSRS studies have been primarily limited to Au@SiO_2 nanoantennas, which has limited applications. The continuation of such diagnostic work is key toward the characterization and development of reliable ultrafast SERS experimentation.

Despite recent advances, some hurdles must still be overcome in the development of femtosecond SERS techniques. Present studies have been limited to a narrow range of model systems, which still require optimization for expansion into studying more complex plasmon-molecule interactions. Furthermore, numerous processes that occur within plasmonic-molecular systems, particularly in the interrogation in the few molecule limit, can greatly complicate data interpretation.[152-153] While the above techniques have come a long way to understanding these interactions, there is still much fundamental work that needs to be done to make them more efficient and effective as analytical tools for understanding plasmon-molecule dynamics. To date, there is no study that has been successful in obtaining structural snapshots of evolving chemical reactants on plasmonic surfaces. Although, once the technical hurdles are surmounted, these techniques should be tremendously useful approaches for identifying the vibrational character of a molecular species as it undergoes a plasmon-mediated chemical reaction. Having the tools to spectroscopically track the intermediate states as a molecular transformation takes place would dramatically increase our understanding of these non-trivial mechanisms involved in plasmonic photocatalysis. However complicated in experimental design, the advancement of ultrafast SERS has far reaching implications in fully realizing applications of plasmon-related processes and deserves continued attention in coming years.

2.4.1.5 Transient Absorption (TA)

The previous sections have contained numerous experimental examples where all the significant data was collected by probing a set of molecules or an individual species as they interact with a photoexcited surface plasmon. However, to effectively probe and understand the interactions between surface plasmons and the electronic states of a given material, a different flavor of ultrafast spectroscopy is required. Here, we discuss the efficacy of TA spectroscopy as a tool to elucidate key parameters of plasmon-induced processes. The configuration of TA spectroscopy used to study plasmonic materials employs two femtosecond laser pulses: a pump pulse for photoexcitation, and a probe pulse to track the subsequent plasmon-induced dynamics. For a more detailed description, Berera *et al.* and Ruckebusch *et al.* have provided excellent reviews on the subject.[154-155] By evaluating the entire collection of transient spectra, one can deduce the effect of plasmonic excitation on adsorbed species. Specific parameters such as energy transfer rates and efficiencies can be extracted by monitoring the differential spectra. To date, most TA experiments on plasmonic systems have looked at the effect of plasmon excitation on proximal semiconductor materials. Studies on transient plasmon-molecule dynamics are challenging as the optical cross sections of plasmonic materials far exceed the absorption cross sections of molecules, meaning that the plasmonic response obscures the transient molecular signal. Therefore, directing a concerted effort towards the development of new plasmonic-semiconductor nanostructures for TA studies may help with the pursuit of better understanding the fundamental mechanism behind plasmon-mediated photocatalysis.[156-157]

TA spectroscopy of plasmon-semiconductor systems has been used to directly probe interfacial charge transfer reactions, as seen by Wu *et al.* in 2015.[158] This alternative route is plasmon-induced metal-to-semiconductor interfacial charge transfer transitions (PICTT), which combines the strong light-absorbing power of a plasmonic transition with the charge separation properties of a semiconductor-metal system (**Figure 2.10A**). Due to the strong coupling between the plasmonic material and semiconductor's electronic states, a new decay pathway is formed between the two materials. The first demonstration for the PICTT pathway was provided by TA studies involving colloidal quantum-confined CdSe-Au nanorod (NR) heterostructures, where the plasmon-induced hot electron transfer occurs within 20 fs (**Figure 2.10B**).[158] The plasmon decays directly by the transfer of an electron to CdSe, therefore the quantum yield of the charge separation process is independent of the excess energy above the CB edge, as long as the excitation energy is above the absorption threshold. The recorded high yield (>24%) of the electron transfer provides a potential bridge to evade the various competitive channels into which the plasmonic energy may partition, providing an alternative design protocol for fabricating efficient plasmon-mediated devices.

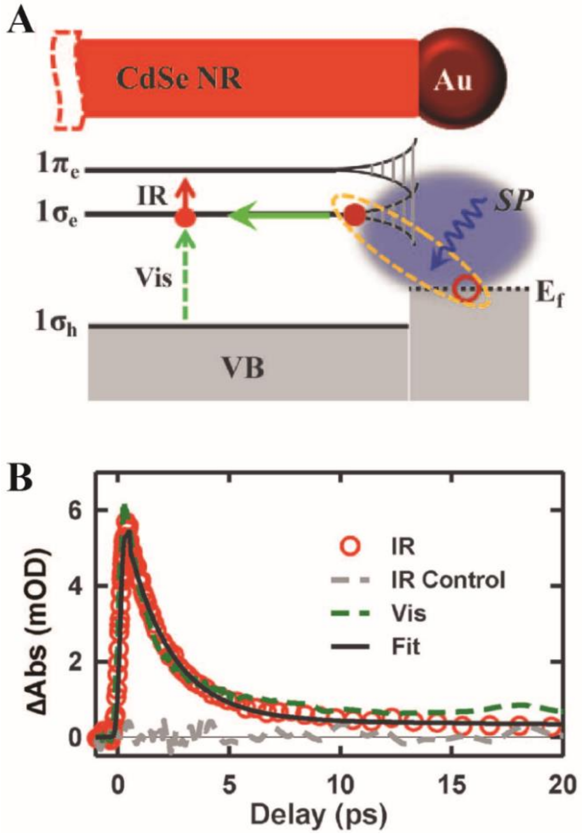

Figure 2.10 (A) Energy schematic of PICTT in CdSe-Au NR systems, where the Au tip is strongly damped. The green dashed arrow corresponds to the interband absorption that occurs in the visible and the red arrow indicates the intraband transition in the IR. (B) Kinetic trace highlighting the intraband absorption in the (probed at ~3000 nm, red circles) and the 1Σ-exiton-bleach (probed at ~580 nm, green line) after 800 nm excitation. From ref. 158. Reprinted with permission from AAAS.

TA spectroscopy has also been used to monitor energy transfer between a metal and semiconductor through a plasmon-induced resonance energy transfer (PIRET) process.[12, 46, 159-160] Here, rather than transferring electrons, the surface plasmon decays by donating its energy to a nearby species, analogous to Förster resonance energy transfer (FRET). PIRET was first directly observed by Cushing *et al.* in 2012, where they monitored Au@SiO$_2$@Cu$_2$O heterojunctions using TA.[46] The spectral overlap between Au and Cu_2O allows for PIRET through dipole-dipole interactions even with the SiO_2 barrier. By monitoring PIRET with TA spectroscopy, they observed PIRET with SiO_2 barrier thicknesses over which direct electron transfer would not be possible. The high energy transfer efficiency at and below the band edge has the potential to increase the Cu_2O photoconversion range, which is independent of the charge transfer process. The ability to transfer plasmonic energy to a blue-shifted region opens up a wide possibility for improving light-harvesting yields. Even for the smallest ~1.5 nm SiO_2 barrier, PIRET excited at 650 nm created ~1.4 times the number of charge carriers in Cu_2O as the above-bandgap excitation of the same incident flux, with the enhancement spanning the entire plasmon distribution. With proper modifications of the device aimed at minimizing the back transfer of energy by FRET, as well as maintaining a sufficient spectral overlap between the plasmon and thin film semiconductor, this method can be utilized in effective solar light harvesting devices over a wide spectral range with high yield.

These examples highlight the importance of employing TA to study plasmon-mediated processes to help elucidate the underlying mechanism for charge separation in plasmonic systems. The use of semiconductors to separate plasmon-generated charges may lead to more efficient harvesting of these charges for plasmonic photocatalysis. However, with the scope of the review article in mind, it is likely that present-day TA techniques will not readily surpass ultrafast Raman approaches in determining chemical mechanisms of catalytic steps in plasmonic photocatalysis. Yet, the results compiled with both of these highly-useful spectroscopic approaches could be further supplemented by employing or integrating non-spectroscopic methods, such as electrochemistry.

2.4.2 Electrochemistry

A number of electrochemical techniques have recently been employed to examine plasmon-induced processes, particularly with regards to understanding charge transfer and heating processes in the coupled plasmon-molecule system. By monitoring overpotentials, it is possible to determine energy levels of reactive intermediates.[10] In addition, scanning electrochemical microscopy (SECM), which monitors the current at an ultramicroelectrode as it is scanned across an active surface, has played a crucial role in determining the contributions of heating during plasmon-mediated processes.[161-162] Ultimately, electrochemical techniques can be employed to provide a wealth of information about the mechanism of plasmonic photocatalysis and to what extent electrons play a role in driving reactions.[163]

A common approach is to pair electrochemical potential control with dark field microscopy, which monitors the scattering from the plasmonic sample.[164-166] This has the advantage of providing precise control over the charge carrier density by altering the applied potential as well as allowing for active monitoring of the LSPR and its response to charge density changes.[165-167] Most of these techniques measure the charging of plasmonic nanostructures by adsorbing them to a conductive substrate, which is typically ITO.[165-166] Upon manipulation of the charge density of a plasmonic nanostructure, various changes to the plasmonic nanoparticle and the local environment can occur, including ionic rearrangement of the electrolyte solution, modifications to the particle morphology, and the ability to mediate specific chemical reactions at the particle surface.[168-170] As an example of the sensitivity of this approach, Collins *et al.* correlated a 0.02 nm blue shift in the LSPR to the addition of 110 electrons to a single gold nanorod in an ion gel device.[169] Dark field microscopy used in tandem with an applied electrochemical potential is clearly a powerful tool for monitoring electron transfer events by closely tracking the LSPR, which may allow for a deeper analysis of the rate limiting steps and catalyst-specific reaction mechanisms.

Additional modifications to this technique, such as including dynamic potential control and achieving single nanoparticle analysis, has allowed for an increased understanding of the electrochemical tuning of nanoparticles and the role of particle heterogeneity in the various responses.[165, 168] Byers *et al.* used hyperspectral dark field imaging to show that upon electrochemical tuning, a population of nanoparticles can undergo several different processes ranging from nanoparticle charging, as described previously, to electrochemical reactions, such as chloride ion oxidation and hydrogen evolution reaction (**Figure 2.11**).[168] These responses vary based on a combination of nanoparticle or nanoparticle/substrate properties that either favor nanoparticle charging or charge transfer. Depending on the local environment and nanoparticle nanoparticles also undergo irreversible or reversible electrochemical reactions which may include hydrogen evolution reaction under negative potentials or metal-halide formation under positive potentials.[168, 170] While there is still room for further understanding of the fundamental principles driving these phenomena, it is clear that these techniques can be utilized to illustrate a picture of the chemistry occurring around plasmonic nanostructures.

In addition to monitoring how adding or removing charge can manipulate plasmonic behavior, electrochemical techniques can also be used to monitor plasmonic photochemical reactions. When the plasmons are intentionally photoexcited with an external source, the electrons in the systems undergo a perturbation and the photocurrent of an integrated plasmonic device or overpotential changes for the half reaction can successfully be recorded. For solar water splitting, the plasmonic electrochemical cell can be modified such that either the hydrogen evolution reaction is plasmon-driven or the device can be modified to form a plasmonic photoanode where the oxidation reaction occurs.[10, 34] For example, Lee *et al.* built a plasmonic photoanode capable of splitting water by modifying

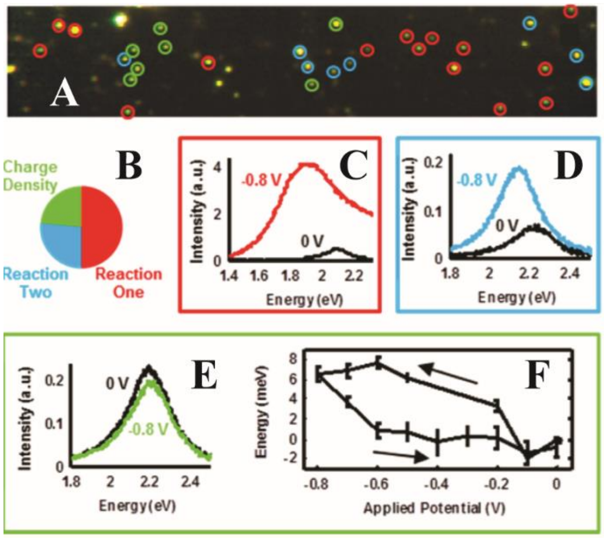

Figure 2.11 Heterogeneity observed during electrochemical tuning of individual gold nanoparticles on ITO. (A) hyperspectral dark field image of gold nanoparticles at open circuit potential (B) organization of gold nanoparticles into three categories based on behavior during potential scan with corresponding spectral response of a nanoparticle for (C) reaction one (irreversible electrochemical reaction), (D) reaction two (reversible electrochemical reaction), and (E) charge density where electrons are added to the gold nanoparticle. (F) LSPR shift reported as energy (meV) as a function of potential scanned for seven individual nanoparticles averaged together. Figure reprinted with permission from ref. 168, https://pubs.acs.org/doi/abs/10.1021/jp504454y. Copyright 2014 American Chemical Society.

gold nanorods. In this device, they successfully separate the hot carriers and use the hot holes to generate O_2 from water. When they compare the measured photocurrent of their device with the production of H_2, they can relate the various kinetics they observe to cell efficiency.[10] Since then, multiple groups have performed similar measurements where the enhanced photocurrent upon illumination due to integrated plasmonic nanostructures is used as a metric for device efficiency towards solar water splitting.[34, 171-173] These efforts are excellent demonstrations of the novelty and the potential impact of utilizing the power of plasmonic photocatalysts to mediate chemical processes that are relevant to society today.

Many of these studies also use cyclic voltammetry (CV) to measure how illumination may affect the oxidation or reduction reactions of a redox couple. CV is an electrochemical measurement in which the current is monitored as the working electrode is ramped linearly and cycled through a potential range.[163] In plasmon-enhanced photochemical reactions, illumination of the cell leads to several deviations from traditional CV characteristic traces, such as discrete shifts in the onset potential for the half reactions and an increase in the photocurrent, which provide useful information pertaining to the energetic barriers for the reaction.[174] Additionally, the redox energies for a studied molecule can be significantly altered by adsorption to the plasmonic material, which is observable in the distinct formation of new features in the CV.[175] Quantifying the changes observed in CV upon illumination of a plasmonic electrochemical cell may help identify how plasmons enhance and modify the observed reactions. However, these techniques focus on ensemble measurements of the system. Due to the potential heterogeneity of plasmonic samples, techniques which measure a smaller subset of the system are necessary to unravel the contributions of different mechanisms.

Scanning electrochemical microscopy (SECM) uses an ultra-microelectrode or a nanoelectrode to sample a more localized environment at interfaces as compared to other electrochemical techniques. SECM probes surface reactions and can provide information regarding electron transfer kinetics. For example, Yun *et al.* separated the individual contributions of hot carriers and thermal effects for the plasmon-driven oxidation of ferrocyanide to ferricyanide.[161] They controlled the

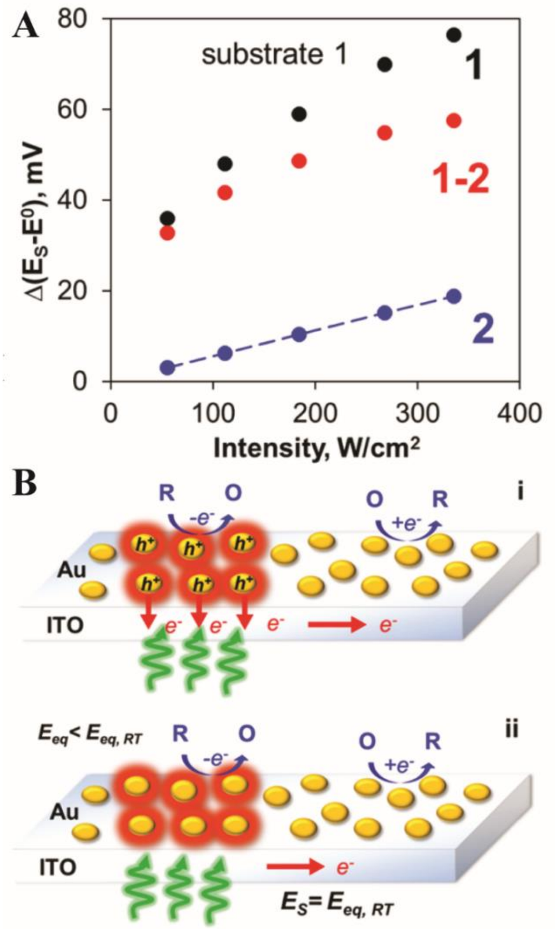

Figure 2.12 Proposed mechanisms for photo-induced oxidation based on contributions of hot holes and thermal effects. (A) Isolating hot hole contribution for photo-induced oxidation by comparing how the reaction potential changes at various laser intensities. Substrate 1 (black) contains contributions from hot holes and heating, substrate 2 (blue) only has thermal contributions, hot hole contribution for substrate 1 (red) is isolated by subtracting out the thermal contributions. (B) Pictorial depiction of proposed mechanisms (i) hot hole generation and (ii) thermal contribution leading to altered equilibrium potential of redox couple. Figure reprinted with permission from ref. 161. Copyright 2018 American Chemical Society.

reaction by holding the electrodes at a fixed potential at various regimes where the hot carriers and thermal effects worked synergistically or competitively (**Figure 2.12**). Using this technique, they were even able to quantify the degree of heating that occurred during the plasmon-driven oxidation of ferrocyanide.[162] For many plasmon-enhanced chemical reactions, the ability to probe surface reactions and measure the surface-dependent current changes allow for a better understanding of the underlying mechanisms which influence plasmon-mediated photochemistry.

Although SECM probes a smaller population of a plasmonic system, it is still an ensemble measurement due to the heterogenous nature of the plasmonic substrate. With the heterogeneity of plasmonic nanostructures and the utility of site-specific catalytic activity, techniques with higher spatial resolution may be necessary. One approach may be to couple electrochemical techniques, such as sample biasing, with techniques like SERS or TERS, which may aid the tracking of electron transfer events at the molecular level.[176] However, it is necessary to characterize the changes in TERS and SERS signals under these conditions as shown by Kurouski *et al.* and Di Martino *et al.*, where depending on changes of the LSPR due to electrochemical tuning or changes between the redox couple, the Raman signal magnitudes can diminish or disappear.[18, 177] Ultimately, the development of an electrochemical integrated TERS technique may be an optimal route for explaining these phenomena.

Electrochemical techniques hold promise for elucidating plasmon-mediated reactions especially with their ability to manipulate and monitor the flow of electrons and the resulting chemical effects, as shown in the above examples. These techniques face some difficulties due to the ensemble nature of these measurements and the fact that majority of these studies are performed with well-understood electrochemical reactions. Although broader applications of these techniques to other plasmon-mediated reactions may be challenging, the information that may gathered from such studies would greatly benefit the understanding of plasmon-mediated processes and their underlying mechanisms.

2.5 Outlook

The maturation of the above experimental techniques, both spectroscopic and electrochemical, has been instrumental for the advancement of new applications and fundamental insight in the plasmonics field. Enormous strides have been made in the past decade, as evidenced by the exceptional growth in the number of plasmonically-powered processes. However, there is still crucial quantitative information that needs to be extracted to help propel plasmon-mediated catalysis towards becoming a competitive and rational option for industrial applications. To help confront these elusive critical parameters in our collective knowledge, we would like to briefly highlight a few technical approaches that clearly hold abundant promise or may be fruitful to explore.

The experimental approaches covered in this review have focused on spectroscopic and electrochemical characterizations of interactions between plasmonic nanostructures and molecular species. These techniques have a number of advantages which make them well-suited for understanding plasmonic photocatalysis, particularly due to their ability to probe the molecular response of the evolving coupled system. However, there are a number of other experimental approaches that have great promise for understanding the mechanism of plasmonic photocatalysis. Magnetic resonance approaches have recently found great success as a characterization technique for the growth and evolution of plasmonic particles,[178] and the molecular specificity could find great use in quantifying and tracking the progress of some plasmon-driven reactions. Other experimental approaches such as EPR, time-resolved terahertz spectroscopy, or pump-probe infrared spectroscopy could also provide new insight into the mechanism of plasmonic photocatalysis.

While this review has focused on experimental approaches to monitoring plasmonic photocatalysis, theory and computational work has guided much of the current understanding of the decay processes and branching ratios in molecular-plasmonic systems, and many of the experimental interpretations presented here would not be possible without theoretical support. A major challenge in furthering theoretical approaches to the study of plasmon-driven photocatalysis lies in the large scale of the system, coupled with the importance of quantum mechanical effects and difficulties in determining the landscape of highly reactive molecular potential energy surfaces. A 20 nm diameter gold sphere contains ~60,000 gold atoms, some of which may be strongly coupled and have significant wavefunction overlap with adsorbed molecular species. High level quantum mechanical calculations on a system of this magnitude are generally intractable with current processing power. However, a number of reasonable approaches have led to significantly improved understanding of these large and complex systems. For example, work by the Nordlander group has provided quantitative values for the hot carrier energy distribution,[3] and the relaxation pathways and dynamics of these photoexcited carriers.[179] On the other end of the spectrum, work by the Carter group has applied embedded correlative wavefunction approaches to calculate energy levels of adsorbed molecular species, which has been highly effective at understanding the mechanism of some plasmon-induced processes,[35, 180] and in guiding the design of more efficient plasmonic photocatalysts. This approach has recently been applied to complex multistep multielectron reactions such as N_2 dissociation.[181-182] Recent theoretical work aimed at understanding the complete and strongly coupled molecular-plasmonic system includes atomistic electrodynamics and quantum mechanical models,[183-184] many-body Green's function formalism approaches to probe quantum emitters coupled to plasmonic systems,[185] and combination of Drude model plasmonic systems with TD-DFT molecular calculations,[186] among many others. There are many exciting possibilities for future directions for theoretical models of plasmonic photocatalysis, particularly with the incorporation of methods to track reactive molecular potential energy surfaces, such as the *ab initio* multiple spawning approach,[187] which has been highly successful in looking at reaction dynamics of molecular species in vacuum.

Although the recent focus has been directed towards engineering useful plasmonic nanostructures to serve as catalysts, there is an immense amount of promise in integrating traditional catalysts to enhance the practical usage of plasmon-mediated catalysis. With this mindset, efforts are currently being made to develop plasmon-metal catalyst coupled systems to effectively improve the metal catalyst's general efficacy. For instance, Swearer *et al.* synthesized a heterometallic antenna-reactor complex composed of an Al nanocrystal (AlNC) antenna and Pd catalytic nanoparticle to initiate highly-selective photocatalysis.[14]

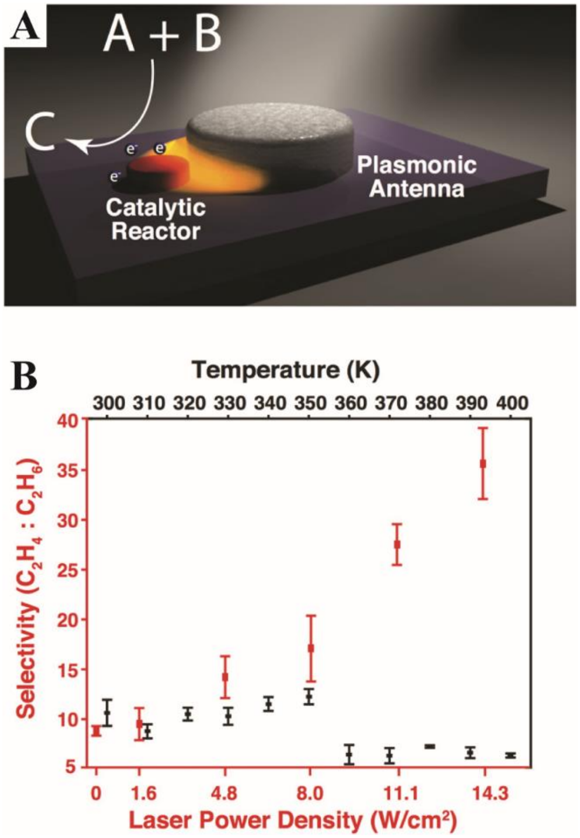

Figure 2.13 Plasmon-mediated photocatalytic reactions using a heterometallic antenna-reactor complex. (A) Cartoon depiction of the coupled AlNC-Pd nanoparticle system. (B) This fabricated substrate is capable of achieving a high-level of chemical selectivity, reaching a maximum 40:1 relative selectivity in ethylene:ethane production. Figure modified with permission from ref. 14, Copyright 2016 National Academy of Sciences.

This reactor complex is driven by the direct coupling of the plasmonic AlNC with the Pd nanoparticle, which dramatically enhanced the absorption character in the catalytic metal. A depiction of this nanostructured architecture can be seen in **Figure 2.13A**. The enhanced production of HD during H_2 dissociation was more strongly correlated to the optical wavelengths that were on resonant to the AlNC's absorption cross section, clearly demonstrating the plasmon's ability to substantially enhance the Pd nanoparticle's ability to facilitate a photocatalytic reaction. Improved selectivity was also achieved when acetylene was added during H_2 exposure. The authors noted a remarkable 40:1 increase in the relative selectivity of ethylene:ethane production (**Figure 2.13B**). Ultimately, their work launched a new wave of studies tailored towards engineering similar reactor complexes that are fueled by a near-field coupling between a traditional metal catalyst and plasmonic material. Original and inventive design such as this is essential for identifying new pathways for refining the present-day attempts of selective plasmon-mediated photocatalysis.

A practical and rational integration of plasmon-mediated photocatalysis into widespread applications may be on the horizon, as the recent findings and scientific advancements have been heavily influential for highly efficient plasmonic catalytic platforms. To achieve this goal, it is imperative to direct a united front towards understanding the mechanism of plasmon decay and the subsequent preferential partitioning of the desired energy. Throughout this review, we hope the readers have grown aware of the non-trivial balance between this partitioning, as the plasmonically-generated hot carriers, thermal elevations, and enhanced local electric fields can all play a role in mediating a given chemical reaction. Once the necessary understanding of this dynamic mechanism is obtained, we believe the field will find great success in designing highly-tunable and selective plasmonic catalytic systems to carry out significant light-driven chemical reactions.

Chapter 3

Competition Between Reaction and Degradation Pathways in Plasmon-Driven Photochemistry

Reprinted with permission from the manuscript by James L. Brooks and Renee R. Frontiera *J. Phys. Chem. C*, 2016, 120(37), 20869-20876

3.1 Overview

Plasmonic materials are exciting candidates for driving photochemical reactions, as they couple strongly with light across a wide range of the electromagnetic spectrum and can dramatically impact the photophysical properties of proximal molecular species. Plasmons have been shown to drive a number of photochemical reactions, but a detailed understanding of the mechanism is lacking in many cases. Here we investigate the effects of plasmonic field enhancement of the plasmon-driven conversion of 4-nitrobenzenethiol to 4,4′-dimercaptoazobenzene. By tuning the ensemble-averaged field enhancement of a plasmonic substrate, we quantify how the reaction yield and rate depend on the magnitude of the electric field. Surprisingly, we find no correlation of increased reaction rate or yield with greater field enhancement. Kinetic analysis of the reaction rate constants reveals a wide range of values, indicating that plasmonic excitation is not the rate-limiting step in this system. Additionally, we identify a competing degradation pathway that significantly contributes to the loss of reactant. This work identifies several factors that are critical in determining the overall efficiency of a plasmon-driven process and should help to lead to optimally designed plasmonic photocatalytic systems.

3.2 Introduction

The ability to focus and amplify a wide range of the electromagnetic spectrum makes plasmonic nanostructures a powerful mechanism for driving photochemical reactions.[72, 188-190] When adsorbed within highly enhancing electromagnetic fields, certain analytes are capable of undergoing molecular conversions that are inaccessible in the absence of the plasmonic substrate. Recent studies have shown plasmonic materials can be utilized as a photocatalytic platform to induce a wide variety of photochemical reactions. Work has been done toward optimizing specific photoreactions, such as water splitting,[11, 34] dissociation of H2,[35, 191] and the photoreduction of CO_2 into hydrocarbons[192] on plasmonic nanostructures. These investigations emphasize the potential of plasmon-driven photoreactions and their ability to trigger a variety of otherwise unfavorable chemical reactions. However, the mechanism of plasmon-driven photocatalysis is still unclear for a number of systems. Plasmon-driven photoreactions may be fueled by a number of factors, such as hot electron transfer,[35, 106, 191, 193] an enhanced thermal environment,[32, 194-195] and/or increased scattering. Because of the varying amplitude of plasmonic electromagnetic field enhancements in a typical heterogeneous sample,[92] working in concert with an additional thermal enhancement phenomenon, quantitative analysis of the plasmon-driven photochemical reaction can be challenging. While the range of successful plasmon-driven processes is continually expanding, detailed mechanisms of plasmonic photoreactivity are lacking.

Surface-enhanced Raman scattering (SERS) is a promising technique for probing the mechanism of plasmon-driven catalysis, as it is a surface-specific molecular technique that is intrinsically sensitive to probing the regions of high field enhancement in a given plasmonic substrate. Considerable evidence supports an electromagnetic enhancement as the dominant component in the SERS enhancement mechanism.[2, 17, 196] This electromagnetic enhancement is produced from the localization and amplification of an incident electromagnetic wave. When working in tandem with a chemical enhancement, which involves changes to the adsorbates' electronic states due to chemisorption,[197] SERS enhancement factors (EFs) are typically in the range of 103–108 for standard SERS substrates and can be higher ($>10^8$) for well-constructed and high-performing SERS substrates.[93]

The overall enhancement factor of a SERS substrate depends on the ensemble-averaged distribution of hot spots.[93] These hot spots are nanoscale junctions or crevices between particles or nanosized features, which serve to enhance the electromagnetic field by several orders of magnitude. As the ensemble-averaged SERS enhancement factor scales approximately as the increase in the electromagnetic field to the fourth power, or $|E/E0|^4$,[2, 198] small changes in the field enhancement can have a dramatic effect on the overall SERS intensity. Tiny alterations to the structure of the plasmonic surface, down to the atomic-scale features, can affect the electric field enhancement and, thus, SERS signal magnitude.[199] Therefore, most plasmonic surfaces, when used for ensemble-averaged measurements, exhibit a wide distribution of enhancement factors.

The SERS substrates used here, fabricated through nanosphere lithography methods,[200-201] have been previously characterized in terms of the hot spot distribution and the contribution of various hot spots to the overall signal.[92] Surprisingly, fewer than 1% of the hot spots account for more than 25% of the overall SERS signal, because of the extremely enhancing nature of these regions. Therefore, the resulting Raman scattering is generated from an ensemble of the most enhancing hot spots.

In this study, we investigate the effects of field enhancement on the plasmon-driven photoreaction of 4-nitrobenzenethiol (4-NBT) to 4,4′-dimercaptoazobenzene (DMAB), as depicted in **Figure 3.1a**. When 4-NBT is adsorbed to the surface of a plasmonically active material, its photoconversion to DMAB is accessible with several plasmonic materials, such as gold, silver, and copper,[103, 105-106] and a wide range of excitation wavelengths and laser powers.[109] Previously published research has tracked this photoreaction with SERS, tracking the growth of the DMAB photoproduct and decay of the 4-NBT reactant as a function of time.[104, 202-203] These studies have typically been performed on aggregated colloids in solution, in which it can be challenging to tune the field enhancement without changing other fundamental characteristics of the substrate.

Here, we use a gold film-over-nanosphere (AuFON) substrate to probe the 4-NBT photoreaction's rate and yield as a function of the SERS enhancement factor. A common perception for plasmon-driven photoreactions is that more field enhancement should lead to a higher reaction yield or efficiency. However, this assumption has yet to be conclusively demonstrated in practice. Our work shows that competing processes, like molecular degradation, can play a significant role in the dependence of the reaction yield on electric field magnitude. Quantifying the rate and yield of various processes that adsorbed molecular species may undergo upon plasmon excitation should ultimately help in the rational design of highly efficient plasmonic catalytic systems.

3.3 Methods

3.3.1 AuFON Substrate Fabrication

AuFON substrates were prepared by following previously published procedures.[201] First, glass coverslips (Fisherbrand, 18 mm) were thoroughly cleaned with an acid piranha solution followed by base piranha treatment. The solutions consisted of a 3:1 mixture of concentrated H2SO4 and 30% H_2O_2, and a 5:1:1 mixture of H_2O, concentrated NH_4OH, and 30% H_2O_2. After being cleaned, the glass substrates were rinsed thoroughly with deionized water.

Polystyrene microspheres 800 nm in diameter (Sigma-Aldrich, LB8) were diluted to 5% by volume in Millipore ultrapure H_2O (18 MΩ); 7.5 μL of the polystyrene solution was drop-coated and manually dispersed across the surface of the glass coverslip. The solution was allowed to evaporate under ambient conditions, and the polystyrene microspheres formed into a close-packed monolayer.

Approximately 200 nm of gold was deposited (5 Å s^{-1}, 1.5×10^{-3} Torr) on the polystyrene-coated substrates using a PVD sputtering system (AJA ATC 220). The substrates were rotated at 16 rpm during the deposition process. Following gold deposition, a saturated (∼200 μM) solution of 4-nitrobenzenethiol (4-NBT) in deionized (DI) H_2O was drop-cast onto the AuFON substrates and allowed to dry. The AuFON substrates were not rinsed after incubation to avoid any delamination of the polystyrene monolayer from the glass slides. Because of the high concentration of 4-NBT deposited on the substrates and the strong affinity of the thiol for the gold surface, we assume that the molecules undergo close packing in a near monolayer (surface coverage of 3.2×10^6 molecules/μm^2),[204] with additional 4-NBT molecules present in a hydration layer on the surface of the gold substrate.

3.3.2 Visible–Near-Infrared (Vis–NIR) Spectroscopy

Localized surface plasmon resonance (LSPR) extinction measurements were taken with a home-built system. LSPR measurements were taken at a range of sample positions, to quantify the heterogeneity in field enhancement across the relevant optical range used in Raman experiments. Light from a quartz tungsten–halogen lamp (Thorlabs, QTH10) was directed through an uncoated aspheric condenser collimating lens toward the substrates. The white light was focused onto the substrate with a 60 mm focal length lens at a 90° geometry. The resulting scattering light was passed through a 25 mm focal length lens, followed by collimation (Thorlabs, F240SMA-780) into a 50 μm core diameter, 0.22 NA optical fiber (Thorlabs, M14L05). An Ocean Optics USB4000 spectrometer was used for detection. The data acquisition time for each collection was 4 ms.

3.3.3 Raman Spectroscopy

Raman spectra were recorded by using a 785 nm Innovative Photonic Solutions diode laser. The beam was directed through a 30/70 beam splitter (CVI Laser) and focused to a 33 μm^2 spot size with a power of 40 mW onto the substrate with an infinity-corrected objective (Olympus Ach 10×, 0.25). The collection was performed in a 180° backscatter geometry, and the scattered radiation was redirected through the beam splitter and sent toward the detection system, consisting of a spectrograph (Acton SpectraPro 2500i) with a

CCD detector (Princeton Instruments, PIXIS 400BX). The acquisition time for each frame ranged from 50 to 100 ms, depending on the sampled region's enhancement factor. At least 1000 consecutive frames were collected for each run.

3.3.4 Characterization of AuFON Substrates

An enhancement factor (EF) was calculated for each sampled region of the AuFON substrates. This value is calculated using the equation[93]:

$$EF = \frac{I_{SERS}/N_{surf}}{I_{NRS}/N_{vol}}$$

where I_{SERS} and I_{NRS} are the Raman intensity of 4-NBT's 1074 cm^{-1} shift recorded on the AuFON substrate and in solution, respectively. N_{surf} is the number of molecules adsorbed on the substrate and N_{vol} is the number of molecules in the sampled volume for the normal Raman collection. Raman cross-sections for 4-NBT and cyclohexane (reference standard) were collected from literature.[197] A surface correction factor of 2 was applied to N_{surf} in order to account for the additional molecules adsorbed to the increased surface area due to the hemispherical shape of the AuFONs. Further details for calculating the SERS EF for these substrates can be found in Appendix A.

3.4 Results and Discussion

A benefit of using the AuFON substrates in this study is that random variations in the sphere packing will alter the observed SERS enhancement factor (EF), which is an ensemble average of the enhancements in the probed region. By randomly varying the number of defects per area in different spatial locations in the AuFON substrates, we are able to follow the 4-nitrobenzenethiol (4-NBT) plasmon-driven reactions in regions of variable field enhancement. This field enhancement can be easily quantified through the magnitude of the SERS signal. Defects in sphere packing can cause changes in the localized surface plasmon resonance (LSPR) of the probed region, resulting in an increased/decreased extinction or broadening at the excitation wavelength (**Figure 3.1b**). As the ensemble-averaged SERS enhancement factor depends of the LSPR magnitude at both the excitation wavelength and the Raman scattering

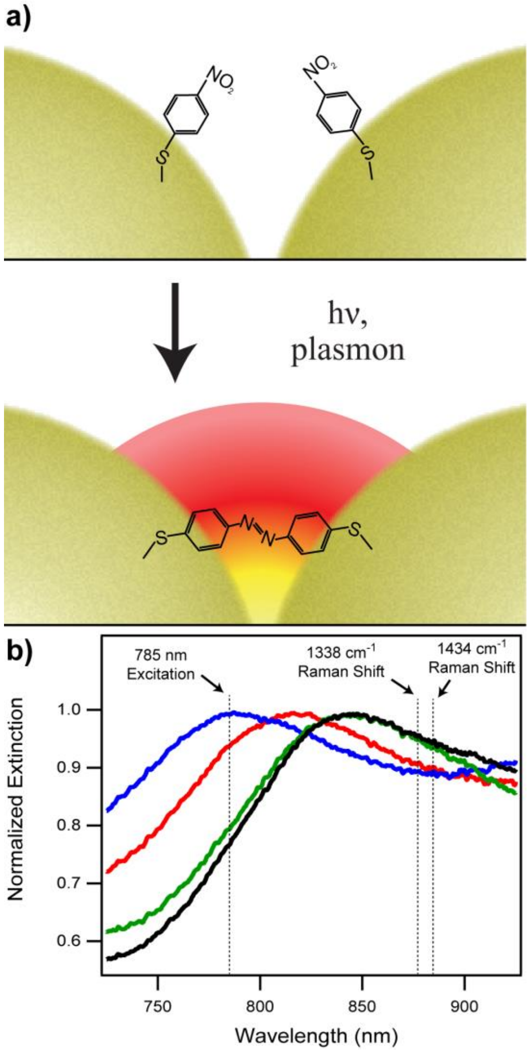

Figure 3.1 (a) Depiction of the plasmon-driven conversion of 4-nitrobenzenethiol to 4,4’-dimercaptoazobenzene. (b) Localized surface plasmon measurements of the SERS substrates. Different spots on the surface have varying plasmon resonance wavelengths, affecting the SERS enhancement factor and overall electric field enhancement.

wavelength, any changes in the LSPR frequency, line width, or amplitude may affect the observed enhancement factor. The 785 nm excitation wavelength is indicated in **Figure 3.1b**, along with scattering wavelengths for two key vibrational modes monitored during the photoreaction. By collecting numerous, discrete acquisitions at different spatial positions across the AuFON substrates, we sample a range of ensemble-averaged SERS EFs that are used to drive the 4-NBT photoreaction. Here, we used a range of EFs from 5.11×10^6 to 3.35×10^7.

Figure 3.2 displays the time-resolved Raman spectra of the plasmon-driven 4-NBT photoreaction. At the start of the measurement, the observed Raman peaks can all be assigned to the 4-NBT reactant. In particular, we focus on the 1338 cm^{-1} mode, highlighted in red, which is assigned to the NO_2 symmetric stretching vibration of 4-NBT.[205-206] During irradiation, we observe the formation of new product peaks at 1140, 1388, and 1434 cm–1, highlighted in green. These features

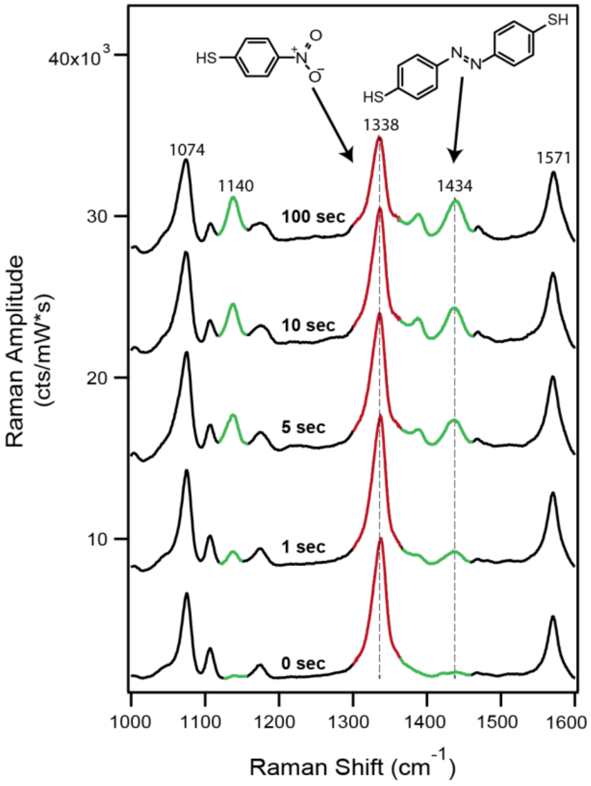

Figure 3.2 Time-resolved SERS measurements during the plasmon-driven conversion of 4-nitrobenezenethiol to 4,4'-dimercaptoazobenzene. The reactant peak at 1338 cm^{-1} decays and the product peak at 1434 cm^{-1} grows in during the SERS measurement.

represent the rapid formation of DMAB, which is clearly visible in these traces after irradiation for 1 s. No intermediates are observed in our spectra. As the reaction proceeds, the intensity of the DMAB peaks increases, while the intensity of the 4-NBT peaks decreases. We chose to use the 1434 cm^{-1} peak as being representative of product growth kinetics, as this peak has previously been assigned to the symmetric azo bond stretch found in DMAB.[207]

Because of small changes in the field enhancement across our substrates, we are able to probe the ensemble-averaged dynamics and yield of the 4-NBT to DMAB dimerization reaction as a function of the SERS EF. We used the SERS EF to estimate the plasmonic field enhancement, using the assumption that the ensemble-averaged SERS enhancement factor scales as the electric field to the fourth power.[2, 198] By initiating and monitoring the reaction at various sample positions, and using the overall SERS magnitude to estimate the field enhancement, we can determine the effect of field enhancement on the photoreaction. We probed the photoreaction at 29 different locations across two separate AuFON substrates.

Figure 3.3 shows the overall change in peak amplitudes during the decay and growth processes as a function of the sampled SERS EF. The change in peak amplitude was assigned as positive for any growth processes and negative for any decreases in peak amplitude. The slopes of the product growth and reactant decay are $(3.5 \pm 0.7) \times 10^{-5}$ and $(-3.6 \pm 0.5) \times 10^{-4}$, respectively. The R^2 values of the growth and decay processes are 0.48

and 0.63, respectively. **Figure 3.3** proves that the changes in both the reactant and product peak amplitudes are correlated to the localized SERS EF, as expected. As the molecules are bound to the gold surface, as the localized SERS EF of the sampled region increases, the magnitude of the resulting Raman signal of both product and reactant should also increase.

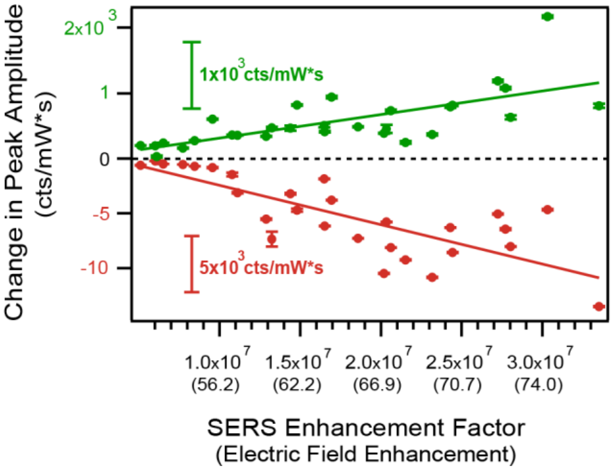

Figure 3.3 Total change in the reactant (red) and product (green) peak amplitudes as a function of the SERS enhancement factor. The y-axes for reactant and product are different in order to clearly highlight the correlation to the SERS enhancement factor.

Interestingly, the slopes for the reactant and product amplitudes as a function of field enhancement are different. The slope for the reactant loss is nearly an order of magnitude larger than that of product formation. This trend arises from both the reaction stoichiometry and the difference in Raman cross sections for the monitored modes of product and reactant. For the formation of a DMAB molecule to occur, the reduction of two adjacent 4-NBT molecules is required. However, the overall change in amplitude for each vibrational mode is heavily dependent on its Raman cross section. The loss or gain of vibrational amplitude will be more dramatic for larger Raman cross sections, which explains the large difference between the slopes in **Figure 3.3**. Off-resonance Raman measurements of the Raman cross sections for 4-NBT and DMAB and their derivatives are not available to provide quantitative support for this argument, but our work implies that the NO_2 symmetric stretch has a Raman cross section larger than that of the azobenzene N═N stretch.

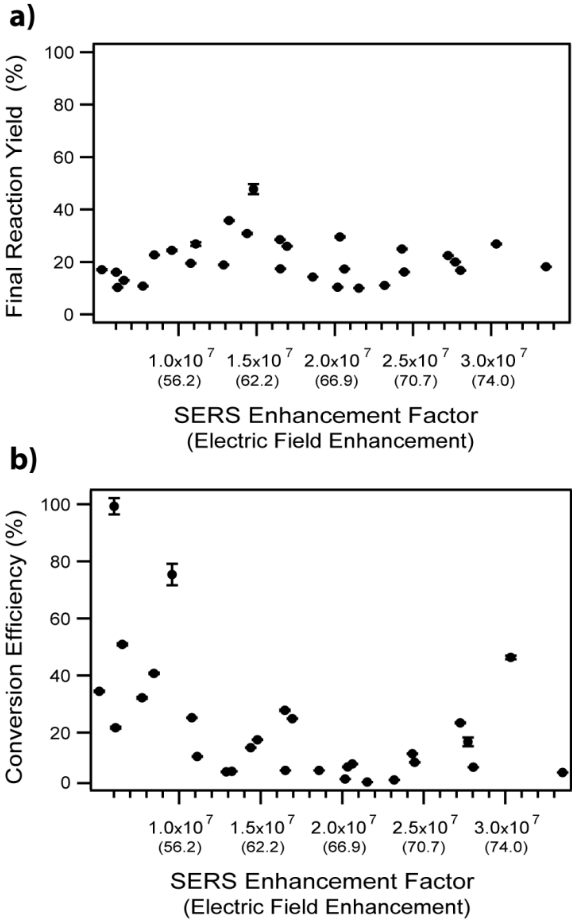

Figure 3.4 (a) The final reaction yield, which is the ratio between the final amplitudes of the product and reactant amplitudes, of the photoreaction and the dependence on the SERS enhancement factor. As the localized field enhancement increases, the reaction yield stays between 10 – 40%. (b) Dependence between the conversion efficiency, defined as a ratio between the amplitude changes of the product and reactant amplitudes, on the SERS enhancement factor. As the field enhancement increases, the reactant peak (1338 cm^{-1}) decays more significantly than the formation of the product peak (1434 cm^{-1}).

To provide insight into the difference in product growth and reactant loss in this plasmon-driven reaction, we considered the reaction yield and conversion efficiency of this reaction. In **Figure 3.4a**, we show the reaction yield for the system, defined as the ratio of the final Raman amplitude of the product to the final amplitude of the reactant. This is effectively a determination of the percentage of molecules that reacted out of the number of 4-NBT molecules that remain on the surface at the end of the measurement. To accurately account for the change in DMAB product amplitude, we subtracted away any signal that was present before laser exposure, which was never greater than 20% of the total. These reaction yields are plotted as a function of the SERS enhancement factor and electric field enhancement. Interestingly, as the field enhancement increases, we do not see an increase in the reaction yield. The reaction yield seems to be independent of the localized SERS EF with values ranging between 10 and 40% for all sampled regions. In all sampled regions, unreacted 4-NBT molecules are clearly visible.

The incomplete conversion of this reaction can likely be explained through steric hindrance. The 4-NBT molecules are immobilized on the gold surface and may experience a strong steric constraint during the photoreaction. For the reaction to occur, two adjacent 4-NBT molecules must be bound to the surface such that the nitro groups are in close proximity. If not, the plasmonic field enhancement will not drive the reaction, thus decreasing the overall number of 4-NBT molecules that undergo the photoconversion. A 10–40% reaction yield signifies that a majority of the 4-NBT molecules in the hot spots are not undergoing photoconversion and remain bound to the gold surface.

In contrast, the conversion efficiency as a function of SERS EF is not as straightforward. Here, we define the conversion efficiency as the ratio of the total growth of product divided by the total loss of reactant, in terms of their respective Raman peak amplitudes. Compared to the final reaction yield, the conversion efficiency focuses on how much depletion occurs in the reactant signal, rather than recording the final amplitude after the laser exposure is completed. As the localized SERS EF increases, the conversion efficiency decreases (**Figure 3.4b**). The efficiency ranged between 20 and 100% for SERS EFs below 10^7 and is typically lower for larger electric field enhancements.

It is reasonable to believe that as the localized electric field increases, the 4-NBT photoreaction should be more likely to occur and produce a higher yield and conversion ratio. It is believed that greater electric field enhancements should lead to increased levels of hot electron generation and transfer, a hotter thermal environment, and/or increased scattering, all of which are potential mechanisms for the 4-NBT plasmon-induced photoreaction. However, as shown in **Figure 3.4b**, after a certain minimal SERS EF ($\sim 10^7$) is sampled, the conversion ratio rapidly decreases. To explain this trend, an in-depth analysis of the reaction kinetics is required.

Because of the great enhancing capabilities of the AuFONs substrates, we were able to rapidly collect a large number of acquisitions during the initial phase of the photochemical reaction, which allowed us to closely follow the ensemble-averaged reaction kinetics. Three independent kinetic measurements, all conducted with different localized field enhancements, are displayed in **Figure 3.5**, with 26 additional measurements displayed in the Supporting Information. In all measured spots, we see a rapid growth of product features with a concurrent loss of Raman amplitude corresponding to reactant molecules. The observed kinetics vary widely in different regions of the substrate. For example, in panels a and b of **Figure 3.5**, the growth of the product, colored green, rapidly increases within the first 10 s, while in **Figure 3.5c**, product formation is slower. There is also a clear loss of reactant signal during product formation for all three traces.

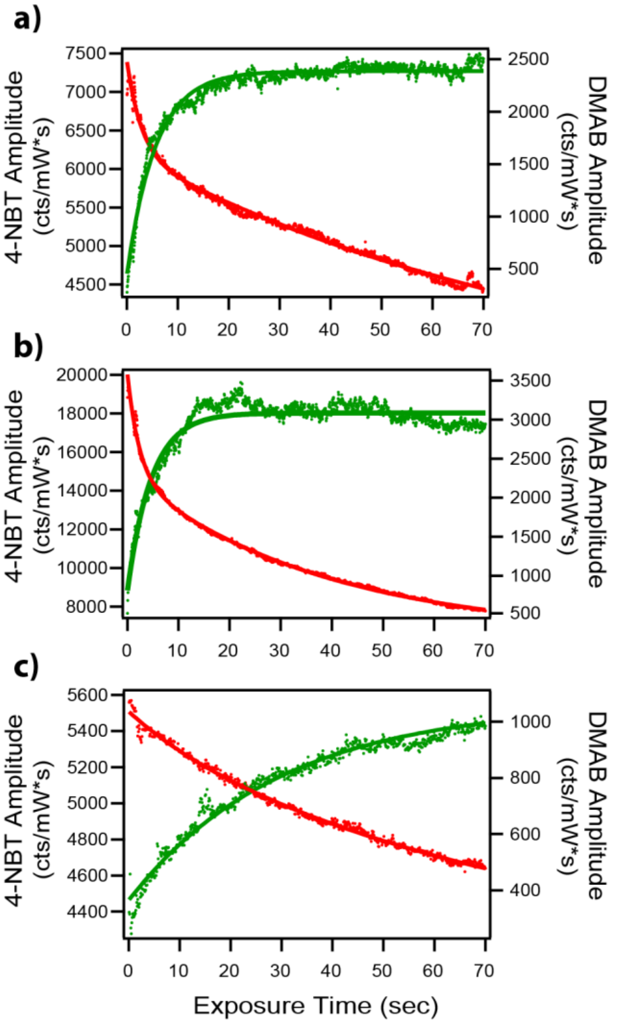

Figure 3.5 Reaction kinetics of the 4-nitrobenzenthiol to 4,4’-dimercaptoazobenzene plasmon-induced photoreaction. (a) The 4-NBT reactant amplitude rapidly decreases with a concurrent growth of product amplitude. At longer times, the reactant peak experiences an additional decay, while the product amplitude remains constant. (b) Similar to a, but with a slight decrease in the product amplitude at longer times (c) In this more weakly enhancing environment, the reaction occurs more slowly.

Figure 3.5a and **5b** highlight an interesting phenomenon during the photochemical process: the amplitude of both 4-NBT kinetic traces continues to decrease after the reaction takes place. This is particularly visible after ~30 s, when the 4-NBT amplitude decreases rapidly but the DMAB amplitude is essentially unchanged. We attribute the loss of the SERS signal to an additional pathway in the plasmon-driven reaction. The loss is likely due to degradation or desorption of a portion of the 4-NBT molecules, particularly those that are located in the highly enhancing regions probed by SERS. Because of the high field magnitudes in these regions, the molecules can undergo degradative processes, such as dielectric breakdown or molecular desorption. In **Figure 3.5b**, we also observe a small decrease in the amplitude of the DMAB product signal, indicative of a similar degradation process. While the magnitude of the DMAB signal decreased for only ∼17% (5 of 29) of studies, the 4-NBT reactant signal photodegradation was present for a majority of the experiments. The rapid decrease in the magnitude of the 4-NBT signal does not occur in **Figure 3.5c**, which had a lower ensemble-averaged field enhancement. In this particular region, 4-NBT loss occurs at a much slower rate and closely matches the DMAB product formation kinetics.

To investigate the effects of field enhancement on photoreaction and photodegradation rates, we fit kinetic traces for 29 different regions, all with different ensemble-averaged electric field enhancements. The DMAB product formation kinetics were fit to a single-exponential curve, as any degradation was typically quite small and did not affect the fit. The majority of the 4-NBT decay kinetics were fit to two exponential functions, representative of loss due to photoreaction and loss due to degradation. A small fraction of the 4-NBT kinetic traces were better fit to a single exponential, indicating either that one of the pathways was not present or that the rate constants for degradation and photoreaction were not well separated. These were not included in the analysis below because of ambiguity in the assignment.

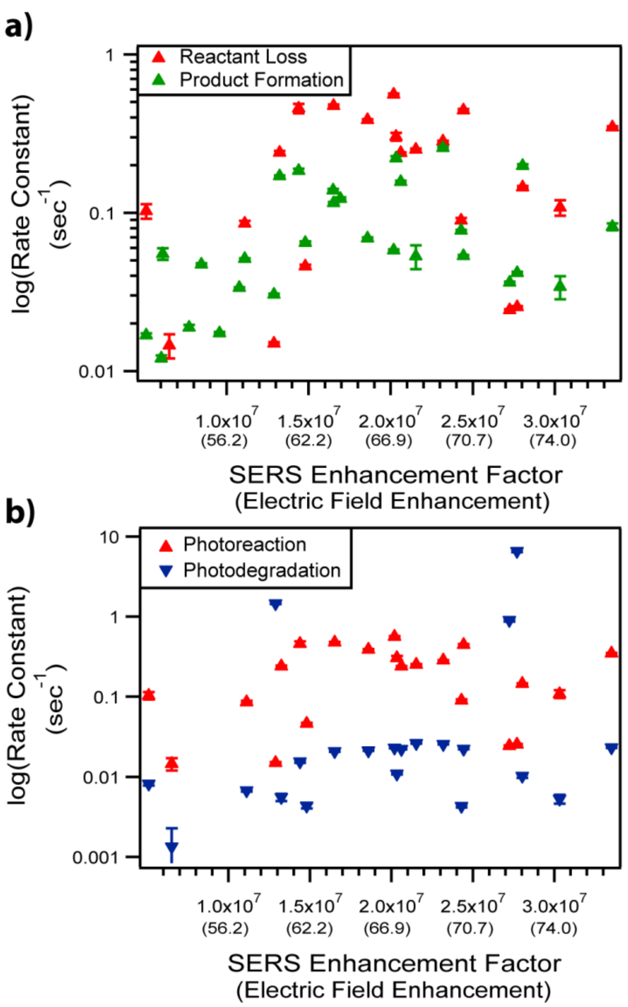

Figure 3.6 Rate constants for plasmon-induced processes. (a) Comparison of photoreaction rate constants for the loss of the 4-NBT reactant (red) and formation of DMAB product (green). (b) Comparison of photoreaction rate for 4-NBT (red) and photodegradation rate of 4-NBT (blue). All observed ensemble-averaged rates are independent of field enhancement for the range of enhancement factors probed.

Figure 3.6a shows the field dependence of the rate constants attributed to the photoreaction, as measured for both the reactant loss and product formation. The rate constants for reactant loss are consistently higher than those for product formation, although both show no clear correlation with the SERS enhancement factor. Therefore, the rate-limiting step for the 4-NBT to DMAB photoconversion is not dependent on the plasmonic field enhancement. The photoreaction rate is likely determined by a limited concentration of nearby protons, which are required for the initial reduction of the 4-NBT species. To reduce the nitro groups on 4-NBT, several studies have shown that the system requires protonation to generate the reaction intermediates.[108, 208-210] These protons likely come from the hydration layer on the surface of the gold,[211] and their availability limits the rate of the photoreaction. This implies that generation of protons is not driven by plasmon excitation.

The hydration layer also is responsible for the differences in photoreaction rate constants for the reactant and product. As this is a 2A → B reaction, we would expect that the reactant rate constant would be twice the value of the product rate constant. While the reactant rate constant is consistently larger than that of the product, a quantitative 2:1 relationship does not hold. Fitting the kinetics with constrained exponentials based on this relationship resulted in a number of poor fits. Given the high molecular concentration used in these studies, we likely have formed a near monolayer of 4-NBT molecules on the surface, with additional free 4-NBT molecules in the hydration layer above the gold surface. It is possible that a free 4-NBT molecule would react with a surface-bound 4-NBT molecule to form DMAB. As the SERS intensity decays exponentially away from the metal surface, any contributions to our SERS signal from free 4-NBT molecules in the hydration layer will be negligible. In this scenario, the observed photoreaction rate constants for the product and reactant would be the same, barring any observable intermediates. Given the heterogeneity of the sampled regions, the observed values for the ensemble-averaged rate constants indicate that the dimerization occurs through both surface-bound and free 4-NBT molecules.

In **Figure 3.6b**, we consider the field-dependent rate constants for degradation and photoreaction for the 4-NBT reactant. Rate constants were assigned to photoreaction when they were within a factor of 5 of the product formation rate constants. Again, there is no observable correlation with field enhancement for the range of SERS enhancement factors probed. Additionally, for all but two of the probed regions, the photoreaction rate constant was approximately an order of magnitude larger than the degradation rate constant. This implies that reaction is typically much faster than degradation, and that prolonged irradiation leads to photodamage. Thus, a careful consideration of the rate constants of desired plasmon-driven photochemical pathways is critical in evaluating the overall yield and efficiency of a given pathway.

3.5 Conclusions

In this work, we have investigated the electric field dependence on the plasmon-driven photoconversion of 4-nitrobenzenethiol (4-NBT) to 4,4′-dimercaptoazobenzene (DMAB). We used plasmonic substrates with a range of ensemble-averaged enhancement factors to determine how the catalytic reaction rate and yield depend on field enhancement. Surprisingly, we found that over the range of electric field enhancements probed, there was no relationship between the reaction rate and the localized field enhancement. Instead, the rate-limiting step in the 4-NBT reduction is not limited by plasmonic processes, but likely the accessibility to protons to create the necessary intermediates. Additionally, we identified a photodegradation pathway that may compete with the 4-NBT to DMAB plasmon-induced photochemical reaction. We see a decrease in the 4-NBT SERS amplitude indicating photodegradation with rate constants typically on the order of 10^{-2} – 10^{-3} s^{-1}. Fortunately, for a majority of sampled regions, this degradation typically occurs after the reaction has been driven to completion.

These results identify several factors critical when fabricating plasmonic catalysts designed for high yield and selectivity. Consideration of rate constants of competing processes is important, as degradation effects are generally more significant in regions of high field enhancement. For the particular reaction studied here, the photoreaction is typically faster than degradation, but in nearly all regions, loss of reactant due to degradation occurred. Additionally, the role of proton availability in the hydration layer is a key factor in the rapid photoreactivity. Thus, an ideal plasmon-driven reaction will optimize the orientation of all reactants in or near the plasmonic hot spot so that the photoreaction can occur before photodegradation. A careful consideration of the relevant rates of various photoinduced processes may be helpful when optimizing plasmon-driven processes for a number of different chemical reactions.

3.6 Acknowledgements

This work was supported by Air Force Office of Scientific Research MURI Grant FA9550-15-10022. A portion of this work was carried out in the Minnesota Nano Center which receives partial support from the NSF through the NNCI program.

Chapter 4

Plasmon-Mediated Intramolecular Methyl Migration

Reprinted with permission from manuscript by James L. Brooks, Dhabih V. Chulhai, Jason D. Goodpaster, and Renee R. Frontiera. To be submitted.

4.1 Overview

Plasmonic materials interact strongly with light to focus and enhance electromagnetic radiation down to nanoscale volumes. Due to this localized confinement, materials that support localized surface plasmon resonances are capable of driving energetically unfavorable chemical reactions. In certain cases, the plasmonic nanostructures are able to preferentially catalyze the formation of specific photoproducts, which offers an opportunity for the development of solar-driven chemical synthesis. Here, we present the first report of using plasmonic environments to induce an intramolecular methyl migration reaction, forming 4-methylpyridine from N-methylpyridinium. Using both experimental and computation methods, we were able to confirm the identity of the N-methylpyridinium by making spectral comparisons against possible photoproducts. This reaction involves breaking a C-N bond and forming a new C-C bond, highlighting the ability of plasmonic materials to drive complex and selective reactions. This work provides a new class of reactions accessible by surface plasmon excitation, and further adds to the growing library of accessible plasmon-mediated chemical reactions.

4.2 Introduction

Plasmonic materials are proving to be a promising platform for initiating and carrying out a wide-range of unique catalytic reactions.[9, 212-214] The optical excitation of a surface plasmon, which is the collective oscillation of the material’s free electron charge density, gives rise to the generation of dramatically-enhanced electromagnetic fields on the nanostructure’s surface.[44] Surface plasmons interact with incident radiation and are able to take that energy and partition it into multiple decay pathways.[38, 45] These pathways, in addition to the generation of the highly-enhanced local fields, include the non-radiative conversion of energy to an abundance of harvestable hot carriers and elevated thermal environments.[3, 72, 215] When molecular species are introduced to the surface, all of the possible decay pathways may interact with the analyte and initiate a chemical transformation. In fact, researchers have been successful in achieving significant light-activated plasmonic reactions, such as hydrogen dissociation,[35] water splitting,[11, 34, 216] carbon dioxide reduction,[31, 192] and the generation[27] and decomposition[15] of ammonia. These examples highlight the potential for integrating plasmonic materials into industrial-significant catalytic processes. However, these reactions are generally limited to achieving modest chemical reactions, such as chemical bond-breaking or performing single-step reactions.

One of the more exciting aspects of using plasmonic materials as light-activated catalysts is their ability to achieve a high-level of chemical selectivity. One excellent example of noteworthy chemical selectivity is the hydrogenation of acetylene using plasmonic antenna-reactor complexes.[14] In this study, Swearer *et al.* were able to obtain a maximum ethylene:ethane product ratio of ~35 with high laser densities. When compared to a traditional thermal heating production mechanism, which peaked a maximum selectivity of ~10, it is clear that plasmonic materials can provide the unique conditions to more effectively initiate certain selective chemical reactions, possibly through the role of hot carriers in the catalytic reaction.

Ultimately, a key goal in the advancement of light-activated plasmonic catalysts is developing practical applications of carrying out selective synthetic or redox reactions. Having direct control over the light-driven formation of a highly-selective final product, and bypassing unnecessary experimental steps, would be beneficial for portable energy conversion applications. As an example, alkyl migrations reactions serve as a common chemical process used to obtain the desired products in numerous selective synthesis procedures.[217-220] Currently, there have been no reports of using plasmonic materials to initiate and carry out an alkyl migration. In this study, we examine a selective intramolecular methyl migration that is activated by introducing an organic heterocyclic amine to strongly amplified plasmonic environments. The heterocyclic amine of interest contains a cationic pyridinium species, which has been demonstrated to play a key role in catalyzing CO_2 reduction in electrocatalysis.[221-223] Studying carrier transfer rates and lifetimes on reactive surface may prove to be relevant for better understanding its role in similar chemical reactions. Here, we use both spectroscopy and theory to identify the photoproduct structure, and to track kinetics following plasmon-excitation.

Surface-enhanced Raman spectroscopy (SERS) is a valuable spectroscopic technique that is inherently sensitive to the intense local electric fields produced by plasmonic materials.[66, 90] SERS provides an amplified Raman spectrum of analytes that are chemi- or physisorbed within the electric fields on the surface of the substrate. When exposed to an excitation source, the incident far-field electromagnetic radiation is tightly focused down to a nanoscale-level confinement in the near-field. These regions of amplified local fields are commonly referred to as hot spots. Hot spots typically form at the juncture between two nanoscale structures or at the crest of sharp, discrete features. In fact, it has been reported that metal film-over-nanospheres (FON), the substrates used during this study, can generate individual hot spots with enhancement factors, which is a quantitative description of the substrates ability to amplify the Raman scattering from its adsorbed analytes, reaching values $>10^{10}$.[92, 224] With its signal originating from the most intense hot spots,[92] SERS is an exceptional technique to induce a plasmon-mediated chemical reaction in the most enhanced environments on the plasmonic substrate.

Multiple studies have utilized the amplified SER spectra to identify the formation of new chemical species and better understand the mechanism fueling the plasmon-driven process. A majority of these reactions have been focused on a bimolecular dimerization of 4-nitrobenzenethiol or 4-aminobenzenethiol to 4,4'dimercaptoazobenzene.[20, 103-104, 106, 108, 118] In addition to this dimerization reaction, other studies have identified plasmon-driven cleavage reactions, such the N-demethylation of methylene blue[225] and the decarboxylation of 4-mercaptobenzoic acid.[226] Ultimately, the reports have been limited to the chemistry occurring at a single functional group or atom on the targeted molecule, and have primarily tracked bond-breaking processes.

Here, we follow the chemically-selective plasmon-mediated methyl migration on N-methylpyridinium (NMP) using AuFON substrates. By monitoring this reaction with SERS, we are able to identify and track the subsequent growth of the product species as it was generated on the surface. To determine the chemical identity of the plasmon-generated photoproduct, we collect the SER spectra of possible product species and compared their vibrational modes to the NMP photoproduct. We observe that the plasmon excitation is the rate-limiting step behind the production of 4-methylpyridine. Furthermore, we used the dressed-polarizability model of SERS to confirm our assignment of 4-methylpyridine.[183, 227-228] This work highlights the growing potential of using plasmonic materials to access and carry out selective chemical transformations and serves as an exciting addition to the ever-growing library of plasmonically-powered chemical reactions.

4.3 Methods

4.3.1 AuFON Substrate Fabrication

We oxygen plasma etched glass coverslips (Fisherbrand, 18 mm diameter, 0.13-0.17 mm thick) to treat the silica surface for nanosphere deposition. We rinsed the glass coverslips thoroughly with deionized water both before and after the plasma etching. We used a diluted solution of 600 nm diameter silica microspheres (NanoCym, 10% by volume) in Millipore ultrapure H_2O (18 MΩ). We drop-casted and manually dispersed 3 μL of the silica solution across the surface of the glass coverslip. The silica microsphere solution evaporated at ambient conditions and the spheres formed into a close-packed monolayer. Following the application of the silica microspheres, we deposited 200 nm of gold on the silica-coated substrates (16 rpm) using a thermal evaporation system (Denton Vacuum, DV-502). An image of the AuFON substrates is shown in **Figure 4.1**. We prepared a 350 μM solution of N-methylpyridinium iodide (Sigma Aldrich) in methanol and deposited 10 μL of the resulting solution on the AuFON for our SERS measurements.

We measured the localized surface plasmon resonance (LSPR) extinction spectrum with a UV-2600/2700 equipped with an integrating sphere attachment (Shimadzu). The data acquisition time for each collection was 4 milliseconds.

4.3.2 Raman Spectroscopy

We collected the Raman spectra by using a 785 nm Innovative Photonic Solutions diode laser. We directed the laser beam through a 30/70 beam splitter (CVI Laser) and focused to a 15.9 μm^2 spot size onto the substrate with an objective (Olympus Ach 10x/0.25). We performed the collection in a 180° backscatter geometry and redirected the scattered radiation through the beam splitter and towards the detection system, consisting of a spectrograph (Acton SpectraPro 2500i) with a CCD detector (Princeton Instruments, PIXIS 100BX). Our spectral acquisition times ranged from 60 ms – 1 sec, depending on the power used during the experiment. The intensities we reported throughout this manuscript were normalized with respect to the acquisition time and excitation power to provide a consistent and quantitative comparison between measurements.

4.3.3 Theoretical Calculations

We obtained all of the calculations presented in this paper with version 2018 of the Amsterdam Density Function (ADF) suite,[229-230] using the Becke-Perdew (BP86) exchange-correlation potential[231-232] and a triple-zeta Slater type basis set with two polarization functions (TZ2P) from the ADF basis set library. We calculated the normal modes analytically within the harmonic approximation and scaled the BP86 frequencies by a factor of 1.017 to account for anharmonic effects. We used the dressed-polarizability model[183, 227-228] to simulate all SERS spectra using both electric fields and field gradients. We obtained the local electric fields and field gradients from a model sphere to mimic surface roughness features ~3 nm.

4.4 Results and Discussion

To provide a spectroscopic description of the ensemble-averaged local field enhancement, we characterized the gold film-over-nanosphere (AuFON) substrates with UV-Vis-NIR spectroscopy (**Figure 4.1**). The collected extinction spectrum is the sum of the overall absorption and scattering events that the incident photons experience when interacting with the plasmonic substrate. Due to the substrate being a highly reflective material, we performed and reported the extinction spectra in terms of percent reflectance. The depletion in the reflectance spectrum, starting at ~740 nm and lasting beyond 1000 nm, corresponds to the presence of a broad localized surface plasmon resonance (LSPR). We

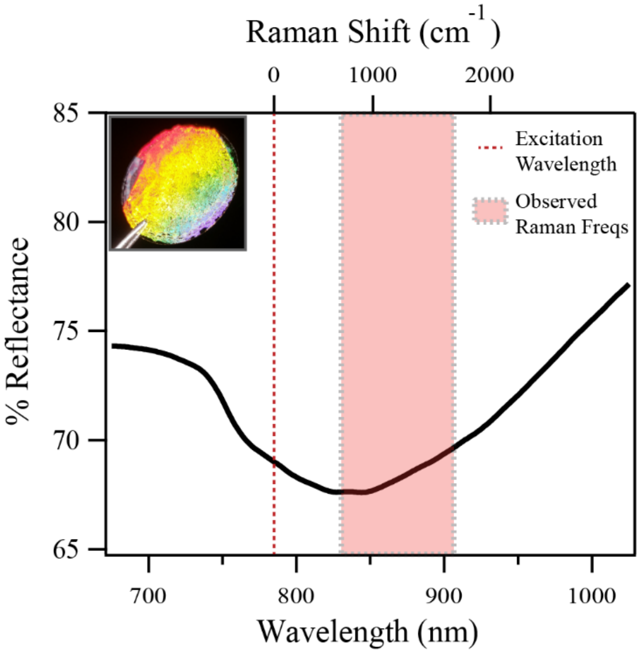

Figure 4.1 Ensemble-averaged far-field extinction spectrum of AuFON substrates. The presence of a localized surface plasmon resonance (LSPR) is depicted as a depletion in the measured percent reflectance. We performed these experiments with a 785 nm excitation source (dotted red line) and collected the observed Raman scattered photons collected between 830–905 nm (highlighted red region). A photograph of the AuFON substrates is shown as an inset in the plot.

configured our Raman detection system to collect Raman scattered photons between ~830 to ~905 nm when using a 785 nm excitation source. This spectral window allowed us to report Raman-active vibrational modes with frequencies between 700 – 1700 cm^{-1}. For optimal signal enhancement in ensemble-averaged studies such as this, it is ideal to design the SERS substrates to host an LSPR with a λ_{max} positioned between the excitation wavelength and resulting Raman scattered photons' wavelengths.[63] **Figure 4.1** highlights the spectral region of the LSPR that is responsible for coupling and amplifying the Raman scattered photons.

In this study, we deposited N-methylpyridinium (NMP) iodide in methanol onto the surface of the AuFON substrates. Once the methanol evaporated, we exposed the substrate to 785 nm laser light and collected the resulting SERS signal with short exposures as a function of time. Previous SERS experiments have confirmed the stability of the cationic NMP on metal substrates.[233] **Figure 4.2** displays the evolution of the plasmon-mediated formation of NMP to 4-methylpyridine. The initial SER spectra contain Raman vibrational signatures that correspond to NMP molecules chemisorbed to a gold surface. However, in less than a second, we identified the formation and subsequent growth of a previously unreported photoproduct in the SER spectra. We see the formation of new product peaks at 797, 1010, 1077, 1210, 1377, and 1620 cm^{-1}, all highlighted with red bars. We did not observe any intermediate species in the collected spectra. Over time, the transformation of NMP reaches a point of saturation and we observe no further changes in the spectra.

In addition to generating unique photophysical effects, such as hot electron and hole generation, plasmonic environments may provide the necessary environment to help promote unfavorable chemical alterations or transformations in certain molecular analytes. In this experimental design, the strongly-enhanced local electric fields, coupled with the presence of harvestable highly-energetic electrons and increased thermal environments, provided sufficient energy to the NMP molecules to undergo this plasmon-mediated chemical transformation. This is the first report that successfully identifies any type of plasmonically-powered transformation of NMP into a new chemical species. We hypothesize that the unique and dramatically enhanced local fields generated by the AuFON substrates provided the essential conditions to access the alternative reaction pathway.

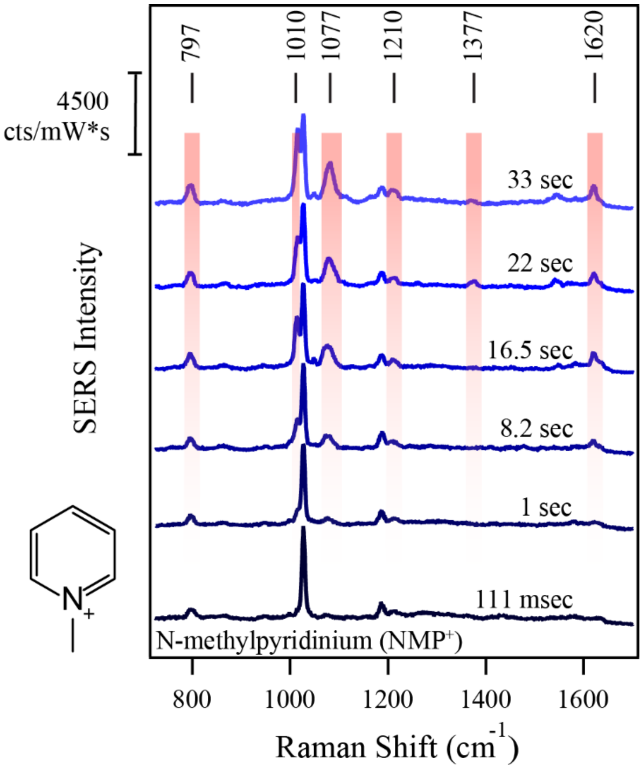

Figure 4.2 Evolution of time-dependent SERS measurements during the plasmon-mediated chemical conversion of N-methylpyridinium on an AuFON substrate. We identified the production of seven unique vibrational modes (797, 1010, 1077, 1210, 1377, and 1620 cm^{-1}) that correspond to the plasmon-generated product.

Unfortunately, we are unable to comment on the overall efficiencies or yields of this particular chemical reaction. In order to induce the growth of the new vibrational modes, the substrate had to be displaced from the laser's focal position. When we positioned the AuFON within the incident light's focal point, we only observed Raman peaks that corresponded to NMP. However, when we discretely translated the substrate away from the laser's focal point, the photoproduct's peaks would begin to grow in on the spectrum. This experimental limitation restricted us from accurately measuring any changes in the observed NMP molecules, as our collections did not accurately depict the original number of NMP molecules positioned in the probed area.

In order to understand more about this chemical transformation, we investigated the reaction's dependence on the applied flux of the 785 nm excitation. We studied the plasmon-mediated reaction with fluxes of 5,000, 12,500, and 31,500 W/cm^2. A description of our procedure to measure the laser spot size and subsequent flux calculations can be found in Appendix B. Lowering the flux resulted in a reduced signal-to-noise ratio, which was accounted for by increasing the acquisition time for each collected frame. The acquisition times for the 5,000, 12,500, and 31,500 W/cm^2 experiments were 1.0, 0.11, and 0.06 sec, respectively. However, the reduced temporal resolution did not significantly affect the results for the low-flux experiments. We included a zero-point value to the flux-dependent plots due to our observations that the chemical process does not initiate unless the substrate is exposed to resonant excitation.

The error bars in **Figure 4.3** represent the averaged standard deviation of the five trials we performed for each data point. We randomly selected the regions for each trial on a singular AuFON substrate to ensure we were operating a consistent position relative to the laser's focal point. However, we were able to observe the formation of a new photoproduct on multiple AuFON substrates that were fabricated using the directions provided in the Methods. The large error bars for the data points performed with an applied flux of 32,000 W/cm^2 are likely due to the increased photodamage that may occur when the SERS substrates are introduced to high laser fluxes. For example, the two trials with the most intense SER signals resulted in having the slowest rates in the 32,000 W/cm^2

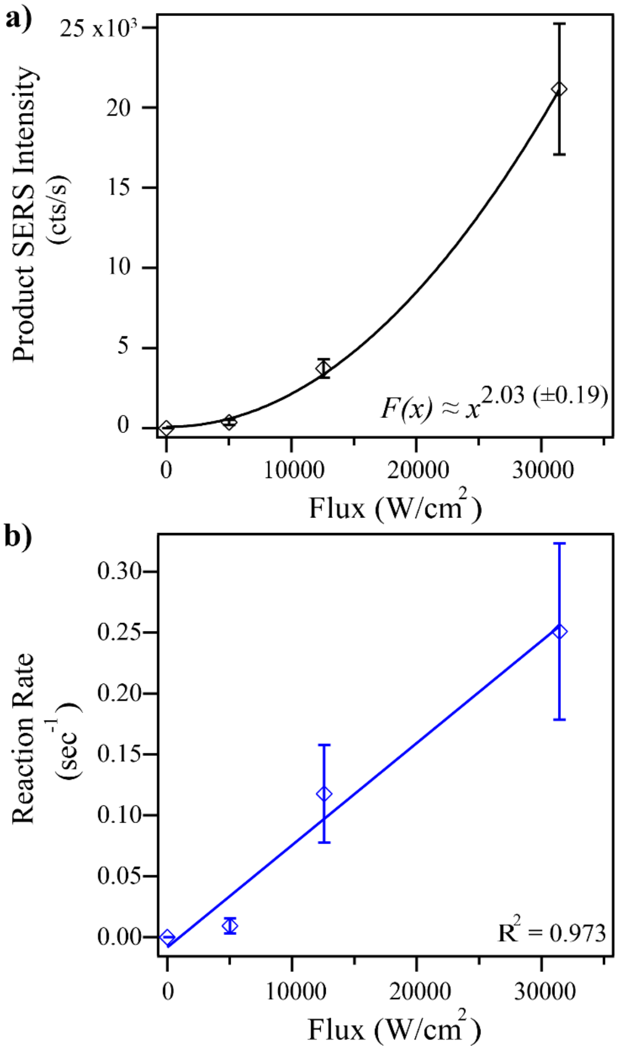

Figure 4.3 Flux-dependent product production and reaction rates. (a) Non-linear relationship between the flux introduced to the SERS substrate and the final product signal intensity. We fit this trend to a power function with the following coefficients: y-intercept, amplitude, and power of 80 (±360), -1.6x10^{-5} (±3.1x10^{-5}), and 2.03 (±0.19), respectively. (b) Relationship between the reaction's rate and the applied flux. This linear fit's slope, y-intercept, and R^2 are 8.38 x 10^{-6} (±0.98 x 10^{-6}), -8.22 x 10^{-3} (±1.69 x 10^{-2}), and 0.973, respectively.

studies. As the applied flux is increased, the local fields are further amplified and the likelihood of inducing competing destructive mechanisms on the gold surface significantly increases.[20] The intense electromagnetic fields are capable of physically changing the identity of the analyte and, at times, provide sufficient energy to induce dielectric breakdown for certain molecules.[234] In addition to the chemical responses, the gold lattice may experience atomic-level alterations when subjected to an intense laser source, which would dramatically modify the structural integrity of the SERS substrate and induce significant changes to the inhomogeneous electric fields located near the surface.[199] Therefore, the addition of these competing degradation pathways, both at the molecule and substrate level, will likely lead to a wider distribution of reaction rates and product generation.

We experimentally observed positive correlations between the product's intensity (normalized with respect to acquisition time) and reaction's rate against the applied flux onto the sample. The first correlation relates to the overall increase in the product's intensity as the flux is increased (**Figure 4.3a**). Here, we monitored the growth of the product species' 1077 cm^{-1} vibrational mode and fit the resulting kinetic trace to an exponential function. By increasing the flux directly applied to the substrate, we noted that the product intensities were able to reach a larger final amplitude as the reaction approached completion, which was an unexpected observation. Typically, we would expect the SER signal to have a linear relationship with the flux. However, after fitting the data to a power function, we observed a $x^{2.03\ (\pm 0.19)}$ dependence between the intensity and flux. While we are unable to determine the exact cause of this observation, we postulate that this phenomenon is linked to the following two physical explanations. First, a larger flux increases the effective surface area that is exposed to the incident laser light. This would ultimately result in more hot spots on the surface being photoactivated and provide more molecules to undergo the reaction. Secondly, the elevated flux would result in an increased number of hot carriers generated in the plasmonic material. It is possible that the NMP plasmon-mediated reaction requires multiple hot carriers, which would explain the flux-dependent growth in the product species.

We were also able to extract the power-dependent reaction rate constant from the exponential fit applied to the 1077 cm^{-1} peak's kinetic traces. Similar to the product formation magnitudes, we observed positive flux-dependent correlation in reaction's rate (**Figure 4.3b**). This flux-dependent trend suggests that we are operating in a regime where the plasmon excitation is the rate-limiting step of the process. By increasing the number of accessible resonant photons, we are able to effectively accelerate the speed for which the reaction proceeds. Also, it is possible that the increased flux is allowing for more molecules within the same region to react and convert into the photoproduct, which would alter the observed reaction rate. While this result is instrumental in identifying plasmon excitation as the rate-limiting step of this specific process, we are unable to determine a step-by-step mechanistic description of the reaction.

With the reaction's production and rate evaluated, we performed experimental and theoretical studies to determine the identity of this selective plasmon-mediated reaction. To do so, we extracted a SER spectrum corresponding to the plasmon-mediated photoproduct after the reaction reached completion. This was done by subtracting away the initial NMP SER spectrum from the final frames of the exposure. With this product-only SER spectrum, we are able to spectrally compare the photoproduct against the SER spectra of known chemical species. We studied three possible photoproducts that may be generated during the plasmon-mediated reaction: pyridine, 2-methlypyridine, and 4-methylpyridine. Previous work has successfully demonstrated a plasmon-driven N-dealkylation on amine containing species,[225] which would result in the formation of pyridine in our NMP studies. Additionally, there is precedent in the literature for NMP to serve as an oxidizing agent and stabilize a radical in its ring[235-236] and to lead to the generation of 2-methylpyrdidine and 4-methylpyrdiine under certain experimental conditions.[237-238]

We collected the possible photoproducts' SER spectra on AuFON substrates and also calculated their corresponding SER spectra using the dressed-polarizability model[183, 227-228] that accounts for the inhomogeneous electric fields present on the SERS substrates. The dressed-polarizability model uses polarizability tensors calculated with quantum mechanics to describe the molecules and local field enhancement matrices calculated with classical electrodynamics. These calculations can therefore uniquely account for the selective enhancements of specific vibrational modes due to the interaction of the molecule with the (inhomogeneous) local fields from the plasmonic surface, critical for obtaining reasonable agreement with surface-enhanced vibrational spectra. The experimental SER spectra of these three molecules, their respective calculated SER spectra, and NMP photoproduct's spectrum can be seen in **Figure 4.4**.

The grey bars in **Figure 4.4** highlight the spectral regions where we expect to see overlap between the photoproduct's Raman vibrational modes and the modes of its true chemical identity. We observed that both of pyridine's experimental and calculated SER spectra lack a number of the relevant vibrational modes and contains Raman vibrational modes that are significantly shifted outside of the targeted spectral windows. Specifically, pyridine is lacking the 797 (C-CH_3 stretching + i.p. ring deformation), 1077 (ring C-H bending), 1210 (ring C-H bending + C-CH_3 stretching), 1377 (CH_3 umbrella motion), and 1620 (ring stretching) cm^{-1} modes.[239] 2-methylpyridine's SER spectra had a stronger resemblance to the photoproduct's spectrum than pyridine but contained additional peaks in the 1200-1500 cm^{-1} region that are not present in the product's spectrum

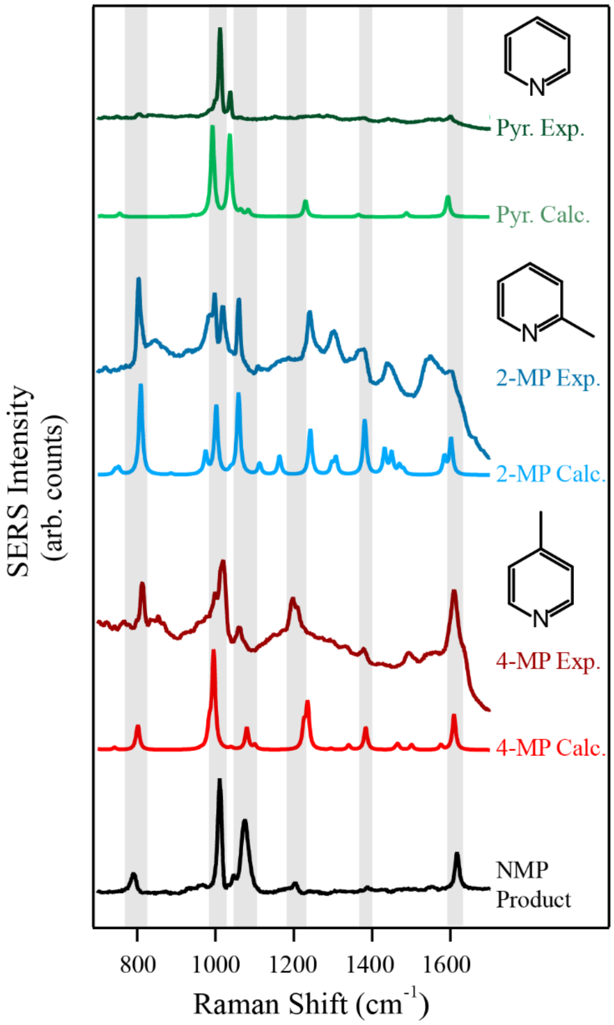

Figure 4.4 Identification of the plasmon-mediated photoproduct. Experimental (dark) and calculated (light) SER spectra of pyridine (green), 2-methylpyridine (blue), and 4-methylpyridine (red) compared against the NMP plasmon-mediated photoproduct (black). The grey bars highlight the regions where we expect to see spectral overlap between the NMP product and its true chemical identity.

and lacked strong overlap with the 1010 (i.p. ring deformation) and 1210 cm^{-1} modes found in the NMP photoproduct. With these observations, we concluded that both pyridine and 2-methylpyridine were not the chemical species being produced in this plasmon-mediated process due to the lack of agreement between their respective spectra.

However, when we compared 4-methylpyridine's experimental and calculated SER spectra to the photoproduct's spectrum, we found that the spectra belonging to the two molecular species were in strong agreement. Both of 4-methylpyridine's spectra contain all of the relevant vibrational modes that are present in the photoproduct's spectrum. Both of the spectra contain and have a strong overlap at the 797, 1010, 1077, 1210, 1377, and 1620 cm^{-1} peaks. We recognize that there are discrepancies in the relative amplitudes of the peaks within the spectra, such as the 1077 and 1210 cm^{-1} modes, but these variations may be due to the differences in binding configurations of a drop-casted solution of 4-methylpyridine and the plasmon-mediated photoproduct. Unfortunately, accurately predicting the orientation and binding configuration of the photogenerated 4-methylpyridine molecules is a non-trivial challenge.

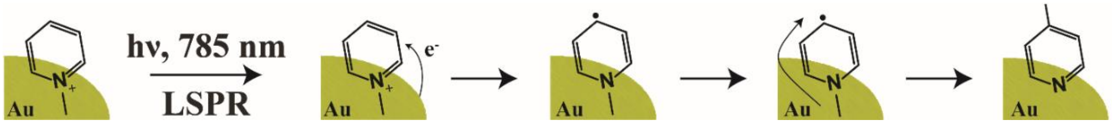

Figure 4.5 Proposed mechanism for plasmon-mediated methyl shift of N-methylpyridine to 4-methylpyridine. The substrate is photoexcited by a resonant 785 nm laser source and subsequently transfers a hot electron to the chemisorbed NMP species. This gives rise to a transient pyridinyl radical species. The N-substituted methyl group then shifts to the radical and stabilizes as 4-methylpyridine.

Figure 4.5 shows our proposed mechanism behind the plasmon-mediated reaction of NMP to 4-methylpyridine. During the exposure, we observed the production and stabilization of Raman features corresponding to 4-methylpyridine. We believe that once the AuFON substrate is exposed to a resonant laser source, the surface plasmon is excited and partitions its energy into the generation of hot electrons and holes. These hot electrons are harvestable, and the local field conditions help promote the transfer of an electron to the NMP species. Previous reports have investigated NMP's ability to serve as an electron accepting material.[236] To the best of our knowledge, there are no reports of NMP or other comparable pyridinium molecules acting as electron donating species, which suggest that the prevailing mechanism fueling this reaction is an electron transfer event. This electron transfer is a transient process and leads to the formation of a short-lived pyridinyl radical species on the substrate's surface. The transfer of a hot electron to an adsorbed analyte occurs in a femto-to-picosecond timescale and we are not able to directly observe this event in our SER spectra.[145]

After the pyridinyl species is formed, we hypothesize that the N-bound methyl group is to preferentially migrate to the C_4 on the heterocyclic amine, producing 4-methylpyridine as the final product. We do not observe the formation of any 2-methylpyridine byproducts in these experiments. We postulate that this is due to a steric hindrance provided by the 2-methyl group on the ring. The NMP molecules are positioned in a tight-packed layer on the surface and would experience an unfavorable steric hindrance if the methyl group were to transfer to the C_2 position. In contrast, mediating a direct methyl migration to the C_4 on the heterocyclic ring would not invoke any steric effects on the molecule, resulting in a more favorable product in the reaction. To further support our hypothesis, a previous study determined that when introduced in a competitive manner, 4-methylpyridine will adsorb more favorably to metal surfaces than 2-methylpyridine.[240] The authors found that there was a distinct and clear steric effect in play for the adsorption of 2-methylpyrdine on the metal surface, whereas 4-methylpyridine did not express any similar effects. To that end, our findings, in addition to the precedent found in literature,[237-238] support our educated hypothesis that NMP is undergoing an intramolecular methyl migration to form 4-methylpyridine.

4.5 Conclusions

Our observation of the intramolecular methyl migration on NMP highlights a new example of enabling selective chemistry in plasmonic environments. In this work, we used AuFON substrates to simultaneously induce and record the plasmon-mediated transformation of NMP an unreported photoproduct. The plasmon-mediated reaction demonstrated a clear positive correlation between the applied flux and the reaction's overall production and rate. We were able to successfully assign 4-methylpyridine as the NMP photoproduct's true chemical identity by collecting experimental and theoretical spectra of possible photoproducts. This work highlights the growing potential of implementing plasmonic platforms to preferentially drive selective chemistries, as well as adding another addition to the repository of accessible plasmon-mediated chemical reactions.

4.6 Acknowledgements

We acknowledge the support from the Air Force Office of Scientific Research under AFOSR award no. FA9550-15-1-0022. Portions of this work were conducted in the Minnesota Nano Center, which is supported by the National Science Foundation through the National Nano Coordinated Infrastructure Network (NNCI) under Award Number ECCS-1542202. We would also like to thank the Haynes Lab at the University of Minnesota for allowing us to use their thermal evaporation deposition chamber for fabricating the AuFON substrates. This research used resources of the National Energy Research Scientific Computing Center (NERSC), a U.S. Department of Energy Office of Science User Facility operated under Contract No. DE-AC02-05CH11231. Additional computer resources were provided by the Minnesota SupercomputingInstitute (MSI) at the University of Minnesota.

Chapter 5

Plasmon-Driven C-N Bond Cleavage Across a Series of Viologen Derivatives

Reprinted with permission from manuscript by James L. Brooks, Dhabih V. Chulhai, Jason D. Goodpaster, and Renee R. Frontiera. To be published.

5.1 Overview

The optical excitation of surface plasmons leads to the generation of highly-enhanced nanoscale local fields and an abundance of harvestable hot carriers. When certain analytes are positioned within these unique environments, surface plasmons may be able to induce chemical reactions that are energetically unfavorable under standard conditions. Sometimes the plasmonic environments can initiate entirely new reaction pathways for the chemical adsorbates. Here, we investigate the nature of plasmon-driven reactions on three viologen derivatives: methyl viologen, ethyl viologen, and benzyl viologen. Viologens have traditionally been employed as excellent redox agents due to their ability to reversibly stabilize additional electrons in their molecular structures. However, by using surface-enhanced Raman spectroscopy, we were able to directly observe a C-N bond cleavage on benzyl and ethyl viologen to form 4,4'-bipyridine on the surface of gold film-over-nanosphere substrates. Surprisingly, methyl viologen does not undergo a similar process. We posit that this differing reactivity may be due to changes in adsorption geometry or in reduction potential. Using both spectroscopic and theoretical methods, we were able to confirm 4,4'-bipyridine as the plasmon-mediated photoproduct. This work highlights the novelty of using plasmonic environments to access new chemical reactions and adds to the expanding library of plasmon-mediated chemical reactions.

5.2 Introduction

Nanostructured plasmonic materials host enhanced optical properties that allow for the confinement and amplification of an incident electromagnetic wave in the near field.[44,

[66] This phenomenon is powered by the presence of a surface plasmon, which is the collective oscillation of the material's conduction electrons. In addition to the local light amplification, the excitation and subsequent decay of a surface plasmon may lead to the generation of highly-energetic electrons and holes, enhancement thermal environments, and the modification of a chemical adsorbate's potential energy surface.[9, 38] These unique forms of energy pathways may be harvested and directed toward initiating chemical reactions.[39, 212-214] Recently, the field of plasmonics has been aggressively investigating the potential of using plasmonic materials as light-activated photocatalysts. Plasmonic materials have been successful in accessing catalytic reactions such as, but not limited to, H_2 dissociation,[35] acid dehydrogenation,[36] CO_2 reduction,[47] acetylene hydrogenation,[14] NH_3 generation[27] and decomposition,[15] and H_2O splitting.[10]

Surface-enhanced Raman spectroscopy (SERS) is an excellent surface-specific spectroscopic technique that can be used to explore the interactions between adsorbed chemical species and plasmonic catalysts.[17, 90, 241] The technique takes advantage of the plasmonic nano-confinement of an incident electromagnetic wave by amplifying the Raman signal from molecules positioned in the dramatically-enhanced local fields, which are also referred to as hot spots. In fact, the resulting SER scattering is approximately proportional to the local electric field to the fourth power, $|E/E_0|^4$. It has been experimentally proven that a significant majority of the collected SERS intensity is produced by the molecules positioned in the most intense hot spots,[92] which are also the most reactive regions of the substrate.[21] Ultimately, SERS is highly effective in determining chemical structures and any subsequent changes in bonding in the most powerful regions of enhancement on the substrate, making it an excellent tool to probe the mechanism of plasmon-driven reactions.

Previous reports have been successful in identifying the products of plasmon-mediated chemical reactions with SERS. Most of these publications investigate the well-studied dimerization reaction of 4-nitrobenzenethiol or 4-aminothiolphenol to 4,4'-dimercaptoazobenzene.[20, 103, 107, 118] This reaction has been studied extensively with multiple plasmonic substrates to better understand the underlying plasmonically-powered mechanism. Other reports have been predominantly restricted to exploring plasmon-mediated cleavages of certain atoms or functional groups on studied analytes. For example, there have been demonstrations of inducing a N-methyl cleavage on methylene blue.[225, 242] As an additional expansion into the library of SERS monitored plasmon-mediated reactions, here we report the first observation of a C-N bond cleavage on a series of viologen derivatives.

Viologens have traditionally been employed as redox molecules to better understand the local electronic environments in numerous biological and materials systems.[243-246] These derivatives have three distinct oxidation states: the dication, radical cation, and the fully reduced species. The dication state is the most energetically favorable state when in solution. The one electron redox potentials ($[V^{2+}/V^{+\bullet}]$) for methyl (MV), ethyl (EV), and benzyl viologen (BV) are -0.446, -0.449, and -0.359 V, respectively.[243, 247] In fact, there have been reports of using SERS to track the one and two electron reductions of MV on a gold plasmonic system.[19, 248-249] However, contrary to previous reports, we observed that when these viologen derivatives are introduced to the dramatically-enhanced local fields provided by gold film-over-nanosphere (AuFON) substrates, they are able to access an alternative reaction pathway to form a new chemical species.

In this study, we discuss the direct observation of C-N bond cleavage on BV and EV chemisorbed to the surface of AuFON substrates. This plasmon-mediated reaction involves the double cleavage of the benzyl and ethyl groups on both molecular analytes. We were able to successfully induce the plasmon-driven process on AuFON substrates using a 785 nm excitation source and monitored the reaction using SERS. Additionally, we observed that the MV photoreaction undergoes an entirely different reaction pathway and does not produce 4,4'-bipyrdine. With the collected spectra, we were able to quantitatively track the production of the plasmon-mediated photoproduct. To confirm our chemical assignment, we performed both experimental and computational SER studies of 4,4'-bipyridine on plasmonic substrates. Ultimately, this work emphasizes the novelty of using dramatically enhanced plasmonic fields and their ability to alter and/or access new reaction pathways for specific chemical adsorbates.

5.3 Methods

5.3.1 AuFON Substrate Fabrication

We prepared the plasmonic AuFON substrates by following previously published procedures.[201, 250] First, we oxygen plasma etched glass coverslips (Fisherbrand, 18 mm diameter, 0.13-0.17 thick) to treat the surface for nanosphere deposition. We rinsed the glass coverslips thoroughly with deionized water both before and after the plasma etching. We exchanged the solvent of 600 nm diameter silica microspheres (NanoCym, 10% by volume) with Millipore ultrapure H_2O (18 MΩ). We drop-cast and manually dispersed 3 μL of the silica solution across the surface of the glass coverslip. The water evaporated at ambient conditions, driving the spheres to pack into a monolayer. Following formation of a hexagonal lattice of silica microspheres, we deposited 200 nm of gold on the substrates using a thermal evaporation system (Denton Vacuum, DV-502). We set the instrument to rotate the substrates at 16 rpm during the deposition process. We prepared 350 μM solutions of benzyl viologen dichloride (Sigma Aldrich, 97% purity), ethyl viologen dibromide (Sigma Aldrich, 99% purity), and methyl viologen dichloride hydrate (Sigma Aldrich, 98% purity) in methanol and deposited 10 μL of solution on each AuFON for our SERS measurements.

We measured the localized surface plasmon resonance (LSPR) extinction spectrum with a UV-2600/2700 equipped with an integrating sphere attachment (Shimadzu). The data acquisition time for each collection was 4 milliseconds.

5.3.2 Raman Spectroscopy

We collected the Raman spectra by using a 785 nm Innovative Photonic Solutions diode laser. We directed the laser beam through a 30/70 beam splitter (CVI Laser) and focused to a 15.9 μm^2 spot onto the substrate with an objective (Olympus Ach 10x/0.25). We performed the collection in a 180° backscatter geometry and redirected the scattered radiation through the beam splitter and towards the detection system, which consisted of a spectrograph (Acton SpectraPro 2500i) with a CCD detector (Princeton Instruments, PIXIS 100BX). Our spectral acquisition times ranged from 66 ms – 1 sec, depending on the designated power used during the experiment. We normalized the Raman intensities with respect to the acquisition time and excitation power in order to provide a consistent and quantitative comparison.

5.3.3 Theoretical Calculations

We carried out all calculations using version 2018 of the Amsterdam Density Function (ADF) suite,[229-230] the Becke-Perdew (BP86) exchange-correlation potential,[231-232] and a triple-zeta Slater type basis set with two polarization functions (TZ2P) from the ADF basis set library; these parameters closely reproduced the experimental vibrational frequencies for the small molecules.[251] We calculated the normal modes analytically within the harmonic approximation and scaled the BP86 frequencies by a factor of 1.017 to account for anharmonic effects.[252] We used the dressed-polarizability model[183, 227-228, 231-232, 253] to simulate all SERS spectra using both electric fields and field gradients. We obtained local electric fields and field gradients from a model sphere to mimic surface roughness features ~3 nm. Lastly, we calculated the Gibbs free energy changes (ΔG) at 298.15 K, where the solution environment was accounted for by using the conductor-like screening model (COSMO).[254-255]

5.4 Results and Discussion

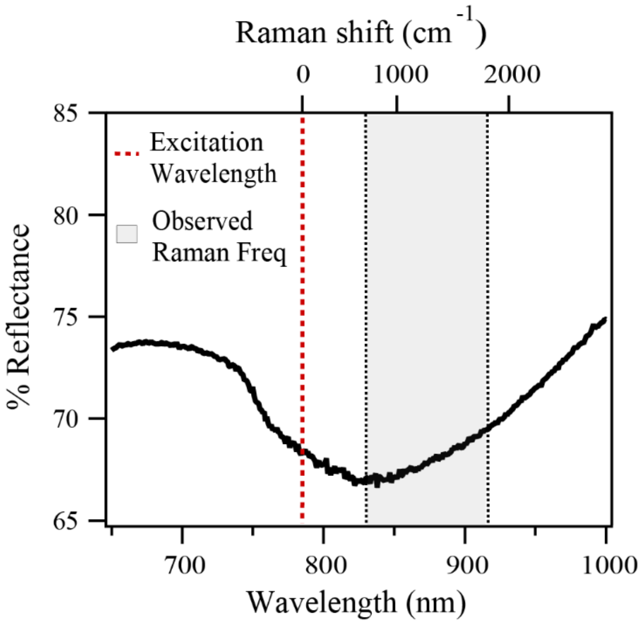

Figure 5.1 UV-Vis-NIR reflectance spectrum of AuFON substrates. The broad, negative feature between ~750-1000 nm corresponds to the presence of a localized surface plasmon resonance. The SERS measurements were performed with a 785 nm excitation source (dashed line, red) and the collected Raman-modes (highlighted region, blue) were scattered between ~840 to ~900 nm.

We performed UV-Vis-NIR spectroscopy to provide a quantitative measurement of the substrate's plasmonic properties. **Figure 5.1** displays the percent reflectance spectrum from the AuFON SERS substrates that we used during these experiments. This spectroscopic measurement accounts for the incident photons that are both absorbed and scattered by the substrate, resulting in an overall decrease in reflectivity due to the localized surface plasmon resonance (LSPR). Therefore, the broad negative feature starting at ~750 nm and extending beyond 1000 nm corresponds to the substrate's LSPR. For SERS measurements, a good estimate is that the optimal signal enhancement occurs when the plasmon is centralized between the excitation wavelength and the scattered photons' wavelengths.[63] We fabricated these AuFON substrates to have their LSPR's λ_{max} to be spectrally positioned at ~840 nm to optimally enhance the SER signal generated from our 785 nm excitation source, which produced Raman-scattered photons ranging from ~840 to ~900 nm. The UV-Vis-NIR measurement is performed over a large, heterogeneous area of the AuFON SERS substrate, making the extinction spectrum an ensemble-averaged collection. Therefore, the resulting spectrum is generated from an assortment of the molecules positioned in the most intense hot spots in the sampled region.

We collected the SER spectra for three different viologen derivatives chemisorbed to the surface of an AuFON substrate: benzyl viologen (BV), ethyl viologen (EV), and methyl viologen (MV). All three molecules are in their dicationic state when adsorbed to the gold substrate, and this is confirmed by previous SERS measurements on viologen species.[248-249, 256-257] **Figure 5.2** displays the time-dependent SER spectra of BV, EV, and MV as they undergo a spectral evolution when a 785 nm excitation source is introduced to the plasmonic substrate. Each plot shows the growth of a previously unreported irreversible product species. When benzyl viologen is chemisorbed to the surface of an AuFON substrate, we observed the growth of six new vibrational modes (**Figure 5.2a**). These modes, highlighted with grey bars in plot, are spectrally positioned at 1020, 1070, 1224, 1294, 1512, and 1608 cm^{-1}. The initial SER spectra (dark red, 220 ms) contain the Raman-active vibrational features that correspond to chemisorbed benzyl viologen molecules. We did not observe any transient intermediate species during the measurements. Likewise, a similar production of a plasmon-mediated photoproduct occurred when we deposited and studied EV on the SERS substrate; we observed the formation of the same six Raman-active modes (**Figure 5.2b**). However, the production of the EV photoproduct only occurred when the substrate was exposed to intense laser fluxes (260 kW/cm^2).

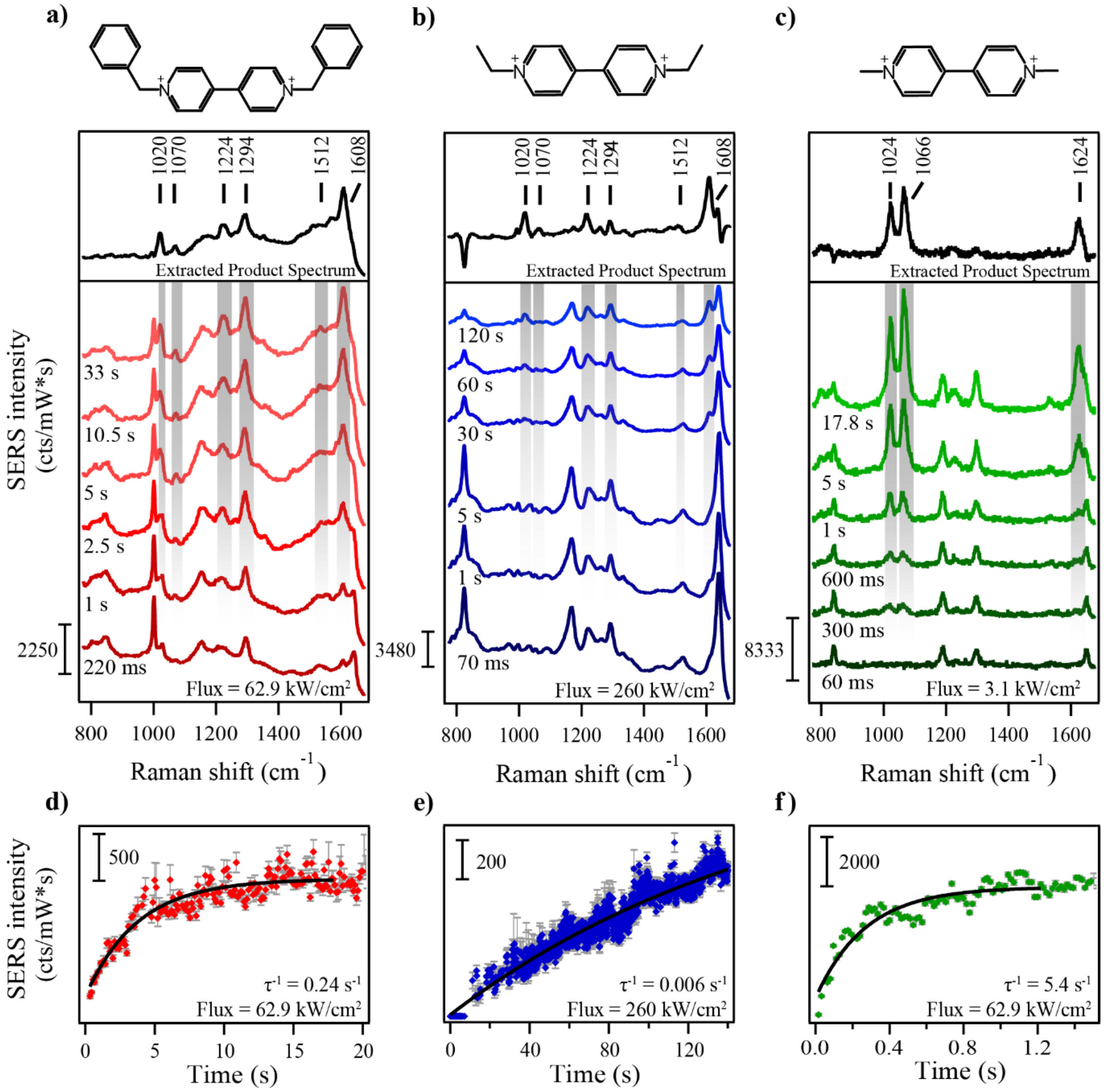

Figure 5.2 Plasmon-mediated chemical transformation of viologen derivatives. Time-dependent SER spectra of (a) benzyl viologen (BV), (b) ethyl viologen (EV), and (c) methyl viologen (MV). The new Raman modes corresponding to the plasmon-driven photo product for BV and EV are found at 1020, 1070, 1224, 1294, 1512, and 1608 cm^{-1} (grey highlight). However, MV does not appear to produce the same Raman features and has new modes appear and grow in at 1024, 1066, and 1624 cm^{-1}. Kinetic traces of the product growth for (d) BV's 1608 cm^{-1}, (e) EV's 1608 cm^{-1}, and (f) MV's 1024 cm^{-1} vibrational modes.

In addition to BV and EV, we collected the time-dependent SER spectra of MV (**Figure 5.2c**). We initiated this experiment with a flux of 3.1 kW/cm^2 to delay the rapid growth of the product species, which allowed us to extract a neat product spectrum. Interestingly, the time-dependent SER spectra contained new Raman features that do not match the photoproduct formed in the BV and EV studies. Rather, we observed the production of three distinct Raman modes at 1024, 1066, and 1624 cm^{-1}. These three modes are dramatically more intense than the product peaks formed during the BV and EV exposures.

With each time-dependent SERS measurement, we were able to calculate an associated rate constant from the kinetic traces. **Figure 5.2d-f** displays the corresponding kinetic traces for BV, EV, and MV when exposed to laser fluxes of 62.9, 260, 62.9 kW/cm^2, respectively. While BV and EV's time-dependent SER spectra show that they are producing the same photoproduct, their observed reaction rates are substantially different. Specifically, the average rate constant for the BV experiments was 0.24 s^{-1} and the associated rate constant for the EV trail was two orders of magnitude slower while being initiated with a dramatically more intense laser flux (0.006 s^{-1}, 260 kW/cm^2). Additionally, we observed that the MV photochemical reaction, which produced a different spectrum than the BV and EV reactions, clearly had the fastest product production with a 5.4 s^{-1} rate constant. We have provided a more detailed discussion on the flux-dependent reaction rates for BV later in the Results and Discussion.

Traditionally, these viologen derivatives have been used as oxidation/reduction indicators in a wide-range of biological studies. As stated in the Introduction, most viologen derivatives possess some of the lowest redox potentials of organic species while maintaining a high-level of reversibility. The viologen derivatives can access three different oxidation states, which are the dication, radical cation, and the fully reduced species. All three of the viologen derivatives we studied are naturally stabilized in their dication form, with both of the nitrogen atoms being positively charged. The reported one electron redox potentials ($[V^{2+}/V^{+\bullet}]$) for MV, EV, and BV are -0.446, -0.449, and -0.359 V, respectively.[243, 247] However, we did not observe the formation of any short-lived Raman features that correspond to the radical cation or fully reduced state that have been reported in previous publications.[248-249, 257]

Previous SERS studies have been performed on similar large heterocyclic amines that contain N-bound substituents. Specifically, we directed our attention to a pair of publications by Tesema *et al*.[225, 242] In their work, the authors found that they were able to utilize plasmonic environments to initiate N-methyl cleavage on methylene blue to form thionine. Similarly, the viologen derivatives that we are probing in these experiments contain N-bound substituent groups in their molecular structure; BV and EV contain benzyl and ethyl substituents, respectively. If the viologen species are behaving in the same manner as the plasmon-enhanced N-methyl cleavage of methylene blue, we would expect to see a cleavage of both of the viologen derivatives' C-N bonds and form 4,4'-bipyridine (BPY).

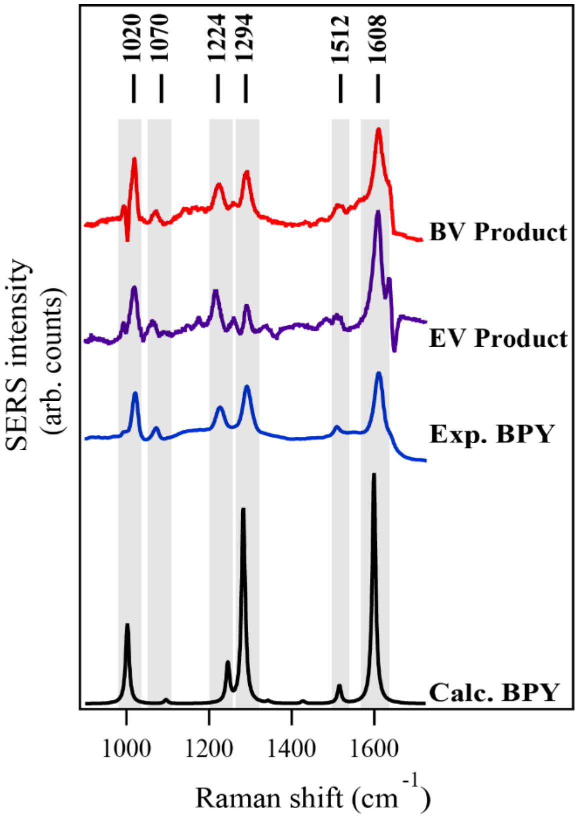

Figure 5.3. Comparison of the experimental and theoretical SER spectra of the viologen photoproducts and BPY. The BV (red) and EV (purple) photoproduct's spectra are in strong agreement with the experimental (blue) and theoretical (black) spectra of BPY. We observed an overlap of the 1020, 1070, 1224, 1294, 1512, and 1608 cm^{-1} vibrational modes in all four spectra, confirming the assignment.

To test our hypothesis that BV and EV were undergoing a plasmon-mediated cleavage of their C-N bonds, we collected both theoretical and experimental SER spectra of BPY. **Figure 5.3** displays the SER spectra of the BV and EV photoproducts compared against the experimental and theoretical spectra belonging to BPY. We were able to extract the products' spectra by subtracting the initial spectra, belonging to chemisorbed BV and EV, from the final spectra collected during the exposures. As seen in **Figure 5.3**, the product spectra are in strong agreement with the experimental BPY SER spectrum. The 1020 (ring breathing), 1070 (ring in plane deformation + CH bending), 1224 (CH in plane bending), 1294 (inter-ring stretching), 1512 (CH in plane bending + ring stretching), and 1608 (ring stretching) cm^{-1} Raman-active modes corresponding to BPY are present in the BV and EV photoproduct's SER spectra.[258] Additionally, the calculated theoretical SER spectrum of BPY on a gold surface is in strong agreement with the extract spectra from the BV and EV photoproducts. Unfortunately, we have been unsuccessful in accurately determining the chemical identity of the new species produced during the MV studies. In an attempt to determine the identity of the MV photoproduct, we spectrally compared the MV photoproduct and an assortment of possible logical photoproducts. Additionally, we also performed a similar SERS measurement on a fully deuterated analog of MV. A discussion on our additional MV studies can be found in Appendix C. Yet, in regard to the BV and EV spectral comparison studies, both spectroscopic methods were highly beneficial in confirming our hypothesis that BV and EV undergo a plasmon-mediated N-benzyl and N-ethyl cleavage to form BPY, respectively.

With the photoproduct's true identity assigned, we were able to determine the relationship between the plasmon-mediated reaction and the flux used to initiate the chemical process. More specifically, we were able to determine the flux's influence on the product's overall production and rate. We initiated the BV photoreaction with fluxes of 5.0, 12.5, 31.5, and 62.9 kW/cm^2 and the acquisition times for each flux measurement were 1 s, 51, 51, and 111 ms, respectively. We have provided a description of our methods used to determine the laser spot size and the associated flux calculations in the Appendix C. Unfortunately, we were unable to perform similar power-dependent experiments on EV, as we were only able to induce the reaction under a flux of 260 kW/cm^{-1}, which resulted in significant molecular and substrate degradation throughout the exposures.

During these measurements, the lower applied fluxes produced time-dependent SER spectra with reduced temporal resolutions. This was due to the necessity to increase the exposure time to ensure we were collecting spectra with acceptable signal-to-noise ratios. Fortunately, the reduced temporal resolution did not affect our experiments because the reaction's rate was significantly slower when initiated with less intense fluxes. We included a zero-point flux value to the plots in **Figure 5.4** because the reaction does not proceed unless an external photon source is introduced to the AuFON substrate. The error bars presented in **Figure 5.4** represent the averaged standard deviation of the five trials we performed at each

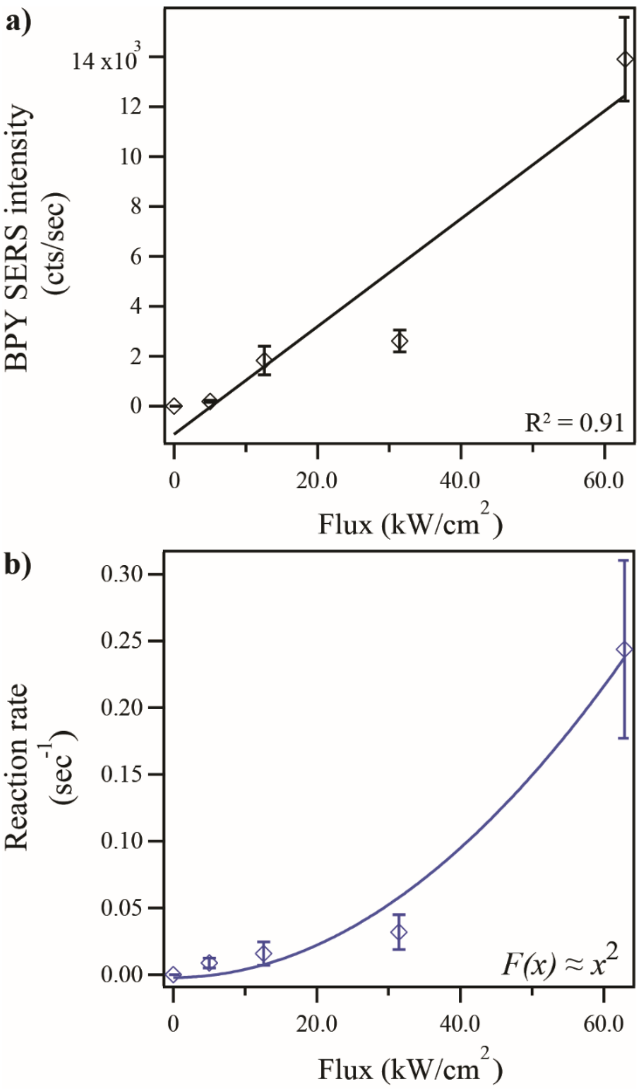

Figure 5.4. Flux-dependent product production and reaction rate for BV. (a) Positive correlation between the applied flux and the product SERS intensity (normalized in respect to the acquisition time). Here, we fit the flux-dependent product intensities to a linear trendline. The linear fit's slope, y-intercept, and R^2 are 0.22 (±0.04), -1130 (±1290), and 0.91, respectively. (b) The reaction's rate and its relationship with the flux. We fit this trend to a 2nd-order power function with the following coefficients: y-intercept, amplitude, and power of -0.002 (±0.009), $6.9\text{x}10^{-11}$ ($\pm 5.1\text{x}10^{-12}$), and 2, respectively.

flux. In these experiments, we randomly selected the locations for each trial across two different AuFON substrates.

Figure 5.4a displays the positive correlation between the Raman intensity of the plasmon-generated BPY and the applied flux onto the AuFON substrate. We monitored the growth of the BPY species' 1608 cm^{-1} vibrational mode and fit the resulting kinetics to an exponential function. As the applied flux was increased, we observed that BPY's 1608 cm^{-1} mode was able to reach more intense amplitudes once the reaction reached a point of completion. We postulate that this result may be due to two different physical explanations. The first reasoning is linked to the flux-dependent production of plasmonic hot carriers. The elevated flux on the AuFON substrate would result in an increased generation of hot carriers on the plasmonic material. If this reaction is a hot electron-driven process, we would expect to see an increase in the production when more hot electrons are accessible by the adsorbates. In addition to the increased generation of hot carriers, it is possible that the observed positive correlation between the flux and product's intensity is associated to an increased effective surface area that is exposed to the resonant photons. This would result in the photoexcitation of additional hot spots, and subsequently molecular adsorbates, on the surface and ultimately increase the number of viologens that may undergo the plasmon-mediated chemical transformation.

In addition to the flux-dependent product production, we investigated the relationship between the reaction's rate and the applied laser flux. We extracted this value from the exponential fit that we applied to the 1608 cm^{-1} kinetic traces. As with the production study, we observed a clear positive correlation between the two variables.

However, in this case, we were able to successfully fit the flux-dependent reaction rates to a second-order power function, x^2. The strong agreement between the flux-dependent rate and the 2nd order power function is due to the two individual C-N bond cleavages that must occur on BV to form BPY.

This is the first report of a light-activated or plasmon-mediated C-N bond cleavage on BV and EV. We believe that the dramatically-enhanced local electromagnetic fields on the AuFON plasmonic substrates provide an essential amount of energy to create entirely new reaction pathways for the viologen derivatives. Previous electrochemical and spectrochemical studies on these viologen derivatives did not observe the formation of BPY when large voltages were applied to the electrochemical cells. Rather, they were able to reversibly induce electron transfer to the viologen derivatives to form the radical cation and fully reduced species. In our experiments, the unique and strongly amplified plasmonic local fields did not allow for a stabilized or observable reduction of the viologen derivatives and directly promoted the C-N bond cleavage to form BPY.

Similar to the mechanism presented by Tesema *et al.*, we postulate that the C-N bond cleavage on the viologen derivatives relies on the presence of oxygen in the local environment.[225] Here, we propose that a transient anionic oxygen species is created by the hot electron generation that occurs when the surface plasmon is photoexcited.[259-260] Their work highlighted the concept that an anionic oxygen interaction with the nitrogens and a hydrogen extraction from the local water molecules is the likely mechanism driving the cleavage of the C-N bond on these large heterocyclic amines. Ultimately, it is very likely that the BV and EV plasmon-mediated transformations on AuFON substrates are occurring by the same chemical mechanism.

In order to explain the increased reactivity of BV relative to EV, we calculated the change in Gibbs free energy (ΔG) associated to the double cleavage on BV, EV, and MV to form BPY. The solution phase ΔG's for BV, EV, and MV are -0.4, 4.6, and 8.1 kcal/mol, respectively. In our work, we observed that the formation of BPY from BV occurred at a much faster rate and higher production (BV >> EV), which aligns well with our calculations, as BV's ΔG is lower than that for EV. From Hammond's postulate,[261] we would expect the reaction rates for BV to BPY to be higher than that for EV to BPY based on the calculated ΔGs. These calculations may provide additional insight in understanding the relative amount of energy required to initiate the C-N bond cleavage on the viologen derivatives. Additionally, the relatively large ΔG for the MV reaction indicate that N-methyl cleavage on MV may be too energetically unfavorable to initiate. We hypothesize that a competing plasmon-mediated reaction pathway may be more energetically accessible and prevents MV from undergoing N-methyl cleavage.

5.5 Conclusions

In this work, we have introduced a new plasmon-driven reaction across a series of viologen derivatives. Specifically, we presented the first report of a plasmon-mediated C-N bond substituent cleavage on benzyl and ethyl viologen to form 4,4'-bipyridine. While these molecules have traditionally been employed as redox agents, we observed an alternative reaction pathway when introduced to the highly-enhanced local fields on

AuFON substrates. To confirm the identity of the plasmon-driven photoproduct, we employed both spectroscopic and computational methods to study 4,4’-biypridine on the surface of gold SERS substrates. Additionally, we presented the formation of the methyl viologen plasmon-mediated photoproduct and our attempts to determine the true chemical identity of the unknown moiety. Our work highlights the novelty of utilizing plasmonic materials as a platform to induce chemical reactions that are unfavorable under standard conditions and serves as another addition to the ever-growing list of plasmon-mediated reactions.

5.6 Acknowledgements

We acknowledge the support from the Air Force Office of Scientific Research under AFOSR award no. FA9550-15-1-0022. Portions of this work were conducted in the Minnesota Nano Center, which is supported by the National Science Foundation through the National Nano Coordinated Infrastructure Network (NNCI) under Award Number ECCS-1542202. We would also like to thank the Haynes Lab at the University of Minnesota for allowing us to use their thermal evaporation deposition chamber for fabricating the AuFON substrates. This research used resources of the National Energy Research Scientific Computing Center (NERSC), a U.S. Department of Energy Office of Science User Facility operated under Contract No. DE-AC02-05CH11231. Additional computer resources were provided by the Minnesota SupercomputingInstitute (MSI) at the University of Minnesota.

Chapter 6

Ultrafast Surface-Enhanced Raman Spectroscopy to Study Hot Electron Transfer in Plasmonic Materials

6.1 Overview

Plasmonic materials are promising platforms for initiating energetically unfavorable chemical reactions. It is widely believed that these reactions are driven by the transfer of highly-energetic hot electrons to the nearby analytes. However, there is still a lack in the general understanding of the interactions between plasmonic hot electrons and molecules, such as the time-dependent reaction rates and the hot electron transfer yield. We propose that these transient electron transfer events, and the following formation of short-lived intermediate species, can be monitored using ultrafast surface-enhanced Raman spectroscopy, a technique that provides a vibrational profile of a molecule near the surface of a plasmonic material. Providing a quantitative description of these interactions will help increase the efficiencies of plasmon-mediated chemical reactions, leading to an optimized design of plasmonically-powered devices capable of enhancing the efficiencies of relevant chemical processes.

6.2 Introduction

Plasmonic materials have recently gained an incredible amount of attention due to their potential to act as light-activated photocatalysts. This is achieved by an effective coupling between an incident light source and the material's surface plasmon,[44, 72] which is the collective oscillation of the free electron charge density on the material's surface. When presented with a source of resonant photons, the surface plasmon is able to rapidly convert that energy and partition it into multiple decay pathways.[9, 45] The surface plasmon is believed to maintain its coherence for 1-10 fs before dephasing and initiating the subsequent processes.[62] While there are multiple decay pathways, the production of highly-energetic hot electrons has been widely found to play the most prominent role in driving plasmon-mediated chemical reactions.[21, 35, 39] Hot electrons are primarily created via Landau damping, through the generation of individual electron-hole pairs and the ensuing electron-electron scattering events over the next 1-100 fs.[71, 73-74] During this time, the ejected hot electrons may have energies extending from the Fermi level to the work function of the plasmonic material.[3, 262]

When certain chemical analytes are positioned near the surface, it is possible that the highly-energetic hot electrons may interact with the molecules and induce a chemical reaction.[19-20, 106, 118] Noteworthy examples of plasmon-mediated chemical reactions include H_2 dissociation,[35] H_2O splitting,[10-11] acetylene hydrogenation,[14] ammonia decomposition,[15] among many others. However, the current work is limited to a description of the plasmonic systems' overall efficiencies, which are poor, and is lacking an understanding of the mechanism by which these plasmonic dynamics occur. To provide further insight into the mechanism and inspire the rational design, a technique with structural sensitivity to probe the various plasmon-molecule interactions is required.

Ultrafast surface-enhanced Raman spectroscopy (SERS) is a technique that provides structural information about a molecular-plasmonic system with time resolution on the order of picoseconds,[7, 21, 140] which is the relevant timescale for the making and breaking of chemical bonds during a hot electron transfer event. Ultrafast SERS uses Raman spectroscopy to take molecular snapshots during the evolution of a plasmon-mediated chemical reaction. Under this experimental design, ultrafast SERS will be instrumental in successfully tracking the ejection of hot electrons from plasmonic materials as they transfer to a specific adsorbed molecule, creating short-lived intermediate species. There is a widespread belief that plasmon-induced chemical reactions are highly contingent on the presence of hot electrons, but the electron transfer process has not been directly observed in a molecular system. By following the step-by-step molecular changes during plasmon excitation, we can identify the specific roles of plasmons and hot electrons in plasmon-mediated chemical reactions. Understanding the various timescales and efficiencies of the hot electron transfer is vital for advancing towards practical and cost-effective industrial applications

Herein, we employ ultrafast SERS to better understand the quantitative information associated to the dynamics, yields, and energies of plasmonic hot electrons. The following chapter details our efforts of designing and interrogating numerous chemical systems aiming for spectroscopically identifying the formation of transient intermediate species during the hot electron process.

6.3 Methods

6.3.1 AuFON Substrate Fabrication and Characterization

We prepared the AuFON substrates by following previously published procedures.[201, 250] First, we oxygen plasma cleaned glass coverslips (Fisherbrand, 18 mm) to treat the surface for nanosphere deposition. We rinsed the coverslips with deionized water before and after the plasma cleaning. We diluted solutions of 600-850 nm diameter silica microspheres (NanoCym) to 10% by volume in Millipore ultrapure H_2O (18 MΩ).

We drop-casted and manually dispersed 3 μL of the silica solution across the surface of the coverslip. The silica microsphere solution evaporated at ambient conditions and the spheres formed into a close-packed monolayer. Following the application of the silica microspheres, we deposited 200 nm of gold on the silica-coated substrates using a thermal evaporation system (Denton Vacuum, DV-502). We set the instrument to rotate the substrates at 16 rpm during the deposition process.

We measured the localized surface plasmon resonance (LSPR) extinction spectrum with a UV-2600/2700 equipped with an integrating sphere attachment (Shimadzu). The data acquisition time for each collection was 4 milliseconds. Percent reflectance measurements of the AuFON substrates can be found in Appendix D.

In addition to the standard AuFON substrates, we fabricated oxide-coated variants of the metal substrates. We coated the AuFON substrate with a dielectric oxide layer using atomic layer deposition. Each deposition recipe was specifically modified to produce the necessary deposition thickness below 5 nm. However, at such miniscule deposition coatings, we were unable to characterize the exact thickness of the oxide layers.

6.3.2. Ultrafast SERS

A detailed description of the ultrafast SERS apparatus has been previously published.[140] For a brief description, we used a Clark-MXR IMPULSE™ to generate the ultrashort pulses used throughout the experiments detailed in this chapter. The IMPULSE™ implements an Yb-doped fiber oscillator/amplifier system to produce a 1035 nm spectrally centered pulse with a < 250 fs duration, a maximum repetition rate of 24.5 MHz, and an average output power of ~15. **Figure 6.1** displays a schematic highlighting the beam paths of the pump and the probe as they navigate the apparatus. We generated the picosecond probe beam by sending the 1035 nm fundamental pulse through a spectral transmission grating filter, which increased the pulse duration to approximately 2.4 ps. Our system allows for using a degenerate configuration (1035 nm pump and probe) or manipulating the spectral character of the pump pulse by sending it though a nonlinear optical parametric amplifier (NOPA). The NOPA produced an output range of ~650 to ~900 nm.

We directed both pulses towards the sample holder and collected the scattered radiation into a spectrograph assembly. The spectrograph assembly consists of a spectrograph (2300i – Princeton Instruments) with a 600 gr/mm grating blazed at 750 nm and a PyLon InGaAs photodiode array (Princeton Instruments). A description of our dual pulse temporal and spatial overlap methods and calculations can be found in Appendix D.

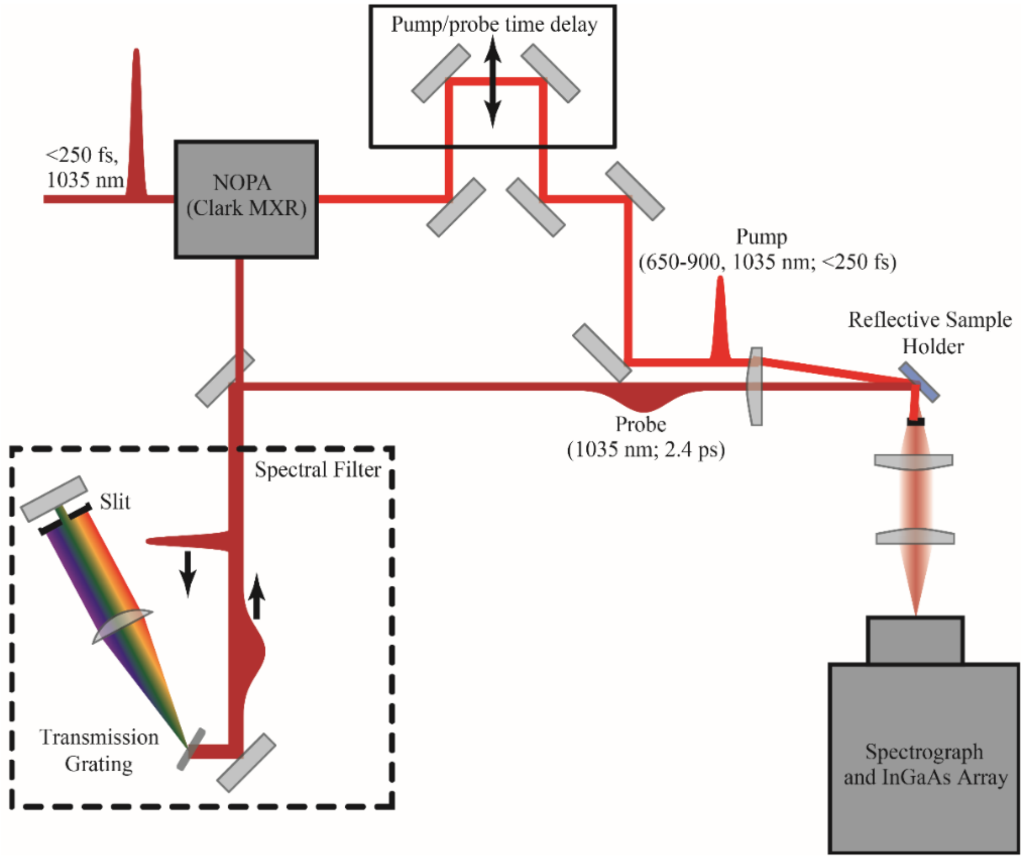

Figure 6.1 Schematic of the ultrafast SERS apparatus. The fundamental pulse was produced from a CLARK-MXR IMPULSE, which is spectrally centered at 1035 nm and has a duration <250 fs. The pump and probe pulses were created by splitting the fundamental beam. We then directed the probe pulse into a spectral filter (dashed box) to narrow the spectral bandwidth of the pulse, which broadens the pulse's duration. Depending on the desired experimental parameters, the pump pulse could be altered by a nonlinear optical parametric amplifier to produce wavelengths between 650-900 nm or it could be used at the fundamental 1035 nm for degenerate pump-probe measurements. We directed the pump pulse towards an automated delay stage, which was used to generate the time points in the ultrafast SERS experiment. Finally, we aligned the two pulses to the sample holder and collected the reflected scattered radiation into the detector assembly, which consisted of a spectrograph and a PyLon InGaAs photodiode array.

6.3.3 Motorized Sample Holder

The experiments we performed in this chapter were done using a custom-built motorized sample holder. The sample holder is designed to collect the reflected Raman scattering in a 90° orientation. Our goal was to construct a stage capable of translating the SERS substrates at an exceptionally fast velocity while maintaining a high-level of reproducibility in the measurements. The sample holder (**Figure 6.2**) was composed of a motorized actuator (LTA-HS, Newport Corporation) and linear translation stage (DDSM50, ThorLabs) to displace the sample vertically and horizontally, respectively. The DDSM50 is able to achieve driving speeds up to 500 mm/s and has a minimal step resolution of 500 nm. We determined that the linear translation stage would be able to translate a substrate the length of the focused laser's diameter (~250 µm)[7] in under 50 µs. In addition, we selected the LTA-HS for its ability to support a large weight load while achieving a moderately quick driving speed (5 mm/s). Together, these two motorized devices provided a rapid means of displacing the AuFON substrates in a rapid manner.

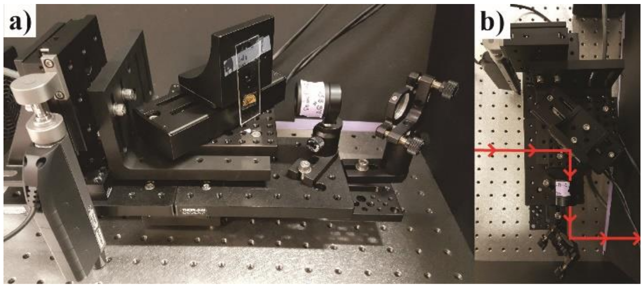

Figure 6.2 Custom-built motorized sample holder. The device consists of an LTA-HS and DDSM50 for vertical and horizontal displacement, respectively. (a) Front and (b) top-down view of the apparatus. The collimating optic is physically attached to the sample holder to ensure consistent alignment into the detection system.

6.4 Results and Discussion

The ultimate goal in designing the ultrafast SERS experiments detailed throughout this chapter was to spectroscopically identify and track the generation of transient intermediate species during a hot electron transfer event. As stated in the Introduction, obtaining a better understanding of the hot electron transfer mechanism is highly relevant for the plasmonic field as whole. With a more concrete description of the relevant parameters, such as the hot electron transfer efficiency and an associated lifetime of the transient intermediate species, the community will be able to build upon the pre-existing work to achieve more effective plasmonic systems. In designing this ultrafast SERS apparatus, our aim was to provide the necessary experimental parameters to successfully construct a detailed mechanistic description of plasmon-mediated hot electron transfer into a targeted molecular adsorbate.

Our approach towards identifying this short-lived phenomenon was to photoexcite the SERS substrate's surface plasmon with a femtosecond pump pulse and subsequently interrogate the molecular dynamics with a picosecond probe pulse as the molecules interact with the short-lived hot electrons. In the experiments discussed below, we preferentially modified the photoexcitation pump wavelength (650-900, 1035 nm) to ensure an overlap with the AuFON substrate's surface plasmon resonance. We performed experiments with a wide-range of pump wavelengths and found a degenerate pump-probe configuration to be the most effective. We hypothesize that this observation is linked to the surface plasmon's ability to direct and locally amplify different wavelengths of light to preferential spatial locations.

An experimental configuration where the pump and probe wavelengths are degenerate should allow for a more controlled study by providing photon sources that will couple most effectively to the same spatial region. However, we are limited with the wavelength of the probe pulse and we employ a 1035 nm pulse after it has been temporally broadened to a pulse duration of ~2.4 ps. In order to collect a SERS spectrum with adequate spectral resolution, we needed to reduce the spectral bandwidth of the 1035 nm pulse. This experimental constraint pushed the temporal resolution of our ultrafast SERS apparatus to the picosecond regime. Yet, we hypothesize that the relevant chemical dynamics that we are pursuing to observe, such as the making and breaking of chemical bonds or transient stabilization of certain singly reduced redox molecules, will occur in a time window that our ultrafast SERS apparatus will allow us to detect.

To identify and track the generation of transient intermediate species during a hot electron transfer event, we investigated the SER response of methyl viologen with a degenerate 1035 nm pump-probe experimental configuration. Methyl viologen is an extensively studied analyte in the broad field of electrochemistry[243-244] and more specifically, is found to be employed in a large number of biological redox reactions.[245, 263] It has repeatedly been demonstrated as an excellent electron accepting species, with a single electron redox potential of -0.45 V.[264] In these studies, we proposed that methyl viologen would serve as an ideal molecular analyte to harvest and transiently stabilize a portion of the hot electrons that are produced during the decay of a photoexcited surface plasmon. We would expect to see the transient production of the singly-reduced methyl viologen radical cation species, which has been spectroscopically identified in previous SERS experiments.[19]

However, when chemisorbed to the surface of AuFON substrates and exposed to an on-resonant source of photons, methyl viologen will undergo a plasmon-mediated photochemical conversion to form a new molecular species. During this conversion, we have observed the generation of new Raman features at 1024, 1066, and 1624 cm^{-1}. Although we are currently unable to accurately assign the identity of the methyl viologen photoproduct, probing these vibrational modes gives us information on chemical dynamics occurring during the picosecond timescale. For a more descriptive discussion into our analysis of the methyl viologen photoproduct, please refer to Chapter 5.

In **Figure 6.3**, we present ultrafast SERS spectra of methyl viologen on an AuFON substrate. The multiple differential spectra are representative of the transient molecular response of the coupled plasmon-molecule system. On the plot, there are two different type of spectra displayed: the above vertically offset spectra are differential transient spectra between -50 ps and 50 ps and the bottom spectrum is a “pump off” spectrum corresponding to the system’s steady-state SERS vibrational profile. The differential spectra are generated by subtracting a -50 ps reference spectrum away from each time point.[21] We employ this subtraction method to remove any pump-induced artifacts that may appear in the raw transient spectra. Additionally, we select a -50 ps reference spectrum due to the lack of interactions it may have with the probe pulse, which is due to the large temporal separation between the probe and pump pulses as they interact with the substrate. In this set of differential spectra, we observed a time-dependent depletion of the 1024, 1066, and 1624 cm^{-1} vibrational modes, all of which correspond to the unknown methyl viologen photoproduct. The transient depletion initiates at the -2 ps time point and rapidly decays over the next four picoseconds. At it its maximum, we observed a ~22% depletion in the photoproduct's Raman signal at the -1 ps time point.

The peak depletions that we have observed may arise from a number of phenomena. When exposed to such intense pulse energies, the chemisorbed molecules may desorb from the metal surface or experience varying levels of chemical degradation.[234] But, if this were the case, we would expect to see a permanent depletion in the transient spectra. Rather, in our experiments, the transient SERS signal is completely replenished, and we do not observe any lasting depletion. Another instance where peak depletions would be present is if the initial molecular analytes undergo a chemical reaction to a new product species on the surface. Similar to before, we would expect to see the

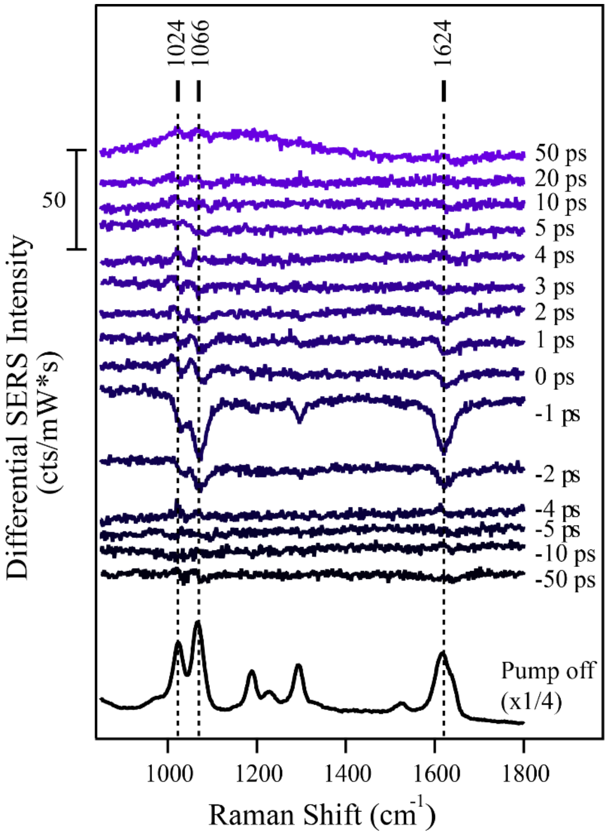

Figure 6.3 Transient depletion in the ultrafast SER spectra of methyl viologen on AuFON substrates. The three Raman-active modes associated to the methyl viologen photoproduct (1024, 1066, and 1624 cm^{-1}) experience a transient peak depletion. We collected the spectra with 0.5 mW (20 pJ) probe power, 0.85 mW (35 pJ) pump power, and an acquisition time of 15 seconds.

formation of transient product peaks in response to the depletion of a reactant peak. In these specific experiments, we ensured that the methyl viologen photoreaction had reached completion before collecting the transient SERS spectra. Also, we did not observe the growth of any positive peaks in the differential spectra. Therefore, an ultrafast plasmon-induced chemical reaction is not the prevailing mechanism driving the transient depletions that we observe in our experiments.

We hypothesize that the transient depletions are associated to a short-lived spectral shift of the localized surface plasmon resonance. Keller and Frontiera first reported this phenomenon when they observed similar peak depletions in their ultrafast SERS measurements on aggregated gold nanoparticles.[140] In their study, they observed transient depletions in the SER spectra of 4-nitrobenzenethiol (4-NBT). They proposed that the peak depletions were due to a red-shift in the colloid’s localized surface plasmon resonance, caused by an uneven perturbation to the plasmonic materials’ electron density. While our experiments employ an AuFON substrate rather than colloids, the AuFON substrate could experience a similar red-shift in its localized surface plasmon resonance.

In other instances, we were able to track the formation of dispersive features in the transient differential SER spectra. **Figure 6.4** displays two sets of ultrafast SERS trials where we studied both methyl viologen and tetracyanoquinodimethane (TCNQ) on AuFON substrates. Akin to methyl viologen, TCNQ is well known for its ability to serve as an electron accepting moiety and is commonly employed as the cation in charge transfer salts. Similar to the previous set of ultrafast SER spectra, we observed an initial transient depletion at -2 ps in both the methyl viologen and TCNQ studies. However, rather than only producing a depletion in the differential spectra, transient dispersive line shapes are present for all of the prominent vibrations in methyl viologen and its photoproduct (**Figure 6.4a)** and the 1382 cm^{-1} vibration for TCNQ (**Figure 6.4b**). Also, in these studies, the transient signatures last until ~10 ps in both the methyl viologen and TCNQ measurements.

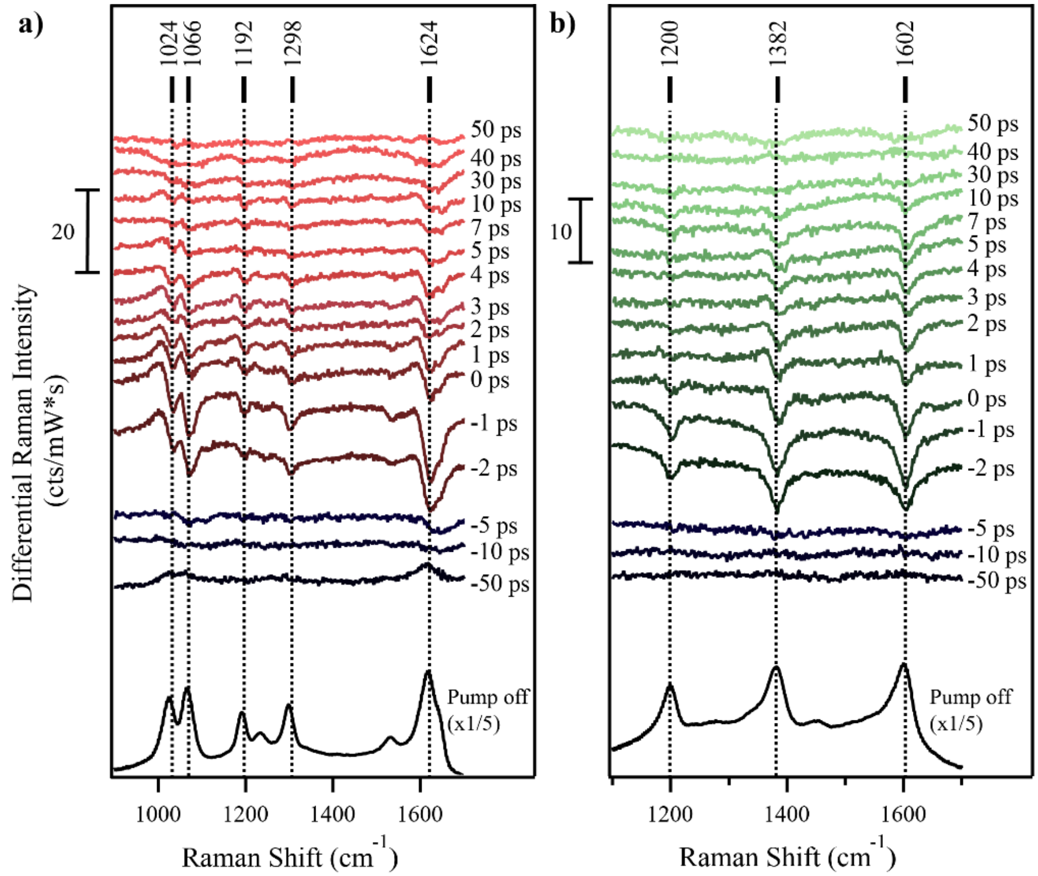

Figure 6.4 Transient dispersive responses in the ultrafast SER spectra of (a) methyl viologen and (b) TCNQ on AuFON substrates. We collected spectra with (a) 4 mW (0.16 nJ) probe power, 10 mW (0.41 nJ) pump power, and an acquisition time of 5 seconds and (b) with 5 mW (0.20 nJ) probe power, 7 mW (29 nJ) pump power, and an acquisition time of 5 seconds.

In a similar study, Brandt *et al*. determined that similar line shapes were transient Fano resonances in their silver colloidal substrates.[21] They were able to employ the ultrafast SERS apparatus as a tool to directly probe the plasmon-molecule interactions during the dimerization of 4-NBT to 4,4'-dimercaptoazobenzne (DMAB). The resulting Fano resonances, which were present in the 4-NBT and dimerized DMAB's vibrational modes, were attributed to the interference between the near-field coupling of the narrow Raman-active molecular transitions to the broad hot electron-induced metal photoluminescence of the AgNPs. The appearance of the dispersive line shapes in our transient spectra is evidence that we are not solely inducing a localized surface plasmon resonance shift in these studies. Rather, we believe that we are observing a similar coupling effect between a narrowband source and a broadband source in our ultrafast SER spectra. Similar to their study, the narrowband Raman-active molecular transitions are serving as one of the two coupled sources. We hypothesis that the broadband source in these experiments are due to either an electronic Raman response or photoluminescence.[265-267] Presently, there is a strong debate over which of these two mechanisms are prevalent in plasmonic materials. However, we are unable to confidently assign either broadband source as the key initiator in the observed Fano-like line shapes.

Lastly, we explored the possibility of using a fullerene derivative as a transient hot electron trap on oxide-coated AuFON substrates. We designed these experiments with the intention of producing an alternative pathway for hot electron transfer to occur. In this design, the metal-semiconductor interface would produce a Schottky barrier between the two materials. The excitation of the surface plasmon would generate an abundance of highly-energetic hot electrons on the plasmonic surface. Then, instead of inducing a direct electron transfer event to a metal-bound chemical analyte, the hot electrons would need to spatially travel through the semiconducting material. To do so, the electrons would need to be sufficient in energy to cross the Schottky barrier between the two materials.

The benefits behind this experimental design are two-fold. First, due to the metal-semiconductor Schottky barrier, the hot electrons would be much less likely to undergo a back transfer into the metal lattice. This would inherently increase the likelihood of inducing an interaction between the molecular adsorbates and an ejected hot electron. Secondly, depositing an oxide on the surface of the metal plasmonic material gives rise to an entirely new class of possible functional groups that can adhere to the material's surface. In the most commonly used plasmonic metals, such as gold and silver, surface specificity is achieved by selecting molecules that have specific chemical moieties, such as thiols, amines, and N-heterocyclic carbenes. Yet, with an oxide layer serving as the exposed surface, additional functional groups, such as hydroxyl or carboxyl groups, would provide a robust adherence to the material. With these factors in mind, we proposed to use a modified carboxylfullerene as the studied analyte. **Figure 6.5** shows the ultrafast SER spectra associated to tris-carboxylfullerene chemisorbed to the surface of an alumina-coated AuFON substrate. In this particular example, we deposited 7 Å of alumina (Al_2O_3) onto the AuFON, as that thickness proved sufficient for maintaining the distance-dependent SERS signal. We obtained the differential spectra by subtracting away a -50 ps reference from the time points. Also, the "pump off" spectrum on the bottom of the plot is the steady-state SER spectrum of tris-carboxylfullerene generated by the probe. We have denoted the primary Raman band in this molecule at 1455 cm^{-1}, which corresponds to the $A_g(2)$ mode in the fullerene derivative. If a singly reduced anionic fullerene were to have formed, we would expect to see a downshift of ~5 cm^{-1} in the $A_g(2)$ mode.[268] We did not observe the transient generation of an anionic fullerene species in any of our ultrafast SERS experiments.

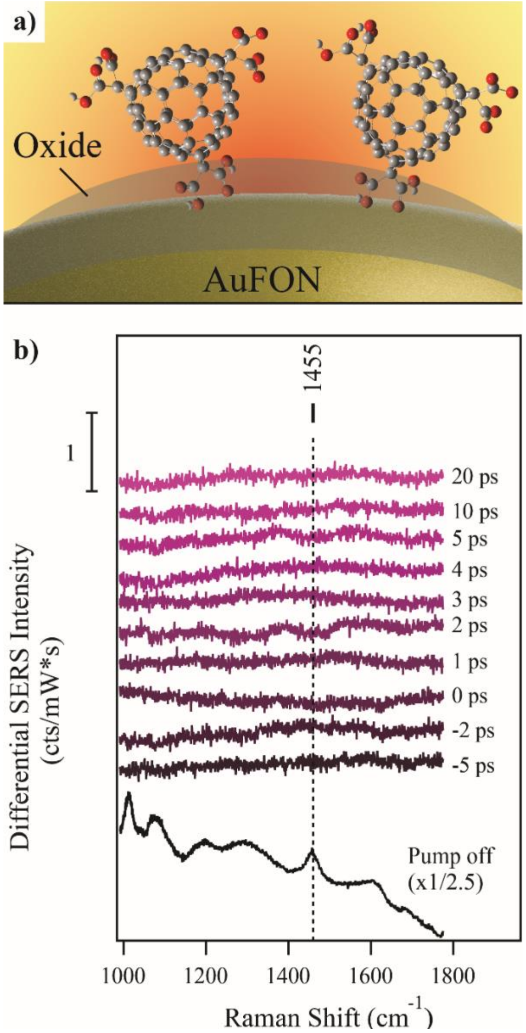

Figure 6.5 Probing the electron transfer process from AuFON substrates to chemisorbed tris-carboxylfullerene. (a) depiction the deposition of tris-carboxylfullerene onto the layer of an oxide deposition. (b) Time-resolved differential SER spectra of tris-carboxylfullerene on an Al_2O_3@AuFON substrate. No transient features were observed during the ultrafast exposures. The spectra were obtained with 9 mW (0.37 nJ) probe and 20 sec acquisition times.

Although we were unable to achieve our original goal of using ultrafast SERS to identify the formation of the intermediate species formed during a hot electron transfer event, we were able to identify transient photophysical responses. Observing transient hot electron transfer is a non-trivial research effort, as there has yet to be a published report of successfully using an ultrafast vibrational spectroscopic technique to observe any short-lived intermediate species associated to hot electron transfer. If fact, these results may suggest that plasmon-mediated photochemistry is not primarily driven by a hot electron transfer event. Rather, we believe it may be possible that these photochemical reactions are powered by one or more of the proposed plasmon energy transfer mechanisms, such as plasmon-induced resonance energy transfer (PIRET).[12, 46, 160, 269-270] In Chapter 7, we discuss our most recent advances towards modifying the experimental setup in an attempt to design a configuration better suited for observing transient intermediate species during ultrafast SERS measurements. Ideally, these new experimental methods should play instrumental in conclusively determining the underlying mechanism driving plasmon-mediated photochemical reactions.

6.5 Conclusion

In this chapter, we detailed our efforts towards using ultrafast SERS to spectroscopically track the formation of transient intermediates during a hot electron transfer event. We interrogated numerous molecular analytes, such as methyl viologen, TCNQ, and a fullerene derivative, but were unsuccessful in identifying any short-lived anionic species in our experiments. However, rather an observing any hot electron-induced intermediate species, we detected similar plasmonic photophysical effects that have been previously reported. Further modifications need to be applied to the experimental approaches towards better understanding hot electron transfer, which are detailed in Chapter 7. Ultimately, while we have been unable to spectroscopically provide a quantitative mechanistic description to the plasmonic community, obtaining the relevant mechanism should still be viewed as a critical step in fully-realizing the true potential of utilizing plasmonic platforms as photocatalysts.

6.6 Acknowledgements

We acknowledge the support from the Air Force Office of Scientific Research under AFOSR award no. FA9550-15-1-0022. Portions of this work were conducted in the Minnesota Nano Center, which is supported by the National Science Foundation through the National Nano Coordinated Infrastructure Network (NNCI) under Award Number ECCS-1542202. We would also like to thank the Haynes Lab at the University of Minnesota for allowing us to use their thermal evaporation deposition chamber for fabricating the AuFON substrates.

Chapter 7

Prospects

7.1 Rapid sample spinning for ultrafast SERS

The field of plasmonics has been rapidly growing due to the untapped potential of using plasmonic materials as light-activated catalysts. However, we believe that obtaining the optimal design of plasmonic photocatalysts is highly-dependent on determining a detailed description of the transient mechanism driving the catalytic processes. In an effort to provide clarity on this topic, we have been actively investigating plasmon-molecule interactions using ultrafast surface-enhanced Raman spectroscopy (SERS). Our goal was to spectroscopically identity the formation of transient intermediate species during a hot electron transfer event (Chapter 6). With this observation, we hypothesized that we would be able to quantitatively define the various parameters behind hot electron transfer, such as a transfer yield, a hot electron accessibility lifetime, etc. It is our belief that these results would inspire a rational design of plasmonic photocatalysts for initiating relevant chemical processes. However, this scientific challenge has proved to be a non-trivial endeavor, as we have been unable to achieve our original goal.

One possible experimental shortcoming in our previous ultrafast SER measurements (Chapter 6) was the prolonged exposure of photons to a single region on the AuFON substrate. To be more specific, we designed the experiments to collect three different sets of spectra for each time point. The three different sets of spectra were the pump off spectrum, a -50 ps reference spectrum, and the desired time point's spectrum. All three sets of spectra were required for an accurate analysis of the transient dynamics. We ensured that the set of spectra, all associated to an individual time point, were collected at a singular spatial region. Once all three were collected, the motorized sample stage would translate the substrate to a new position, resulting in the focal area being positioned onto a fresh region on the substrate. We employed this method to prevent the production of spectral artifacts when subtracting the spectra from two distinctly different regions on the substrate. In SERS measurements, it is very likely to observe discrete differences in the spectra when translating across the sample.[271] In theory, this collection method should generate spectra that can be easily subtracted to produce artifact-free transient spectra.

However, while we were reducing the likelihood of observing an undesired artifact in the transient spectra, we were also exposing each unique spatial region to a surplus of photons. In most of our experiments, we were continuously subjecting our pulsed lasers onto the same spatial location for over 120 seconds before transitioning to a new region on the substrate. There are two clear negative aspects for operating under these conditions. First, continuously directing high-energy pulses at the substrate will cause physical deteriorations to occur. These deteriorations can be due to a nanoscale alteration of the metal lattice, resulting in either a dramatic rise in the spectrum's background or permanent depletion in the Raman-active modes.[92] Alternatively, the continuous exposures can lead to chemical breakdown on the surface, which would significantly alter the vibrational features in the collected SER spectrum.[234]

The second negative characteristic of this experimental design is linked to the immense number of pulses used to collect our spectra. In the experiments highlighted in Chapter 6, we used an ultrafast laser that was set to a repetition rate of 24.5 MHz, meaning that a new pulse arrives at the sample nearly every 40 nanoseconds. When employing an instrument set to this repetition rate, a typical experiment using 20 second acquisition times and 3 spectral averages would require 4.9 x 10^8 pulses to generate the final SER spectrum. After continuously interacting with the surplus of high energy pulses, it is entirely possible that the photoexcited surface plasmon's ability to efficiently partition its initial energy into harvestable hot electrons has dramatically declined. Thus, the resulting SER spectrum would be constructed using a vast amount of pulses that were effectively "empty" and did not contain any relevant information pertaining to the initial plasmonic dynamics. Any relevant dynamics recorded in the initial pulses would be substantially overwhelmed by the pulses containing no pertinent transient information. We hypothesize that an ideal experimental approach would limit the number of interactions between the pulses and each distinct location on the AuFON substrate. With this in mind, we set out to develop an alternative method that reduces the undesirable single-region pulse saturation and generates a SER spectrum more representative of the early onset dynamics of an unagitated surface plasmon.

One approach towards tackling this challenge is to develop a new method of rapidly translating our SERS substrates during the ultrafast experiments. Recently, we have been working towards the development of a sample holder capable of translating AuFON substrates at rapid velocities. To do so, we implemented a hard disk drive (HDD) motor that can consistently rotate at high speeds (7,200 rpm). In this design, we load multiple AuFON substrates onto a single platter and mount it to the HDD motor (**Figure 7.1a**). The sample holder rapidly rotates the AuFON substrates in and out of the laser's focal region and generates an ensemble-averaged SER spectrum of the studied analyte from all of the mounted substrates. The rotational spinning also increases the effective area that is probed during a single ultrafast SERS measurement, as that area is directly proportional to the circumference of the circularly mounted AuFON substrates. When using a slower repetition rate (2 MHz, 250 µm spot size diameter), we would need to continuously translate our samples at a speed of 500 m/s to ensure that each pulse interacts with an entirely new region on the substrate. While this modified sample holder was unable to achieve that level of speed, we were able to significantly reduce the number of pulses to ~10 per every unique probed location on the substrate. Instead of oversaturating a region with a surplus of photons, the HDD motor displaces the substrate quickly enough to ensure that we are continuously probing fresh regions on the substrate.

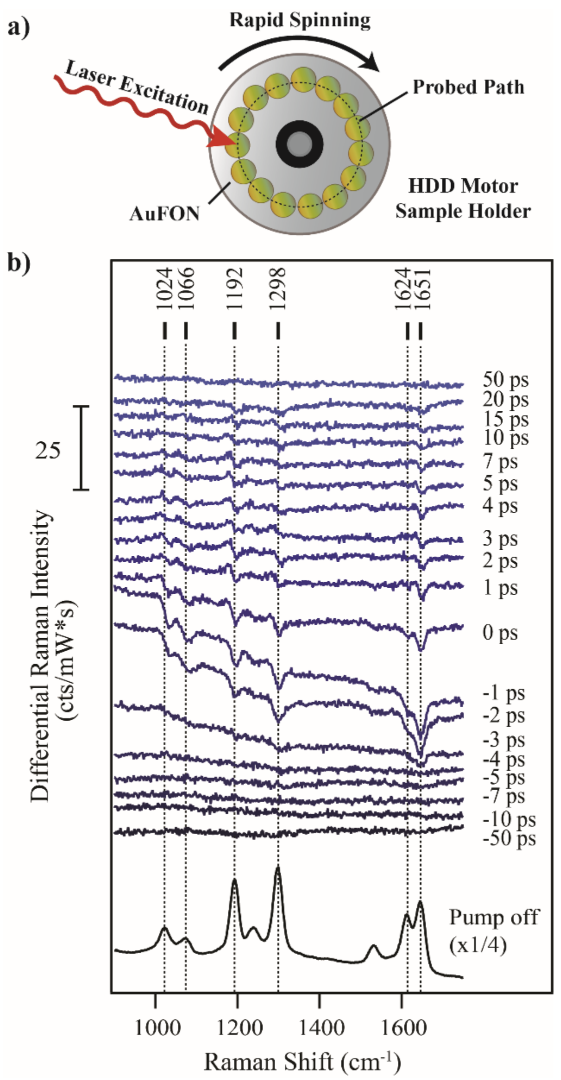

Figure 7.1 Ultrafast SERS measurements using a modified HDD sample holder. (a) Cartoon depiction of the experimental setup of mounting multiple AuFON substrates on the HDD's platter. (b) Transient dispersive responses in the ultrafast SER spectra of methyl viologen. We collected the spectra with a 3 mW (0.12 nJ) probe, 8 mW (0.33 nJ) pump, and an acquisition time of 5 s.

Figure 7.1b displays the ultrafast SER spectra of methyl viologen using the modified HDD sample holder. Similar to the results presented in Chapter 6, we observed a transient depletion in all of methyl viologen's prominent modes beginning at -2 ps. The vibrational modes at 1024, 1066, and 1624 cm^{-1} belong to the unknown methyl viologen photoproduct that is generated on AuFON substrates (Chapter 5), whereas the 1192, 1298, and 1651 cm^{-1} correspond to methyl viologen. Over the next two picoseconds, the transient features begin to evolve into dispersive line shapes and maintain this character until ~10 ps. These results are consistent to what we observed when using the motorized sample holder in Chapter 6. However, the modified HDD sample holder was able to reliably reproduce these transient results, whereas the results gathered with the motorized sample holder were extremely difficult to reproduce.

The modified HDD sample holder may prove instrumental in the pursuit of detecting a transient intermediate species during a hot electron transfer event. Distinguishing the ideal plasmon-molecule system appears to be the next step in making a substantial advancement towards successfully accomplishing our original goal of obtaining a better understanding of the transient hot electron transfer dynamics. While we were only able to experimentally reproduce the dispersive responses in methyl viologen's transient spectra collected with the motorized sample holder, the modified HDD sample holder greatly reduced the difficulty in replicating these results across multiple AuFON substrates. Ultimately, the HDD sample holder should provide the necessary experimental conditions to probe the transient response of fresh surface plasmons as they interact with nearby chemical adsorbates, hopefully unveiling a transient description of the underlying mechanism behind hot electron transfer.

7.2 Alternative plasmonic materials for SERS substrates

All of the research presented throughout this thesis was performed by implementing metal film over nanosphere substrates, specifically using gold as the plasmonic metal. As we have repeatedly demonstrated, AuFON substrates are a reliable and reproducible substrate for producing dramatically-enhanced Raman scattering for analytes of interest. While they may prove to be highly heterogenous across the surface, we showed that the substrates can inherently provide a local field gradient to extract field-dependent SERS results (Chapter 3). Additionally, we demonstrated that the local plasmonic fields generated by the AuFON substrates are capable of accessing entirely new reaction pathways for certain chemical analytes, such as a methyl migration and N-substituent cleavage on N-methylpyridinium (Chapter 4) and viologen derivates (Chapter 5), respectively.

However, while we achieved many experimental successes with AuFON substrates as our preferred SERS substrate, we did experience some non-trivial challenges that were due to fundamental flaws of the substrates. First, by using gold, we were heavily restricted to studying molecules with functional groups that have a strong affinity to the gold surface. Typically, the analytes had to contain a thiol or amine group to ensure a strong chemisorption to the surface. If a strong adherence wasn't made, seeing dramatic changes in the resulting vibrational spectrum would be expected when the flux applied onto the substrate was increased.

Along with the limited chemical selectivity, AuFON substrates lack robustness when exposed to high laser fluxes. In both continuous wave and pulsed laser measurements, we observed a depletion in the SERS signal and a dramatic rise in the spectrum's background. In the experiments where we employed a continuous wave laser as the excitation source, we noticed that the laser was damaging the SERS substrate when we approached fluxes of ~60 kW/cm^2. Additionally, due to the higher peak powers in pulsed lasers set to low repetition rates, we noticed a substantial difference in the quality of the SER spectra when operating our ultrafast apparatus at repetition rates of 2 and 24.5 MHz, and we were unable to generate a SER spectrum when using a 1 KHz laser. Essentially, we repeatably encountered situations where the AuFON substrate's durability hindered our experimental efforts.

As an attempt to assuage these issues, we explored the development of an alternative plasmonic FON substrate. In this work, we collaborated with the Oh Lab at the University of Minnesota to fabricate titanium nitride (TiN) FON substrates using atomic layer deposition (ALD). Titanium nitride is considered a promising alternative plasmonic material due its structural hardness,[272] ability to host plasmonic resonances in the visible and near-infrared regions,[40] and its cheap economic pricing. Ideally, a TiNFON would prove to be more robust in withstanding high laser power densities and allow for an entirely new class of adsorbates to use as molecular analytes.

To fabricate the substrates, we deposited a close-packed monolayer of silica nanospheres and deposited 100 – 200 nm of TiN using custom ALD recipes. Similar to AuFON substrates, we were able to control the central position of the substrate's plasmon resonance by simply altering the size of the silica nanobeads. In these experiments, we used silica bead sizes of 540, 600, and 750 nm and deposited roughly 200 nm of TiN. By increasing the size of the silica beads, we expect to see a corresponding red-shift in the substrate's surface plasmon resonance.

Figure 7.2 displays the percent reflectance spectra of three TiNFON substrates. As the figure shows, the three different bead sizes were able to produce plasmon resonances that spanned from the visible region to the near infrared. More specifically, the substrates fabricated with 540, 600, and 750 nm beads generated spectra with the plasmon resonances centered at 510, 790, and 886 nm, respectively.

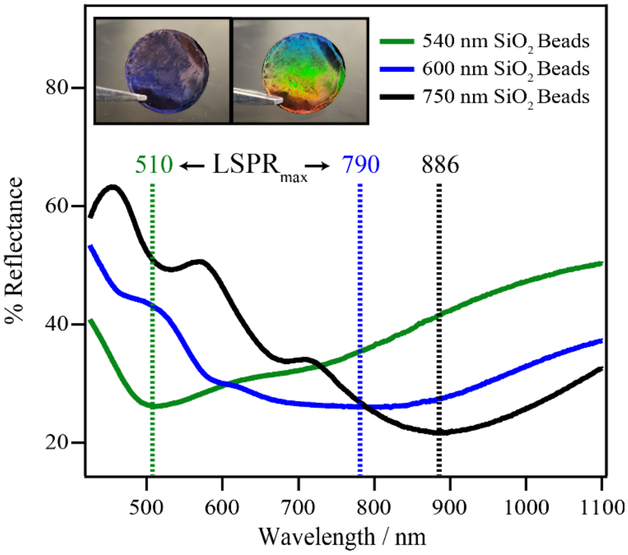

Figure 7.2 Percent reflectance spectra of the TiNFON substrates. The LSPR$_{max}$ wavelength for the substrates made with 540 (green), 600 (blue), and 750 nm (black) silica beads are 510, 790, and 886 nm, respectively. Inset displays images of a TiNFON substrate at different angles.

Unfortunately, we were unsuccessful in collecting a SER spectrum of a molecule deposited onto the surface of a TiNFON substrate. The difficulties in obtaining a SER spectrum with a TiNFON could be due to a couple of physical limitations of the material. First, it is possible that the TiNFON substrate was not able to produce the necessary field conditions to effectively enhance the Raman scattering of the studied molecular analytes. However, our UV-VIS-NIR measurements on the TiNFON substrates depict a noticeable depletion in the percent reflectance spectra where the surface plasmon resonances are spectrally positioned, demonstrating that the material is able to effectively generate and host surface plasmons. We observed substantial depletions in the percent reflectance spectra (~10%), which are comparable to the depletions we recorded for AuFON substrates. Theoretical models developed by Juneja and Shishodia further support our analysis that TiN is a suitable alternative plasmonic materials for generating surface plasmons in the NIR region.[273]

Rather, it seems more likely that the complications in collecting a chemisorbed analyte's SER spectrum is due to the inability of molecules to undergo surface functionalization on the material. We employed several chemical analytes in hopes of generating a SER spectrum. The molecules contained a wide-range of different functional groups that could be used to chemi- or physisorb to the TiN surface. These groups include, but are not limited to, thiols, carboxylic acids, amines, hydroxyls, phosphates, alkyls, and esters. In fact, there is a substantial dearth of literature discussing the surface functionalization of TiN, which may hint at a wide-spread struggle of inducing surface functionalization on TiN materials. However, recently there have been a report of chemically modifying the TiN surface to promote the adherence of silane functional groups.[274] This experimental technique may serve as an excellent alternative method to successfully promote a strong interaction between the analyte and TiN, allowing for the collection of a SER spectrum on TiNFON substrates.

If we are able to successfully functionalize the TiN surface with relevant chemical moieties, TiNFON substrates should prove to be a promising SERS substrate to study plasmon-mediated photochemistry. Compared to traditional metal plasmonic substrates, TiNFONs would provide a refreshing level of stability when exposed to high laser fluxes. While our chemical repository may be restricted to silane-containing molecules, the benefits gained from having a more robust substrate would be substantial. Ideally, the development of SERS-active TiNFONs can serve a vital role in studying plasmon-molecules interactions in both steady-state and transient regimes.

7.3 Conclusions

In conclusion, we have demonstrated that SERS is an excellent technique for understanding the capabilities of using plasmonic materials to access energetically unfavorable chemical reactions. Throughout this thesis, we have discussed our attempts towards expanding the repository of plasmon-mediated chemical reactions and using ultrafast spectroscopies to obtain a quantitative description of the transfer of hot electrons into nearby adsorbates. Advancing our experimental approaches, such as implementing new methods to interrogate our samples and developing more robust SERS substrates, may prove to be a crucial step in identifying intermediate species in our ultrafast measurements. Once we understand more about the transient dynamics of hot electron transfer, the plasmonics community should be able to dramatically advance the quality and efficacy of light-activated plasmonic catalysts, leading to a cost-effective implementation of powering industrially-relevant chemical reactions.

References

(1) Li, K.; Hogan, N. J.; Kale, M. J.; Halas, N. J.; Nordlander, P.; Christopher, P., Balancing Near-Field Enhancement, Absorption, and Scattering for Effective Antenna-Reactor Plasmonic Photocatalysis. *Nano Lett.* **2017,** *17* (6), 3710-3717.

(2) Hao, E.; Schatz, G. C., Electromagnetic Fields Around Silver Nanoparticles and Dimers. *J. Chem. Phys.* **2004,** *120* (1), 357-366.

(3) Manjavacas, A.; Liu, J. G.; Kulkarni, V.; Nordlander, P., Plasmon-Induced Hot Carriers in Metallic Nanoparticles. *ACS Nano* **2014,** *8* (8), 7630-7638.

(4) Sundararaman, R.; Narang, P.; Jermyn, A. S.; Goddard, W. A., 3rd; Atwater, H. A., Theoretical Predictions for Hot-Carrier Generation from Surface Plasmon Decay. *Nat. Commun.* **2014,** *5*, 5788.

(5) Adleman, J. R.; Boyd, D. A.; Goodwin, D. G.; Psaltis, D., Heterogenous Catalysis Mediated by Plasmon Heating. *Nano Lett.* **2009,** *9* (12), 4417-4423.

(6) Harris, N.; Ford, M. J.; Cortie, M. B., Optimization of Plasmonic Heating by Gold Nanospheres and Nanoshells. *J. Phys. Chem. B* **2006,** *110* (22), 10701-10707.

(7) Keller, E. L.; Frontiera, R. R., Ultrafast Nanoscale Raman Thermometry Proves Heating is not a Primary Mechanism for Plasmon-Driven Photocatalysis. *ACS Nano* **2018,** *12* (6), 5848-5855.

(8) Boerigter, C.; Aslam, U.; Linic, S., Mechanism of Charge Transfer from Plasmonic Nanostructures to Chemically Attached Materials. *ACS Nano* **2016,** *10* (6), 6108-6115.

(9) Brooks, J. L.; Warkentin, C. L.; Saha, D.; Keller, E. L.; Frontiera, R. R., Toward a Mechanistic Understanding of Plasmon-Mediated Photocatalysis. *Nanophotonics* **2018,** *7* (11), 1697-1724.

(10) Lee, J.; Mubeen, S.; Ji, X.; Stucky, G. D.; Moskovits, M., Plasmonic Photoanodes for Solar Water Splitting with Visible Light. *Nano Lett.* **2012,** *12* (9), 5014-5019.

(11) Mubeen, S.; Lee, J.; Singh, N.; Kramer, S.; Stucky, G. D.; Moskovits, M., An Autonomous Photosynthetic Device in which All Charge Carriers Derive from Surface Plasmons. *Nat. Nanotechnol.* **2013,** *8* (4), 247-251.

(12) Li, J.; Cushing, S. K.; Meng, F.; Senty, T. R.; Bristow, A. D.; Wu, N., Plasmon-Induced Resonance Energy Transfer for Solar Energy Conversion. *Nat. Photonics* **2015,** *9* (9), 601-607.

(13) Meng, F.; Cushing, S. K.; Li, J.; Hao, S.; Wu, N., Enhancement of Solar Hydrogen Generation by Synergistic Interaction of $La_2Ti_2O_7$ Photocatalyst with Plasmonic

Gold Nanoparticles and Reduced Graphene Oxide Nanosheets. *ACS Catal.* **2015,** *5* (3), 1949-1955.

(14) Swearer, D. F.; Zhao, H.; Zhou, L.; Zhang, C.; Robatjazi, H.; Martirez, J. M.; Krauter, C. M.; Yazdi, S.; McClain, M. J.; Ringe, E.; Carter, E. A.; Nordlander, P.; Halas, N. J., Heterometallic Antenna-Reactor Complexes for Photocatalysis. *Proc. Natl. Acad. Sci. U.S.A.* **2016,** *113* (32), 8916-8920.

(15) Zhou, L.; Swearer, D. F.; Zhang, C.; Robatjazi, H.; Zhao, H.; Henderson, L.; Dong, L.; Christopher, P.; Carter, E. A.; Nordlander, P.; Halas, N. J., Quantifying Hot Carrier and Thermal Contributions in Plasmonic Photocatalysis. *Science* **2018,** *362* (6410), 69-72.

(16) Tahir, M.; Tahir, B.; Amin, N. A. S., Gold-Nanoparticle-Modified TiO_2 Nanowires for Plasmon-Enhanced Photocatalytic CO_2 Reduction with H_2 under Visible Light Irradiation. *Appl. Surf. Sci.* **2015,** *356*, 1289-1299.

(17) Stiles, P. L.; Dieringer, J. A.; Shah, N. C.; Van Duyne, R. P., Surface-Enhanced Raman Spectroscopy. *Annu. Rev. Anal. Chem.* **2008,** *1* (1), 601-626.

(18) Di Martino, G.; Turek, V. A.; Lombardi, A.; Szabo, I.; de Nijs, B.; Kuhn, A.; Rosta, E.; Baumberg, J. J., Tracking Nanoelectrochemistry Using Individual Plasmonic Nanocavities. *Nano Lett.* **2017,** *17* (8), 4840-4845.

(19) de Nijs, B.; Benz, F.; Barrow, S. J.; Sigle, D. O.; Chikkaraddy, R.; Palma, A.; Carnegie, C.; Kamp, M.; Sundararaman, R.; Narang, P.; Scherman, O. A.; Baumberg, J. J., Plasmonic Tunnel Junctions for Single-Molecule Redox Chemistry. *Nat. Commun.* **2017,** *8* (1), 994.

(20) Brooks, J. L.; Frontiera, R. R., Competition between Reaction and Degradation Pathways in Plasmon-Driven Photochemistry. *J. Phys. Chem. C* **2016,** *120* (37), 20869-20876.

(21) Brandt, N. C.; Keller, E. L.; Frontiera, R. R., Ultrafast Surface-Enhanced Raman Probing of the Role of Hot Electrons in Plasmon-Driven Chemistry. *J. Phys. Chem. Lett.* **2016,** *7* (16), 3179-3185.

(22) Schultz, D. M.; Yoon, T. P., Solar Synthesis: Prospects in Visible Light Photocatalysis. *Science* **2014,** *343* (6174), 1239176.

(23) Fujishima, A.; Honda, K., Electrochemical Photolysis of Water at a Semiconductor Electrode. *Nature* **1972,** *238* (5358), 37-38.

(24) Pelaez, M.; Nolan, N. T.; Pillai, S. C.; Seery, M. K.; Falaras, P.; Kontos, A. G.; Dunlop, P. S. M.; Hamilton, J. W. J.; Byrne, J. A.; O'Shea, K.; Entezari, M. H.;

Dionysiou, D. D., A Review on the Visible Light Active Titanium Dioxide Photocatalysts for Environmental Applications. *Appl. Catal. B-Environ.* **2012,** *125*, 331-349.

(25) Dry, M. E., High Quality Diesel via the Fischer-Tropsch Process - A Review. *J. Chem. Technol. Biotechnol.* **2002,** *77* (1), 43-50.

(26) Galloway, J. N.; Townsend, A. R.; Erisman, J. W.; Bekunda, M.; Cai, Z.; Freney, J. R.; Martinelli, L. A.; Seitzinger, S. P.; Sutton, M. A., Transformation of the Nitrogen Cycle: Recent Trends, Questions, and Potential Solutions. *Science* **2008,** *320* (5878), 889-892.

(27) Oshikiri, T.; Ueno, K.; Misawa, H., Plasmon-Induced Ammonia Synthesis through Nitrogen Photofixation with Visible Light Irradiation. *Angew. Chem. Int. Ed.* **2014,** *53* (37), 9802-9805.

(28) Ali, M.; Zhou, F.; Chen, K.; Kotzur, C.; Xiao, C.; Bourgeois, L.; Zhang, X.; MacFarlane, D. R., Nanostructured Photoelectrochemical Solar Cell for Nitrogen Reduction using Plasmon-Enhanced Black Silicon. *Nat. Commun.* **2016,** *7*, 11335.

(29) Ursua, A.; Gandia, L. M.; Sanchis, P., Hydrogen Production From Water Electrolysis: Current Status and Future Trends. *Proc. IEEE* **2012,** *100* (2), 410-426.

(30) Balat, M., Potential Importance of Hydrogen as a Future Solution to Environmental and Transportation Problems. *Int. J. Hydrogen Energy* **2008,** *33* (15), 4013-4029.

(31) Song, H.; Meng, X.; Dao, T. D.; Zhou, W.; Liu, H.; Shi, L.; Zhang, H.; Nagao, T.; Kako, T.; Ye, J., Light-Enhanced Carbon Dioxide Activation and Conversion by Effective Plasmonic Coupling Effect of Pt and Au Nanoparticles. *ACS Appl. Mater. Inter.* **2018,** *10* (1), 408-416.

(32) Christopher, P.; Xin, H.; Linic, S., Visible-Light-Enhanced Catalytic Oxidation Reactions on Plasmonic Silver Nanostructures. *Nat. Chem.* **2011,** *3* (6), 467-472.

(33) Hung, W. H.; Aykol, M.; Valley, D.; Hou, W.; Cronin, S. B., Plasmon Resonant Enhancement of Carbon Monoxide Catalysis. *Nano Lett.* **2010,** *10* (4), 1314-1318.

(34) Liu, Z.; Hou, W.; Pavaskar, P.; Aykol, M.; Cronin, S. B., Plasmon Resonant Enhancement of Photocatalytic Water Splitting Under Visible Illumination. *Nano Lett.* **2011,** *11* (3), 1111-1116.

(35) Mukherjee, S.; Libisch, F.; Large, N.; Neumann, O.; Brown, L. V.; Cheng, J.; Lassiter, J. B.; Carter, E. A.; Nordlander, P.; Halas, N. J., Hot Electrons do the Impossible: Plasmon-Induced Dissociation of H_2 on Au. *Nano Lett.* **2013,** *13* (1), 240-247.

(36) Zheng, Z.; Tachikawa, T.; Majima, T., Plasmon-Enhanced Formic Acid Dehydrogenation using Anisotropic Pd-Au Nanorods Studied at the Single-Particle Level. *J. Am. Chem. Soc.* **2015,** *137* (2), 948-957.

(37) Hartland, G. V., Measurements of the Material Properties of Metal Nanoparticles by Time-Resolved Spectroscopy. *Phys. Chem. Chem. Phys.* **2004,** *6* (23), 5263-5274.

(38) Aruda, K. O.; Tagliazucchi, M.; Sweeney, C. M.; Hannah, D. C.; Weiss, E. A., The Role of Interfacial Charge Transfer-Type Interactions in the Decay of Plasmon Excitations in Metal Nanoparticles. *Phys. Chem. Chem. Phys.* **2013,** *15* (20), 7441-7449.

(39) Zhang, Y.; He, S.; Guo, W.; Hu, Y.; Huang, J.; Mulcahy, J. R.; Wei, W. D., Surface-Plasmon-Driven Hot Electron Photochemistry. *Chem. Rev.* **2018,** *118* (6), 2927-2954.

(40) Naik, G. V.; Schroeder, J. L.; Ni, X.; Kildishev, A. V.; Sands, T. D.; Boltasseva, A., Titanium Nitride as a Plasmonic Material for Visible and Near-Infrared Wavelengths. *Opt. Mater. Express* **2012,** *2* (4), 478-489.

(41) Garcia, G.; Buonsanti, R.; Runnerstrom, E. L.; Mendelsberg, R. J.; Llordes, A.; Anders, A.; Richardson, T. J.; Milliron, D. J., Dynamically Modulating the Surface Plasmon Resonance of Doped Semiconductor Nanocrystals. *Nano Lett.* **2011,** *11* (10), 4415-4420.

(42) Zhao, Y.; Burda, C., Development of Plasmonic Semiconductor Nanomaterials with Copper Chalcogenides for a Future with Sustainable Energy Materials. *Energy Environ. Sci.* **2012,** *5* (Energy & Environmental Science2), 5564-5576.

(43) Kelly, K. L.; Coronado, E.; Zhao, L. L.; Schatz, G. C., The Optical Properties of Metal Nanoparticles: The Influence of Size, Shape, and Dielectric Environment. *J. Phys. Chem. B* **2003,** *107* (3), 668-677.

(44) Schuller, J. A.; Barnard, E. S.; Cai, W.; Jun, Y. C.; White, J. S.; Brongersma, M. L., Plasmonics for Extreme Light Concentration and Manipulation. *Nat. Mater.* **2010,** *9* (3), 193-204.

(45) Aslam, U.; Chavez, S.; Linic, S., Controlling Energy Flow in Multimetallic Nanostructures for Plasmonic Catalysis. *Nat. Nanotechnol.* **2017,** *12* (10), 1000-1005.

(46) Cushing, S. K.; Li, J.; Meng, F.; Senty, T. R.; Suri, S.; Zhi, M.; Li, M.; Bristow, A. D.; Wu, N., Photocatalytic Activity Enhanced by Plasmonic Resonant Energy

Transfer from Metal to Semiconductor. *J. Am. Chem. Soc.* **2012,** *134* (36), 15033-15041.

(47) Yu, S.; Wilson, A. J.; Heo, J.; Jain, P. K., Plasmonic Control of Multi-Electron Transfer and C-C Coupling in Visible-Light-Driven CO_2 Reduction on Au Nanoparticles. *Nano Lett.* **2018,** *18* (4), 2189-2194.

(48) Ferry, V. E.; Sweatlock, L. A.; Pacifici, D.; Atwater, H. A., Plasmonic Nanostructure Design for Efficient Light Coupling into Solar Cells. *Nano Lett.* **2008,** *8* (12), 4391-4397.

(49) Ferry, V. E.; Verschuuren, M. A.; Li, H. B.; Verhagen, E.; Walters, R. J.; Schropp, R. E.; Atwater, H. A.; Polman, A., Light Trapping in Ultrathin Plasmonic Solar Cells. *Opt. Express* **2010,** *18 Suppl 2* (S2), A237-245.

(50) Gan, Q.; Bartoli, F. J.; Kafafi, Z. H., Plasmonic-Enhanced Organic Photovoltaics: Breaking the 10% Efficiency Barrier. *Adv. Mater.* **2013,** *25* (17), 2385-2396.

(51) Munday, J. N.; Atwater, H. A., Large Integrated Absorption Enhancement in Plasmonic Solar Cells by Combining Metallic Gratings and Antireflection Coatings. *Nano Lett.* **2011,** *11* (6), 2195-2201.

(52) Pala, R. A.; White, J.; Barnard, E.; Liu, J.; Brongersma, M. L., Design of Plasmonic Thin-Film Solar Cells with Broadband Absorption Enhancements. *Adv. Mater.* **2009,** *21* (34), 3504-3509.

(53) Reineck, P.; Lee, G. P.; Brick, D.; Karg, M.; Mulvaney, P.; Bach, U., A Solid-State Plasmonic Solar Cell via Metal Nanoparticle Self-Assembly. *Adv. Mater.* **2012,** *24* (35), 4750-4755, 4729.

(54) Wang, W.; Wu, S.; Reinhardt, K.; Lu, Y.; Chen, S., Broadband Light Absorption Enhancement in Thin-Film Silicon Solar Cells. *Nano Lett.* **2010,** *10* (6), 2012-2018.

(55) Ali, M. R.; Rahman, M. A.; Wu, Y.; Han, T.; Peng, X.; Mackey, M. A.; Wang, D.; Shin, H. J.; Chen, Z. G.; Xiao, H.; Wu, R.; Tang, Y.; Shin, D. M.; El-Sayed, M. A., Efficacy, Long-Term Toxicity, and Mechanistic studies of Gold Nanorods Photothermal Therapy of Cancer in Xenograft Mice. *Proc. Natl. Acad. Sci. U.S.A.* **2017,** *114* (15), E3110-E3118.

(56) Chen, J.; Wang, D.; Xi, J.; Au, L.; Siekkinen, A.; Warsen, A.; Li, Z. Y.; Zhang, H.; Xia, Y.; Li, X., Immuno Gold Nanocages with Tailored Optical Properties for Targeted Photothermal Destruction of Cancer Cells. *Nano Lett.* **2007,** *7* (5), 1318-1322.

(57) Huang, P.; Lin, J.; Li, W.; Rong, P.; Wang, Z.; Wang, S.; Wang, X.; Sun, X.; Aronova, M.; Niu, G.; Leapman, R. D.; Nie, Z.; Chen, X., Biodegradable Gold Nanovesicles with an Ultrastrong Plasmonic Coupling Effect for Photoacoustic Imaging and Photothermal Therapy. *Angew. Chem. Int. Ed.* **2013,** *52* (52), 13958-13964.

(58) Huang, X.; El-Sayed, I. H.; Qian, W.; El-Sayed, M. A., Cancer Cell Imaging and Photothermal Therapy in the Near-Infrared Region by using Gold Nanorods. *J. Am. Chem. Soc.* **2006,** *128* (6), 2115-2120.

(59) Loo, C.; Lin, A.; Hirsch, L.; Lee, M. H.; Barton, J.; Halas, N.; West, J.; Drezek, R., Nanoshell-Enabled Photonics-Based Imaging and Therapy of Cancer. *Technol. Cancer. Res. Treat.* **2004,** *3* (1), 33-40.

(60) Mackey, M. A.; Ali, M. R.; Austin, L. A.; Near, R. D.; El-Sayed, M. A., The Most Effective Gold nanorod Size for Plasmonic Photothermal Therapy: Theory and In Vitro Experiments. *J. Phys. Chem. B* **2014,** *118* (5), 1319-1326.

(61) Wang, S.; Huang, P.; Nie, L.; Xing, R.; Liu, D.; Wang, Z.; Lin, J.; Chen, S.; Niu, G.; Lu, G.; Chen, X., Single Continuous Wave Laser Induced Photodynamic/Plasmonic Photothermal Therapy using Photosensitizer-Functionalized Gold Nanostars. *Adv. Mater.* **2013,** *25* (22), 3055-3061.

(62) Hartland, G. V., Optical Studies of Dynamics in Noble Metal Nanostructures. *Chem. Rev.* **2011,** *111* (6), 3858-3887.

(63) Kleinman, S. L.; Sharma, B.; Blaber, M. G.; Henry, A. I.; Valley, N.; Freeman, R. G.; Natan, M. J.; Schatz, G. C.; Van Duyne, R. P., Structure Enhancement Factor Relationships in Single Gold Nanoantennas by Surface-Enhanced Raman Excitation Spectroscopy. *J. Am. Chem. Soc.* **2013,** *135* (1), 301-308.

(64) Lesina, A. C.; Vaccari, A.; Berini, P.; Ramunno, L., On the Convergence and Accuracy of the FDTD Method for Nanoplasmonics. *Opt. Express* **2015,** *23* (8), 10481-10497.

(65) Jeanmaire, D. L.; Van Duyne, R. P., Surface Raman Spectroelectrochemistry. *J. Electroanal. Chem.* **1977,** *84* (1), 1-20.

(66) Le Ru, E. C.; Etchegoin, P., *Principles of Surface-Enhanced Raman Spectroscopy: and Related Plasmonic Effects*. Elsevier Science: 2008.

(67) Hartstein, A.; Kirtley, J. R.; Tsang, J. C., Enhancement of the Infrared Absorption from Molecular Monolayers with Thin Metal Overlayers. *Phys. Rev. Lett.* **1980,** *45* (3), 201-204.

(68) Osawa, M.; Ataka, K.-I.; Yoshii, K.; Nishikawa, Y., Surface-Enhanced Infrared Spectroscopy: The Origin of the Absorption Enhancement and Band Selection Rule in the Infrared Spectra of Molecules Adsorbed on Fine Metal Particles. *Appl. Spectrosc.* **2016,** *47* (9), 1497-1502.

(69) Liebermann, T.; Knoll, W., Surface-Plasmon Field-Enhanced Fluorescence Spectroscopy. *Colloids Surf., A* **2000,** *171* (1-3), 115-130.

(70) Gersten, J.; Nitzan, A., Spectroscopic Properties of Molecules Interacting with Small Dielectric Particles. *J. Chem. Phys.* **1981,** *75* (3), 1139-1152.

(71) Li, X.; Xiao, D.; Zhang, Z., Landau Damping of Quantum Plasmons in Metal Nanostructures. *New J Phys* **2013,** *15* (2).

(72) Brongersma, M. L.; Halas, N. J.; Nordlander, P., Plasmon-Induced Hot Carrier Science and Technology. *Nat. Nanotechnol.* **2015,** *10* (1), 25-34.

(73) Link, S.; El-Sayed, M. A., Size and Temperature Dependence of the Plasmon Absorption of Colloidal Gold Nanoparticles. *J. Phys. Chem. B* **1999,** *103* (21), 4212-4217.

(74) Sonnichsen, C.; Franzl, T.; Wilk, T.; von Plessen, G.; Feldmann, J.; Wilson, O.; Mulvaney, P., Drastic Reduction of Plasmon Damping in Gold Nanorods. *Phys. Rev. Lett.* **2002,** *88* (7), 077402.

(75) Ahmadi, T. S.; Logunov, S. L.; El-Sayed, M. A., Picosecond Dynamics of Colloidal Gold Nanoparticles. *J. Phys. Chem.* **1996,** *100* (20), 8053-8056.

(76) Aruda, K. O.; Tagliazucchi, M.; Sweeney, C. M.; Hannah, D. C.; Schatz, G. C.; Weiss, E. A., Identification of Parameters through which Surface Chemistry Determines the Lifetimes of Hot Electrons in Small Au Nanoparticles. *Proc. Natl. Acad. Sci. U.S.A.* **2013,** *110* (11), 4212-4217.

(77) Herzog, J. B.; Knight, M. W.; Natelson, D., Thermoplasmonics: Quantifying Plasmonic Heating in Single Nanowires. *Nano Lett.* **2014,** *14* (2), 499-503.

(78) Pissuwan, D.; Valenzuela, S. M.; Cortie, M. B., Therapeutic Possibilities of Plasmonically Heated Gold Nanoparticles. *Trends Biotechnol.* **2006,** *24* (2), 62-67.

(79) Neumann, O.; Feronti, C.; Neumann, A. D.; Dong, A.; Schell, K.; Lu, B.; Kim, E.; Quinn, M.; Thompson, S.; Grady, N.; Nordlander, P.; Oden, M.; Halas, N. J., Compact Solar Autoclave Based on Steam Generation using Broadband Light-Harvesting Nanoparticles. *Proc. Natl. Acad. Sci. U.S.A.* **2013,** *110* (29), 11677-11681.

(80) Zharov, V. P.; Mercer, K. E.; Galitovskaya, E. N.; Smeltzer, M. S., Photothermal Nanotherapeutics and Nanodiagnostics for Selective Killing of Bacteria Targeted with Gold Nanoparticles. *Biophys. J.* **2006,** *90* (2), 619-627.

(81) Cao, L.; Barsic, D. N.; Guichard, A. R.; Brongersma, M. L., Plasmon-Assisted Local Temperature Control to Pattern Individual Semiconductor Nanowires and Carbon nanotubes. *Nano Lett.* **2007,** *7* (11), 3523-3527.

(82) Röntzsch, L.; Heinig, K.-H.; Schuller, J. A.; Brongersma, M. L., Thin film Patterning by Surface-Plasmon-Induced Thermocapillarity. *Appl. Phys. Lett.* **2007,** *90* (4), 044105.

(83) Khurgin, J. B., How to Deal with the Loss in Plasmonics and Metamaterials. *Nat. Nanotechnol.* **2015,** *10* (1), 2-6.

(84) Kazuma, E.; Jung, J.; Ueba, H.; Trenary, M.; Kim, Y., Real-Space and Real-Time Observation of a Plasmon-Induced Chemical Reaction of a Single Molecule. *Science* **2018,** *360* (6388), 521-526.

(85) Somorjai, G. A.; Li, Y., *Introduction to Surface Chemistry and Catalysis*. John Wiley & Sons: 2010.

(86) Kolasinski, K. W., *Surface Science: Foundations of Catalysis and Nanoscience*. John Wiley & Sons: 2012.

(87) Ertl, G.; Knözinger, H.; Weitkamp, J., *Handbook of Heterogeneous Catalysis*. Wiley-VCH: 1997.

(88) Bonn, M.; Funk, S.; Hess, C.; Denzler, D. N.; Stampfl, C.; Scheffler, M.; Wolf, M.; Ertl, G., Phonon- Versus Electron-Mediated Desorption and Oxidation of CO on Ru(0001). *Science* **1999,** *285* (5430), 1042-1045.

(89) Diebold, U., The Surface Science of Titanium Dioxide. *Surf. Sci. Rep.* **2003,** *48* (5-8), 53-229.

(90) Moskovits, M., Surface-Enhanced Spectroscopy. *Rev. Mod. Phys.* **1985,** *57* (3), 783-826.

(91) Goddard, G.; Brown, L. O.; Habbersett, R.; Brady, C. I.; Martin, J. C.; Graves, S. W.; Freyer, J. P.; Doorn, S. K., High-Resolution Spectral Analysis of Individual SERS-Active Nanoparticles in Flow. *J. Am. Chem. Soc.* **2010,** *132* (17), 6081-6090.

(92) Fang, Y.; Seong, N. H.; Dlott, D. D., Measurement of the Distribution of Site Enhancements in Surface-Enhanced Raman Scattering. *Science* **2008,** *321* (5887), 388-392.

(93) Kleinman, S. L.; Frontiera, R. R.; Henry, A. I.; Dieringer, J. A.; Van Duyne, R. P., Creating, Characterizing, and Controlling Chemistry with SERS Hot Spots. *Phys. Chem. Chem. Phys.* **2013,** *15* (1), 21-36.

(94) Li, P.; Ma, B.; Yang, L.; Liu, J., Hybrid Single Nanoreactor for In Situ SERS Monitoring of Plasmon-Driven and Small Au Nanoparticles Catalyzed Reactions. *Chem. Comm. (Camb.)* **2015,** *51* (57), 11394-11397.

(95) Liu, H.; Zhang, L.; Lang, X.; Yamaguchi, Y.; Iwasaki, H.; Inouye, Y.; Xue, Q.; Chen, M., Single Molecule Detection from a Large-Scale SERS-Active $Au_{79}Ag_{21}$ Substrate. *Sci. Rep.* **2011,** *1*, 112.

(96) Nie, S.; Emory, S. R., Probing Single Molecules and Single Nanoparticles by Surface-Enhanced Raman Scattering. *Science* **1997,** *275* (5303), 1102-1106.

(97) Petti, L.; Capasso, R.; Rippa, M.; Pannico, M.; La Manna, P.; Peluso, G.; Calarco, A.; Bobeico, E.; Musto, P., A Plasmonic Nanostructure Fabricated by Electron Beam Lithography as a Sensitive and Highly Homogeneous SERS Substrate for Bio-Sensing Applications. *Vib. Spectrosc.* **2016,** *82*, 22-30.

(98) Xie, W.; Walkenfort, B.; Schlucker, S., Label-Free SERS Monitoring of Chemical Reactions Catalyzed by Small Gold Nanoparticles using 3D Plasmonic Superstructures. *J. Am. Chem. Soc.* **2013,** *135* (5), 1657-1660.

(99) Yin, Z.; Wang, Y.; Song, C.; Zheng, L.; Ma, N.; Liu, X.; Li, S.; Lin, L.; Li, M.; Xu, Y.; Li, W.; Hu, G.; Fang, Z.; Ma, D., Hybrid Au-Ag Nanostructures for Enhanced Plasmon-Driven Catalytic Selective Hydrogenation through Visible Light Irradiation and Surface-Enhanced Raman Scattering. *J. Am. Chem. Soc.* **2018,** *140* (3), 864-867.

(100) Zhang, X.; Dai, Z.; Si, S.; Zhang, X.; Wu, W.; Deng, H.; Wang, F.; Xiao, X.; Jiang, C., Ultrasensitive SERS Substrate Integrated with Uniform Subnanometer Scale "Hot Spots" Created by a Graphene Spacer for the Detection of Mercury Ions. *Small* **2017,** *13* (9), 1603347.

(101) Joshi, G. K.; White, S. L.; Johnson, M. A.; Sardar, R.; Jain, P. K., Ultrashort, Angstrom-Scale Decay of Surface-Enhanced Raman Scattering at Hot Spots. *J. Phys. Chem. C* **2016,** *120* (43), 24973-24981.

(102) Masango, S. S.; Hackler, R. A.; Large, N.; Henry, A. I.; McAnally, M. O.; Schatz, G. C.; Stair, P. C.; Van Duyne, R. P., High-Resolution Distance Dependence Study of Surface-Enhanced Raman Scattering Enabled by Atomic Layer Deposition. *Nano Lett.* **2016,** *16* (7), 4251-4259.

(103) Shin, K. S.; Lee, H. S.; Joo, S. W.; Kim, K., Surface-Induced Photoreduction of 4-Nitrobenzenethiol on Cu Revealed by Surface-Enhanced Raman Scattering Spectroscopy. *J. Phys. Chem. C* **2007,** *111* (42), 15223-15227.

(104) Liu, X.; Tang, L.; Niessner, R.; Ying, Y.; Haisch, C., Nitrite-Rriggered Surface Plasmon-Assisted Catalytic Conversion of p-Aminothiophenol to p,p'-Dimercaptoazobenzene on Gold Nanoparticle: Surface-Enhanced Raman Scattering Investigation and Potential for Nitrite Detection. *Anal. Chem.* **2015,** *87* (1), 499-506.

(105) Lee, S. J.; Kim, K., Surface-Induced Photoreaction of 4-nitrobenzenethiol on Silver: Influence of SERS-Active Sites. *Chem. Phys. Lett.* **2003,** *378* (1-2), 122-127.

(106) Kim, K.; Choi, J.-Y.; Shin, K. S., Photoreduction of 4-Nitrobenzenethiol on Au by Hot Electrons Plasmonically Generated from Ag Nanoparticles: Gap-Mode Surface-Enhanced Raman Scattering Observation. *J. Phys. Chem. C* **2015,** *119* (9), 5187-5194.

(107) Huang, Y. F.; Zhu, H. P.; Liu, G. K.; Wu, D. Y.; Ren, B.; Tian, Z. Q., When the Signal is not from the Original Molecule to be Detected: Chemical Transformation of Para-Aminothiophenol on Ag during the SERS Measurement. *J. Am. Chem. Soc.* **2010,** *132* (27), 9244-9246.

(108) Dong, B.; Fang, Y.; Xia, L.; Xu, H.; Sun, M., Is 4-Nitrobenzenethiol Converted to p,p′-Dimercaptoazobenzene or 4-Aminothiophenol by Surface Photochemistry Reaction? *J. Raman Spectrosc.* **2011,** *42* (6), 1205-1206.

(109) Dong, B.; Fang, Y.; Chen, X.; Xu, H.; Sun, M., Substrate-, Wavelength-, and Time-Dependent Plasmon-Assisted Surface Catalysis Reaction of 4-Nitrobenzenethiol Dimerizing to p,p'-Dimercaptoazobenzene on Au, Ag, and Cu Films. *Langmuir* **2011,** *27* (17), 10677-10682.

(110) Kneipp, K.; Wang, Y.; Kneipp, H.; Perelman, L. T.; Itzkan, I.; Dasari, R. R.; Feld, M. S., Single Molecule Detection Using Surface-Enhanced Raman Scattering (SERS). *Phys. Rev. Lett.* **1997,** *78* (9), 1667-1670.

(111) Kleinman, S. L.; Ringe, E.; Valley, N.; Wustholz, K. L.; Phillips, E.; Scheidt, K. A.; Schatz, G. C.; Van Duyne, R. P., Single-Molecule Surface-Enhanced Raman Spectroscopy of Crystal Violet Isotopologues: Theory and Experiment. *J. Am. Chem. Soc.* **2011,** *133* (11), 4115-4122.

(112) Camden, J. P.; Dieringer, J. A.; Wang, Y.; Masiello, D. J.; Marks, L. D.; Schatz, G. C.; Van Duyne, R. P., Probing the Structure of Single-Molecule Surface-Enhanced Raman Scattering Hot Spots. *J. Am. Chem. Soc.* **2008,** *130* (38), 12616-12617.

(113) Le Ru, E. C.; Meyer, M.; Etchegoin, P. G., Proof of Single-Molecule Sensitivity in Surface Enhanced Raman Scattering (SERS) by Means of a Two-Analyte Technique. *J. Phys. Chem. B* **2006,** *110* (4), 1944-1948.

(114) Dieringer, J. A.; Lettan, R. B., 2nd; Scheidt, K. A.; Van Duyne, R. P., A Frequency Domain Existence Proof of Single-Molecule Surface-Enhanced Raman Spectroscopy. *J. Am. Chem. Soc.* **2007,** *129* (51), 16249-16256.

(115) Xu, H.; Bjerneld, E. J.; Käll, M.; Börjesson, L., Spectroscopy of Single Hemoglobin Molecules by Surface Enhanced Raman Scattering. *Phys. Rev. Lett.* **1999,** *83* (21), 4357-4360.

(116) Kneipp, K.; Kneipp, H.; Deinum, G.; Itzkan, I.; Dasari, R. R.; Feld, M. S., Single-Molecule Detection of a Cyanine Dye in Silver Colloidal Solution Using Near-Infrared Surface-Enhanced Raman Scattering. *Appl. Spectrosc.* **2016,** *52* (2), 175-178.

(117) Sprague-Klein, E. A.; McAnally, M. O.; Zhdanov, D. V.; Zrimsek, A. B.; Apkarian, V. A.; Seideman, T.; Schatz, G. C.; Van Duyne, R. P., Observation of Single Molecule Plasmon-Driven Electron Transfer in Isotopically Edited 4,4'-Bipyridine Gold Nanosphere Oligomers. *J. Am. Chem. Soc.* **2017,** *139* (42), 15212-15221.

(118) Choi, H. K.; Park, W. H.; Park, C. G.; Shin, H. H.; Lee, K. S.; Kim, Z. H., Metal-Catalyzed Chemical Reaction of Single Molecules Directly Probed by Vibrational Spectroscopy. *J. Am. Chem. Soc.* **2016,** *138* (13), 4673-4684.

(119) Sonntag, M. D.; Chulhai, D.; Seideman, T.; Jensen, L.; Van Duyne, R. P., The Origin of Relative Intensity Fluctuations in Single-Molecule Tip-Enhanced Raman Spectroscopy. *J. Am. Chem. Soc.* **2013,** *135* (45), 17187-17192.

(120) Zrimsek, A. B.; Wong, N. L.; Van Duyne, R. P., Single Molecule Surface-Enhanced Raman Spectroscopy: A Critical Analysis of the Bianalyte versus Isotopologue Proof. *J. Phys. Chem. C* **2016,** *120* (9), 5133-5142.

(121) Taylor, R. W.; Lee, T. C.; Scherman, O. A.; Esteban, R.; Aizpurua, J.; Huang, F. M.; Baumberg, J. J.; Mahajan, S., Precise Subnanometer Plasmonic Junctions for SERS within Gold Nanoparticle Assemblies using Cucurbit[n]uril "Glue". *ACS Nano* **2011,** *5* (5), 3878-3887.

(122) Kim, N. H.; Hwang, W.; Baek, K.; Rohman, M. R.; Kim, J.; Kim, H. W.; Mun, J.; Lee, S. Y.; Yun, G.; Murray, J.; Ha, J. W.; Rho, J.; Moskovits, M.; Kim, K., Smart SERS Hot Spots: Single Molecules Can Be Positioned in a Plasmonic Nanojunction Using Host-Guest Chemistry. *J. Am. Chem. Soc.* **2018,** *140* (13), 4705-4711.

(123) Wessel, J., Surface-Enhanced Optical Microscopy. *J. Opt. Soc. Am. B* **1985,** *2* (9), 1538-1541.

(124) Anderson, M. S., Locally Enhanced Raman Spectroscopy with an Atomic Force Microscope. *Appl. Phys. Lett.* **2000,** *76* (21), 3130-3132.

(125) Hayazawa, N.; Inouye, Y.; Sekkat, Z.; Kawata, S., Metallized Tip Amplification of Near-Field Raman Scattering. *Opt. Commun.* **2000,** *183* (1-4), 333-336.

(126) Stöckle, R. M.; Suh, Y. D.; Deckert, V.; Zenobi, R., Nanoscale Chemical Analysis by Tip-Enhanced Raman Spectroscopy. *Chem. Phys. Lett.* **2000,** *318* (1-3), 131-136.

(127) Sonntag, M. D.; Klingsporn, J. M.; Garibay, L. K.; Roberts, J. M.; Dieringer, J. A.; Seideman, T.; Scheidt, K. A.; Jensen, L.; Schatz, G. C.; Van Duyne, R. P., Single-Molecule Tip-Enhanced Raman Spectroscopy. *J. Phys. Chem. C* **2011,** *116* (1), 478-483.

(128) Bailo, E.; Deckert, V., Tip-Enhanced Raman Spectroscopy of Single RNA Strands: Towards a Novel Direct-Sequencing Method. *Angew. Chem. Int. Ed.* **2008,** *47* (9), 1658-1661.

(129) Zhang, Z.; Sheng, S.; Wang, R.; Sun, M., Tip-Enhanced Raman Spectroscopy. *Anal. Chem.* **2016,** *88* (19), 9328-9346.

(130) Hayazawa, N.; Saito, Y.; Kawata, S., Detection and Characterization of Longitudinal Field for Tip-Enhanced Raman Spectroscopy. *Appl. Phys. Lett.* **2004,** *85* (25), 6239-6241.

(131) Pettinger, B.; Domke, K. F.; Zhang, D.; Picardi, G.; Schuster, R., Tip-Enhanced Raman Scattering: Influence of the Tip-Surface Geometry on Optical Resonance and Enhancement. *Surf. Sci.* **2009,** *603* (10-12), 1335-1341.

(132) Kazemi-Zanjani, N.; Vedraine, S.; Lagugne-Labarthet, F., Localized Enhancement of Electric Field in Tip-Enhanced Raman Spectroscopy using Radially and Linearly Polarized Light. *Opt. Express* **2013,** *21* (21), 25271-25276.

(133) Deckert-Gaudig, T.; Richter, M.; Knebel, D.; Jahnke, T.; Jankowski, T.; Stock, E.; Deckert, V., A Modified Transmission Tip-Enhanced Raman Scattering (TERS) Setup Provides Access to Opaque Samples. *Appl. Spectrosc.* **2014,** *68* (8), 916-919.

(134) Sun, M.; Zhang, Z.; Zheng, H.; Xu, H., In-situ Plasmon-Driven Chemical Reactions Revealed by High Vacuum Tip-Enhanced Raman Spectroscopy. *Sci. Rep.* **2012,** *2*, 647.

(135) van Schrojenstein Lantman, E. M.; Deckert-Gaudig, T.; Mank, A. J. G.; Deckert, V.; Weckhuysen, B. M., Catalytic Processes Monitored at the nanoscale with Tip-Enhanced Raman Spectroscopy. *Nat. Nanotechnol.* **2012,** *7*, 583.

(136) Zhang, Z.; Chen, L.; Sun, M.; Ruan, P.; Zheng, H.; Xu, H., Insights into the Nature of Plasmon-Driven Catalytic Reactions Revealed by HV-TERS. *Nanoscale* **2013,** *5* (8), 3249-3252.

(137) Kumar, N.; Stephanidis, B.; Zenobi, R.; Wain, A. J.; Roy, D., Nanoscale Mapping of Catalytic Activity using Tip-Enhanced Raman Spectroscopy. *Nanoscale* **2015,** *7* (16), 7133-7137.

(138) Yeo, B.-S.; Stadler, J.; Schmid, T.; Zenobi, R.; Zhang, W., Tip-Enhanced Raman Spectroscopy – Its Status, Challenges and Future Directions. *Chem. Phys. Lett.* **2009,** *472* (1-3), 1-13.

(139) Ren, B.; Picardi, G.; Pettinger, B., Preparation of Gold Tips Suitable for Tip-Enhanced Raman Spectroscopy and Light Emission by Electrochemical Etching. *Rev. Sci. Instrum.* **2004,** *75* (4), 837-841.

(140) Keller, E. L.; Frontiera, R. R., Monitoring Charge Density Delocalization upon Plasmon Excitation with Ultrafast Surface-Enhanced Raman Spectroscopy. *ACS Photonics* **2017,** *4* (5), 1033-1039.

(141) Gruenke, N. L.; McAnally, M. O.; Schatz, G. C.; Van Duyne, R. P., Balancing the Effects of Extinction and Enhancement for Optimal Signal in Surface-Enhanced Femtosecond Stimulated Raman Spectroscopy. *J. Phys. Chem. C* **2016,** *120* (51), 29449-29454.

(142) Zhang, Y.; Zhen, Y. R.; Neumann, O.; Day, J. K.; Nordlander, P.; Halas, N. J., Coherent Anti-Stokes Raman Scattering with Single-Molecule Sensitivity using a Plasmonic Fano Resonance. *Nat. Commun.* **2014,** *5*, 4424.

(143) Crampton, K. T.; Zeytunyan, A.; Fast, A. S.; Ladani, F. T.; Alfonso-Garcia, A.; Banik, M.; Yampolsky, S.; Fishman, D. A.; Potma, E. O.; Apkarian, V. A., Ultrafast Coherent Raman Scattering at Plasmonic Nanojunctions. *J. Phys. Chem. C* **2016,** *120* (37), 20943-20953.

(144) Yampolsky, S.; Fishman, D. A.; Dey, S.; Hulkko, E.; Banik, M.; Potma, E. O.; Apkarian, V. A., Seeing a Single Molecule Vibrate through Time-Resolved Coherent Anti-Stokes Raman Scattering. *Nat. Photonics* **2014,** *8* (8), 650-656.

(145) Keller, E. L.; Brandt, N. C.; Cassabaum, A. A.; Frontiera, R. R., Ultrafast Surface-Enhanced Raman Spectroscopy. *Analyst* **2015,** *140* (15), 4922-4931.

(146) Gruenke, N. L.; Cardinal, M. F.; McAnally, M. O.; Frontiera, R. R.; Schatz, G. C.; Van Duyne, R. P., Ultrafast and Nonlinear Surface-Enhanced Raman Spectroscopy. *Chem. Soc. Rev.* **2016,** *45* (8), 2263-2290.

(147) Frontiera, R. R.; Gruenke, N. L.; Van Duyne, R. P., Fano-Like Resonances Arising from Long-Lived Molecule-Plasmon Interactions in Colloidal Nanoantennas. *Nano Lett.* **2012,** *12* (11), 5989-5994.

(148) Ding, S. Y.; You, E. M.; Tian, Z. Q.; Moskovits, M., Electromagnetic Theories of Surface-Enhanced Raman Spectroscopy. *Chem. Soc. Rev.* **2017,** *46* (13), 4042-4076.

(149) Frontiera, R. R.; Henry, A. I.; Gruenke, N. L.; Van Duyne, R. P., Surface-Enhanced Femtosecond Stimulated Raman Spectroscopy. *J. Phys. Chem. Lett.* **2011,** *2* (10), 1199-1203.

(150) Mandal, A.; Erramilli, S.; Ziegler, L. D., Origin of Dispersive Line Shapes in Plasmonically Enhanced Femtosecond Stimulated Raman Spectra. *J. Phys. Chem. C* **2016,** *120* (37), 20998-21006.

(151) McAnally, M. O.; McMahon, J. M.; Van Duyne, R. P.; Schatz, G. C., Coupled Wave Equations Theory of Surface-Enhanced Femtosecond Stimulated Raman Scattering. *J. Chem. Phys.* **2016,** *145* (9), 094106.

(152) Itoh, T.; Yamamoto, Y. S., Recent Topics on Single-Molecule Fluctuation Analysis using Blinking in Surface-Enhanced Resonance Raman Scattering: Clarification by the Electromagnetic Mechanism. *Analyst* **2016,** *141* (17), 5000-5009.

(153) Lombardi, J. R.; Birke, R. L.; Haran, G., Single Molecule SERS Spectral Blinking and Vibronic Coupling. *J. Phys. Chem. C* **2011,** *115* (11), 4540-4545.

(154) Berera, R.; van Grondelle, R.; Kennis, J. T., Ultrafast Transient Absorption Spectroscopy: Principles and Application to Photosynthetic Systems. *Photosynth. Res.* **2009,** *101* (2-3), 105-118.

(155) Ruckebusch, C.; Sliwa, M.; Pernot, P.; de Juan, A.; Tauler, R., Comprehensive Data Analysis of Femtosecond Transient Absorption Spectra: A Review. *J. Photoch. Photobio. C* **2012,** *13* (1), 1-27.

(156) Furube, A.; Hashimoto, S., Insight into Plasmonic Hot-Electron Transfer and Plasmon Molecular Drive: New Dimensions in Energy Conversion and Nanofabrication. *NPG Asia Mater.* **2017,** *9* (12), e454-e454.

(157) Jiang, R.; Li, B.; Fang, C.; Wang, J., Metal/Semiconductor Hybrid Nanostructures for Plasmon-Enhanced Applications. *Adv. Mater.* **2014,** *26* (31), 5274-5309.

(158) Wu, K.; Chen, J.; McBride, J. R.; Lian, T., Efficient Hot-Electron Transfer by a Plasmon-Induced Interfacial Charge-Transfer Transition. *Science* **2015,** *349* (6248), 632-635.

(159) Li, J.; Cushing, S. K.; Zheng, P.; Meng, F.; Chu, D.; Wu, N., Plasmon-Induced Photonic and Energy-Transfer Enhancement of Solar Water Splitting by a Hematite Nanorod Array. *Nat. Commun.* **2013,** *4,* 2651.

(160) Cushing, S. K.; Li, J.; Bright, J.; Yost, B. T.; Zheng, P.; Bristow, A. D.; Wu, N., Controlling Plasmon-Induced Resonance Energy Transfer and Hot Electron Injection Processes in Metal@TiO_2 Core–Shell Nanoparticles. *J. Phys. Chem. C* **2015,** *119* (28), 16239-16244.

(161) Yu, Y.; Sundaresan, V.; Willets, K. A., Hot Carriers versus Thermal Effects: Resolving the Enhancement Mechanisms for Plasmon-Mediated Photoelectrochemical Reactions. *J. Phys. Chem. C* **2018,** *122* (9), 5040-5048.

(162) Yu, Y.; Williams, J. D.; Willets, K. A., Quantifying Photothermal Heating at Plasmonic Nanoparticles by Scanning Electrochemical Microscopy. *Faraday Discuss.* **2018,** *210* (0), 29-39.

(163) Bard, A. J., *Electrochemical Methods : Fundamentals and Applications*. Wiley: New York, 1980.

(164) Chirea, M.; Collins, S. S.; Wei, X.; Mulvaney, P., Spectroelectrochemistry of Silver Deposition on Single Gold Nanocrystals. *J. Phys. Chem. Lett.* **2014,** *5* (24), 4331-4335.

(165) Hoener, B. S.; Zhang, H.; Heiderscheit, T. S.; Kirchner, S. R.; De Silva Indrasekara, A. S.; Baiyasi, R.; Cai, Y.; Nordlander, P.; Link, S.; Landes, C. F.; Chang, W. S., Spectral Response of Plasmonic Gold Nanoparticles to Capacitive Charging: Morphology Effects. *J. Phys. Chem. Lett.* **2017,** *8* (12), 2681-2688.

(166) Novo, C.; Funston, A. M.; Gooding, A. K.; Mulvaney, P., Electrochemical Charging of Single Gold Nanorods. *J. Am. Chem. Soc.* **2009,** *131* (41), 14664-14666.

(167) Brown, A. M.; Sheldon, M. T.; Atwater, H. A., Electrochemical Tuning of the Dielectric Function of Au Nanoparticles. *ACS Photonics* **2015,** *2* (4), 459-464.

(168) Byers, C. P.; Hoener, B. S.; Chang, W. S.; Yorulmaz, M.; Link, S.; Landes, C. F., Single-Particle Spectroscopy Reveals Heterogeneity in Electrochemical Tuning of the Localized Surface Plasmon. *J. Phys. Chem. B* **2014,** *118* (49), 14047-14055.

(169) Collins, S. S.; Wei, X.; McKenzie, T. G.; Funston, A. M.; Mulvaney, P., Single Gold Nanorod Charge Modulation in an Ion Gel Device. *Nano Lett.* **2016,** *16* (11), 6863-6869.

(170) Hoener, B. S.; Byers, C. P.; Heiderscheit, T. S.; De Silva Indrasekara, A. S.; Hoggard, A.; Chang, W.-S.; Link, S.; Landes, C. F., Spectroelectrochemistry of Halide Anion Adsorption and Dissolution of Single Gold Nanorods. *J. Phys. Chem. C* **2016,** *120* (37), 20604-20612.

(171) Ingram, D. B.; Linic, S., Water Splitting on Composite Plasmonic-Metal/Semiconductor Photoelectrodes: Evidence for Selective Plasmon-Induced Formation of Charge Carriers Near the Semiconductor Surface. *J. Am. Chem. Soc.* **2011,** *133* (14), 5202-5205.

(172) Robatjazi, H.; Bahauddin, S. M.; Doiron, C.; Thomann, I., Direct Plasmon-Driven Photoelectrocatalysis. *Nano Lett.* **2015,** *15* (9), 6155-6161.

(173) Thomann, I.; Pinaud, B. A.; Chen, Z.; Clemens, B. M.; Jaramillo, T. F.; Brongersma, M. L., Plasmon Enhanced Solar-to-Fuel Energy Conversion. *Nano Lett.* **2011,** *11* (8), 3440-3446.

(174) Zheng, J.; Lu, T.; Cotton, T. M.; Chumanov, G., Photoinduced Electrochemical Reduction of Nitrite at an Electrochemically Roughened Silver Surface. *J. Phys. Chem. B* **1999,** *103* (31), 6567-6572.

(175) Wilson, A. J.; Molina, N. Y.; Willets, K. A., Modification of the Electrochemical Properties of Nile Blue through Covalent Attachment to Gold As Revealed by Electrochemistry and SERS. *J. Phys. Chem. C* **2016,** *120* (37), 21091-21098.

(176) Zaleski, S.; Wilson, A. J.; Mattei, M.; Chen, X.; Goubert, G.; Cardinal, M. F.; Willets, K. A.; Van Duyne, R. P., Investigating Nanoscale Electrochemistry with Surface- and Tip-Enhanced Raman Spectroscopy. *Acc. Chem. Res.* **2016,** *49* (9), 2023-2030.

(177) Kurouski, D.; Mattei, M.; Van Duyne, R. P., Probing Redox Reactions at the Nanoscale with Electrochemical Tip-Enhanced Raman Spectroscopy. *Nano Lett.* **2015,** *15* (12), 7956-7962.

(178) Marbella, L. E.; Millstone, J. E., NMR Techniques for Noble Metal Nanoparticles. *Chem. Mater.* **2015,** *27* (8), 2721-2739.

(179) Liu, J. G.; Zhang, H.; Link, S.; Nordlander, P., Relaxation of Plasmon-Induced Hot Carriers. *ACS Photonics* **2017,** *5* (7), 2584-2595.

(180) Libisch, F.; Cheng, J.; Carter, E. A., Electron-Transfer-Induced Dissociation of H_2 on Gold Nanoparticles: Excited-State Potential Energy Surfaces via Embedded Correlated Wavefunction Theory. *Z. Phys. Chem.* **2013,** *227* (9-11), 1455.

(181) Martirez, J. M.; Carter, E. A., Excited-State N_2 Dissociation Pathway on Fe-Functionalized Au. *J. Am. Chem. Soc.* **2017,** *139* (12), 4390-4398.

(182) Martirez, J. M. P.; Carter, E. A., Prediction of a Low-Temperature N_2 Dissociation Catalyst Exploiting Near-IR-to-Visible Light Nanoplasmonics. *Sci. Adv.* **2017,** *3* (12), eaao4710.

(183) Chulhai, D. V.; Hu, Z.; Moore, J. E.; Chen, X.; Jensen, L., Theory of Linear and Nonlinear Surface-Enhanced Vibrational Spectroscopies. *Annu. Rev. Phys. Chem.* **2016,** *67* (1), 541-564.

(184) Hu, Z.; Chulhai, D. V.; Jensen, L., Simulating Surface-Enhanced Hyper-Raman Scattering Using Atomistic Electrodynamics-Quantum Mechanical Models. *J. Chem. Theory Comput.* **2016,** *12* (12), 5968-5978.

(185) Litz, J. P.; Brewster, R. P.; Lee, A. B.; Masiello, D. J., Molecular–Electronic Structure in a Plasmonic Environment: Elucidating the Quantum Image Interaction. *J. Phys. Chem. C* **2013,** *117* (23), 12249-12257.

(186) Neuman, T.; Esteban, R.; Casanova, D.; Garcia-Vidal, F. J.; Aizpurua, J., Coupling of Molecular Emitters and Plasmonic Cavities beyond the Point-Dipole Approximation. *Nano Lett.* **2018,** *18* (4), 2358-2364.

(187) Ben-Nun, M.; Quenneville, J.; Martínez, T. J., Ab Initio Multiple Spawning: Photochemistry from First Principles Quantum Molecular Dynamics. *J. Phys. Chem. A* **2000,** *104* (22), 5161-5175.

(188) Moskovits, M., The Case for Plasmon-Derived Hot Carrier Devices. *Nat. Nanotechnol.* **2015,** *10* (1), 6-8.

(189) Hou, W.; Cronin, S. B., A Review of Surface Plasmon Resonance-Enhanced Photocatalysis. *Adv. Funct. Mater.* **2013,** *23* (13), 1612-1619.

(190) Wang, P.; Huang, B.; Dai, Y.; Whangbo, M. H., Plasmonic Photocatalysts: Harvesting Visible Light with Noble Metal Nanoparticles. *Phys. Chem. Chem. Phys.* **2012,** *14* (28), 9813-9825.

(191) Zhou, L.; Zhang, C.; McClain, M. J.; Manjavacas, A.; Krauter, C. M.; Tian, S.; Berg, F.; Everitt, H. O.; Carter, E. A.; Nordlander, P.; Halas, N. J., Aluminum Nanocrystals as a Plasmonic Photocatalyst for Hydrogen Dissociation. *Nano Lett.* **2016,** *16* (2), 1478-1484.

(192) Hou, W.; Hung, W. H.; Pavaskar, P.; Goeppert, A.; Aykol, M.; Cronin, S. B., Photocatalytic Conversion of CO_2 to Hydrocarbon Fuels via Plasmon-Enhanced Absorption and Metallic Interband Transitions. *ACS Catal.* **2011,** *1* (8), 929-936.

(193) Xie, W.; Schlucker, S., Hot Electron-Induced Reduction of Small Molecules on Photorecycling Metal Surfaces. *Nat. Commun.* **2015,** *6*, 7570.

(194) Qiu, J.; Wei, W. D., Surface Plasmon-Mediated Photothermal Chemistry. *J. Phys. Chem. C* **2014,** *118* (36), 20735-20749.

(195) Christopher, P.; Xin, H.; Marimuthu, A.; Linic, S., Singular Characteristics and Unique Chemical Bond Activation Mechanisms of Photocatalytic Reactions on Plasmonic Nanostructures. *Nat. Mater.* **2012,** *11* (12), 1044-1050.

(196) Moskovits, M., Persistent Misconceptions Regarding SERS. *Phys. Chem. Chem. Phys.* **2013,** *15* (15), 5301-5311.

(197) Valley, N.; Greeneltch, N.; Van Duyne, R. P.; Schatz, G. C., A Look at the Origin and Magnitude of the Chemical Contribution to the Enhancement Mechanism of Surface-Enhanced Raman Spectroscopy (SERS): Theory and Experiment. *J. Phys. Chem. Lett.* **2013,** *4* (16), 2599-2604.

(198) Stranahan, S. M.; Willets, K. A., Super-Resolution Optical Imaging of Single-Molecule SERS Hot Spots. *Nano Lett.* **2010,** *10* (9), 3777-3784.

(199) Laor, U.; Schatz, G. C., The Role of Surface Roughness in Surface-Enhanced Raman Spectroscopy (SERS): The Importance of Multiple Plasmon Resonances. *Chem. Phys. Lett.* **1981,** *82* (3), 566-570.

(200) Haynes, C. L.; Van Duyne, R. P., Nanosphere Lithography: A Versatile Nanofabrication Tool for Studies of Size-Dependent Nanoparticle Optics. *J. Phys. Chem. B* **2001,** *105* (24), 5599-5611.

(201) Greeneltch, N. G.; Blaber, M. G.; Henry, A. I.; Schatz, G. C.; Van Duyne, R. P., Immobilized Nanorod Assemblies: Fabrication and Understanding of Large Area Surface-Enhanced Raman Spectroscopy Substrates. *Anal. Chem.* **2013,** *85* (4), 2297-2303.

(202) Zhang, Q.; Wang, H., Facet-Dependent Catalytic Activities of Au Nanoparticles Enclosed by High-Index Facets. *ACS Catal.* **2014,** *4* (11), 4027-4033.

(203) Kim, K.; Kim, K. L.; Shin, K. S., Photoreduction of 4,4'-Dimercaptoazobenzene on Ag Revealed by Raman Scattering Spectroscopy. *Langmuir* **2013,** *29* (1), 183-190.

(204) Wan, L.-J.; Terashima, M.; Noda, H.; Osawa, M., Molecular Orientation and Ordered Structure of Benzenethiol Adsorbed on Gold(111). *J. Phys. Chem. B* **2000,** *104* (15), 3563-3569.

(205) Skadtchenko, B. O.; Aroca, R., Surface-Enhanced Raman Scattering of *p*-Nitrothiophenol Molecular Vibrations of its Silver Salt and the Surface Complex Formed on Silver Islands and Colloids. *Spectrochim. Acta A* **2001,** *57A* (5), 1009-1016.

(206) McCreery, R. L., *Raman Spectroscopy for Chemical Analysis*. John Wiley and Sons, Inc: 2000.

(207) Kim, K.; Shin, D.; Kim, K. L.; Shin, K. S., Surface-Enhanced Raman Scattering of 4,4'-Dimercaptoazobenzene Trapped in Au Nanogaps. *Phys. Chem. Chem. Phys.* **2012,** *14* (12), 4095-4100.

(208) Zhao, L.-B.; Chen, J.-L.; Zhang, M.; Wu, D.-Y.; Tian, Z.-Q., Theoretical Study on Electroreduction of p-Nitrothiophenol on Silver and Gold Electrode Surfaces. *J. Phys. Chem. C* **2015,** *119* (9), 4949-4958.

(209) Xu, P.; Kang, L.; Mack, N. H.; Schanze, K. S.; Han, X.; Wang, H. L., Mechanistic Understanding of Surface Plasmon Assisted Catalysis on a Single Particle: Cyclic Redox of 4-Aminothiophenol. *Sci. Rep.* **2013,** *3*, 2997.

(210) Kang, L.; Han, X.; Chu, J.; Xiong, J.; He, X.; Wang, H. L.; Xu, P., In Situ Surface-Enhanced Raman Spectroscopy Study of Plasmon-Driven Catalytic Reactions of 4-Nitrothiophenol under a Controlled Atmosphere. *ChemCatChem* **2015,** *7* (6), 1004-1010.

(211) Wastl, D. S.; Weymouth, A. J.; Giessibl, F. J., Optimizing Atomic Resolution of Force Microscopy in Ambient Conditions. *Phys. Rev. B: Condens. Matter* **2013,** *87* (24), 245415.

(212) Shin, H.-H.; Koo, J.-J.; Lee, K. S.; Kim, Z. H., Chemical Reactions Driven by Plasmon-Induced Hot Carriers. *Appl. Mater. Today* **2019,** *16*, 112-119.

(213) Zhan, C.; Chen, X.-J.; Yi, J.; Li, J.-F.; Wu, D.-Y.; Tian, Z.-Q., From Plasmon-Enhanced Molecular Spectroscopy to Plasmon-Mediated Chemical Reactions. *Nat. Rev. Chem.* **2018,** *2* (9), 216-230.

(214) Mohammadparast, F.; Dadgar, A. P.; Tirumala, R. T. A.; Mohammad, S.; Topal, C. O.; Kalkan, A. K.; Andiappan, M., C–C Coupling Reactions Catalyzed by Gold Nanoparticles: Evidence for Substrate-Mediated Leaching of Surface Atoms Using Localized Surface Plasmon Resonance Spectroscopy. *J. Phys. Chem. C* **2019,** *123* (18), 11539-11545.

(215) Coppens, Z. J.; Li, W.; Walker, D. G.; Valentine, J. G., Probing and Controlling Photothermal Heat Generation in Plasmonic Nanostructures. *Nano Lett.* **2013,** *13* (3), 1023-1028.

(216) Yan, L.; Wang, F.; Meng, S., Quantum Mode Selectivity of Plasmon-Induced Water Splitting on Gold Nanoparticles. *ACS Nano* **2016,** *10* (5), 5452-5458.

(217) Sandoval, J. J.; Palma, P.; Alvarez, E.; Rodriguez-Delgado, A.; Campora, J., Dibenzyl and Diallyl 2,6-Bisiminopyridinezinc(II) Complexes: Selective Alkyl Migration to the Pyridine Ring Leads to Remarkably Stable Dihydropyridinates. *Chem. Comm. (Camb.)* **2013,** *49* (60), 6791-6793.

(218) Lanni, E. L.; Bosscher, M. A.; Ooms, B. D.; Shandro, C. A.; Ellsworth, B. A.; Anderson, C. E., Synthesis of Substituted N-Benzyl Pyridones via an O- to N-Alkyl Migration. *J. Org. Chem.* **2008,** *73* (16), 6425-6428.

(219) Takahashi, M.; Suzuki, H.; Moro-Oka, Y.; Ikawa, T., 1,3-O- to -C-Alkyl Migration of 1-Alkenyl Alkyl Acetals and Ketals Catalyzed by Boron Trifluoride. Selective Cross- and Regioselective Aldol Type Reactions. *Tetrahedron Lett.* **1982,** *23* (10), 1079-1082.

(220) Tasker, S. Z.; Bosscher, M. A.; Shandro, C. A.; Lanni, E. L.; Ryu, K. A.; Snapper, G. S.; Utter, J. M.; Ellsworth, B. A.; Anderson, C. E., Preparation of N-Alkyl 2-Pyridones via a Lithium Iodide Promoted O- to N-Alkyl Migration: Scope and Mechanism. *J. Org. Chem.* **2012,** *77* (18), 8220-8230.

(221) Barton, E. E.; Rampulla, D. M.; Bocarsly, A. B., Selective Solar-Driven Reduction of CO_2 to Methanol using a Catalyzed *p*-GaP Based Photoelectrochemical Cell. *J. Am. Chem. Soc.* **2008,** *130* (20), 6342-6344.

(222) Keith, J. A.; Carter, E. A., Theoretical Insights into Pyridinium-Based Photoelectrocatalytic Reduction of CO_2. *J. Am. Chem. Soc.* **2012,** *134* (18), 7580-7583.

(223) Ertem, M. Z.; Konezny, S. J.; Araujo, C. M.; Batista, V. S., Functional Role of Pyridinium during Aqueous Electrochemical Reduction of CO_2 on Pt(111). *J. Phys. Chem. Lett.* **2013,** *4* (5), 745-748.

(224) Farcau, C.; Astilean, S., Mapping the SERS Efficiency and Hot-Spots Localization on Gold Film over Nanospheres Substrates. *J. Phys. Chem. C* **2010,** *114* (27), 11717-11722.

(225) Tesema, T. E.; Kafle, B.; Tadesse, M. G.; Habteyes, T. G., Plasmon-Enhanced Resonant Excitation and Demethylation of Methylene Blue. *J. Phys. Chem. C* **2017,** *121* (13), 7421-7428.

(226) Zong, Y.; Guo, Q.; Xu, M.; Yuan, Y.; Gu, R.; Yao, J., Plasmon-Induced Decarboxylation of Mercaptobenzoic Acid on Nanoparticle Film Monitored by Surface-Enhanced Raman Spectroscopy. *RSC Adv.* **2014,** *4* (60), 31810-31816.

(227) Chulhai, D. V.; Chen, X.; Jensen, L., Simulating Ensemble-Averaged Surface-Enhanced Raman Scattering. *J. Phys. Chem. C* **2016,** *120* (37), 20833-20842.

(228) Chulhai, D. V.; Jensen, L., Determining Molecular Orientation With Surface-Enhanced Raman Scattering Using Inhomogenous Electric Fields. *J. Phys. Chem. C* **2013,** *117* (38), 19622-19631.

(229) Fonseca Guerra, C.; Snijders, J. G.; te Velde, G.; Baerends, E. J., Towards an Order-N DFT Method. *Theor. Chem. Acc.* **1998,** *99* (6), 391-403.

(230) te Velde, G.; Bickelhaupt, F. M.; Baerends, E. J.; Fonseca Guerra, C.; van Gisbergen, S. J. A.; Snijders, J. G.; Ziegler, T., Chemistry with ADF. *J. Comput. Chem.* **2001,** *22* (9), 931-967.

(231) Becke, A. D., Density-Functional Exchange-Energy Approximation with Correct Asymptotic Behavior. *Phys. Rev. A: At. Mol. Opt. Phys.* **1988,** *38* (6), 3098-3100.

(232) Perdew, J. P., Density-Functional Approximation for the Correlation Energy of the Inhomogeneous Electron Gas. *Phys. Rev. B: Condens. Matter* **1986,** *33* (12), 8822-8824.

(233) Bunding, K. A.; Bell, M. I.; Durst, R. A., The Surface-Enhanced Raman Spectrum of N-Methylpyridinium Ion on a Silver Electrode. *Chem. Phys. Lett.* **1982,** *89* (1), 54-58.

(234) Szczerbiński, J.; Gyr, L.; Kaeslin, J.; Zenobi, R., Plasmon-Driven Photocatalysis Leads to Products Known from E-Beam and X-Ray-Induced Surface Chemistry. *Nano Lett.* **2018,** *18* (11), 6740-6749.

(235) Zoltewicz, J. A.; Kauffman, G. M.; Smith, C. L., Mechanism of Base-Catalyzed Hydrogen Exchange for N-Methylpyridinium Ion and Pyridine N-Oxide Relative Positional Rates. *J. Am. Chem. Soc.* **1968,** *90* (21), 5939-5940.

(236) Gaudiello, J. G.; Larkin, D.; Rawn, J. D.; Sosnowski, J. J.; Bancroft, E. E.; Blount, H. N., On the Mechanism of the Electrochemical Reduction of N-Methylpyridinium Ion. *J. Electroanal. Chem.* **1982,** *131* (Jan), 203-214.

(237) Ladenburg, *Justus Liebigs Annalen der Chemie* **1888,** *247*, 17.

(238) Lange, *Chem. Ber.* **1885,** *18*, 3439.

(239) Cardini, G.; Muniz-Miranda, M.; Schettino, V., SERS and DFT Study on 4-Methylpyridine Adsorbed on Silver Colloids and Electrodes. *J. Phys. Chem. B* **2004,** *108* (44), 17007-17011.

(240) Sato, H.; Kawasaki, M.; Kasatani, K.; Kawai, E.; Suzuki, H., Competitive Adsorption of 2- and 4-Methylpyridine and Pyridine on a Polycrystalline Ag Electrode as Studied by SERS. *Chem. Phys. Lett.* **1986,** *123* (4), 355-358.

(241) Haynes, C. L.; McFarland, A. D.; Van Duyne, R. P., Surface-Enhanced Raman Spectroscopy. *Anal. Chem.* **2005,** *77* (17), 338 A-346 A.

(242) Tesema, T. E.; Annesley, C.; Habteyes, T. G., Plasmon-Enhanced Autocatalytic N-Demethylation. *J. Phys. Chem. C* **2018,** *122* (34), 19831-19841.

(243) Bird, C. L.; Kuhn, A. T., Electrochemistry of the Viologens. *Chem. Soc. Rev.* **1981,** *10* (1), 49-82.

(244) Gemborys, H. A.; Shaw, B. R., Electrochemical Behavior of Methyl Viologen in Zeolite Particle Films. *J. Electroanal. Chem.* **1986,** *208* (1), 95-107.

(245) Ward, M. D.; White, J. R.; Bard, A. J., Electrochemical Investigation of the energetics of Particulate Titanium Dioxide Photocatalysts. The Methyl Viologen-Acetate System. *J. Am. Chem. Soc.* **1983,** *105* (1), 27-31.

(246) Morris-Cohen, A. J.; Frederick, M. T.; Cass, L. C.; Weiss, E. A., Simultaneous Determination of the Adsorption Constant and the Photoinduced Electron Transfer Rate for a CdS Quantum Dot–Viologen Complex. *J. Am. Chem. Soc.* **2011,** *133* (26), 10146-10154.

(247) Michaelis, L.; Hill, E. S., The Viologen Indicators. *J. Gen. Physiol.* **1933,** *16* (6), 859-873.

(248) Feilchenfeld, H.; Chumanov, G.; Cotton, T. M., Photoreduction of Methylviologen Adsorbed on Silver. *J. Phys. Chem.* **1996,** *100* (12), 4937-4943.

(249) Chen, S.-H.; Ren, X.-M., SERS Studies of Methyl Viologen on Silver Sol and the Effect of Halide Ions. *Spectrochim. Acta A* **1995,** *51* (4), 717-725.

(250) Dick, L. A.; McFarland, A. D.; Haynes, C. L.; Van Duyne, R. P., Metal Film Over Nanosphere (MFON) Electrodes for Surface-Enhanced Raman Spectroscopy (SERS): Improvements in Surface Nanostructure Stability and Suppression of Irreversible Loss. *J. Phys. Chem. B* **2002,** *106* (4), 853-860.

(251) Zhao, L.; Jensen, L.; Schatz, G. C., Pyridine− Ag20 Cluster: A Model System for Studying Surface-Enhanced Raman Scattering. *J. Am. Chem. Soc* **2006,** *128* (9), 2911-2919.

(252) Laury, M. L.; Carlson, M. J.; Wilson, A. K., Vibrational Frequency Scale Factors for Density Functional Theory and the Polarization Consistent Basis Sets. *J. Comput. Chem.* **2012,** *33* (30), 2380-2387.

(253) Janesko, B. G.; Scuseria, G. E., Surface Enhanced Raman Optical Activity of Molecules on Orientationally Averaged Substrates: Theory of Electromagnetic Effects. *J. Chem. Phys.* **2006,** *125* (12), 124704.

(254) Klamt, A.; Schüürmann, G., COSMO: A New Approach to Dielectric Screening in Solvents with Explicit Expressions for the Screening Energy and its Gradient. *J. Chem. Soc., Perkin Trans. 2* **1993,** (5), 799-805.

(255) Pye, C. C.; Ziegler, T., An Implementation of the conductor-like Screening Model of Solvation within the Amsterdam Density Functional Package. *Theor. Chem. Acc.* **1999,** *101* (6), 396-408.

(256) Feng, Q.; Yue, W.; Cotton, T. M., Surface-enhanced Resonance Raman Scattering from Methyl Viologen at a Silver Electrode: Evidence for Two Distinct Adsorption Interactions. *J. Phys. Chem.* **1990,** *94* (5), 2082-2091.

(257) Lu, T.; Birke, R. L.; Lombardi, J. R., Surface Raman Spectroscopy of the Three Redox Forms of Methylviologen. *Langmuir* **1986,** *2* (3), 305-309.

(258) Suzuki, M.; Niidome, Y.; Yamada, S., Adsorption Characteristics of 4,4′-Bipyridine Molecules on Gold Nanosphere Films Studied by Surface-Enhanced Raman Scattering. *Thin Solid Films* **2006,** *496* (2), 740-747.

(259) Huang, Y. F.; Zhang, M.; Zhao, L. B.; Feng, J. M.; Wu, D. Y.; Ren, B.; Tian, Z. Q., Activation of Oxygen on Gold and Silver Nanoparticles Assisted by Surface Plasmon Resonances. *Angew. Chem. Int. Ed.* **2014,** *53* (9), 2353-2357.

(260) Zhao, L.-B.; Liu, X.-X.; Zhang, M.; Liu, Z.-F.; Wu, D.-Y.; Tian, Z.-Q., Surface Plasmon Catalytic Aerobic Oxidation of Aromatic Amines in Metal/Molecule/Metal Junctions. *J. Phys. Chem. C* **2016,** *120* (2), 944-955.

(261) Hammond, G. S., A Correlation of Reaction Rates. *J. Am. Chem. Soc.* **1955,** *77* (2), 334-338.

(262) Frischkorn, C.; Wolf, M., Femtochemistry at Metal Surfaces: Nonadiabatic Reaction Dynamics. *Chem. Rev.* **2006,** *106* (10), 4207-4233.

(263) Robinson, H. H.; Yocum, C. F., Cyclic Photophosphorylation Reactions Catalyzed by Ferredoxin, Methyl Viologen and Anthraquinone Sulfonate. Use of Photochemical Reactions to Optimize Redox Poising. *Biochim. Biophys. Acta Bioenerg.* **1980,** *590* (1), 97-106.

(264) Watanabe, T.; Honda, K., Measurement of the Extinction Coefficient of the Methyl Viologen Cation Radical and the Efficiency of its Formation by Semiconductor Photocatalysis. *J. Phys. Chem.* **1982,** *86* (14), 2617-2619.

(265) Cai, Y. Y.; Liu, J. G.; Tauzin, L. J.; Huang, D.; Sung, E.; Zhang, H.; Joplin, A.; Chang, W. S.; Nordlander, P.; Link, S., Photoluminescence of Gold Nanorods: Purcell Effect Enhanced Emission from Hot Carriers. *ACS Nano* **2018,** *12* (2), 976-985.

(266) Cai, Y. Y.; Sung, E.; Zhang, R.; Tauzin, L. J.; Liu, J. G.; Ostovar, B.; Zhang, Y.; Chang, W. S.; Nordlander, P.; Link, S., Anti-Stokes Emission from Hot Carriers in Gold Nanorods. *Nano Lett.* **2019,** *19* (2), 1067-1073.

(267) Dey, S.; Banik, M.; Hulkko, E.; Rodriguez, K.; Apkarian, V. A.; Galperin, M.; Nitzan, A., Observation and Analysis of Fano-Like Lineshapes in the Raman Spectra of Molecules Adsorbed at Metal Interfaces. *Phys. Rev. B: Condens. Matter* **2016,** *93* (3), 035411.

(268) McGlashen, M. L.; Blackwood Jr, M. E.; Spiro, T. G., Resonance Raman Spectroelectrochemistry of the Fullerene C_{60} Radical Anion. *J. Am. Chem. Soc.* **1993,** *115* (5), 2074-2075.

(269) Andrew, P.; Barnes, W. L., Energy Transfer Across a Metal Film Mediated by Surface Plasmon Polaritons. *Science* **2004,** *306* (5698), 1002-1005.

(270) Hsu, L.-Y.; Ding, W.; Schatz, G. C., Plasmon-Coupled Resonance Energy Transfer. *J. Phys. Chem. Lett.* **2017,** *8* (10), 2357-2367.

(271) Sharma, B.; Frontiera, R. R.; Henry, A.-I.; Ringe, E.; Van Duyne, R. P., SERS: Materials, Applications, and the Future. *Mater. Today* **2012,** *15* (1-2), 16-25.

(272) Cheng, H.-E.; Wen, Y.-W., Correlation between Process Parameters, Microstructure and Hardness of Titanium Nitride Films by Chemical Vapor Deposition. *Surf. Coat. Technol.* **2004,** *179* (1), 103-109.

(273) Juneja, S.; Shishodia, M. S., Surface Plasmon Amplification in Refractory Transition Metal Nitrides Based Nanoparticle Dimers. *Opt. Commun.* **2019,** *433*, 89-96.

(274) Cheng, G.; Luo, J.; Qian, J.; Miao, J., Surface Modification of Nano-TiN by using Silane Coupling Agent. *Mater. Sci.-Poland* **2014,** *32* (2), 214-219.

Appendix A

Supporting Information for Manuscript:

Competition Between Reaction and Degradation in Plasmon-Driven Photochemistry

A.1 Estimation of SERS Enhancement Factors

The enhancement factors used in the figures were calculated by applying the following equation:[1]

$$EF = \frac{I_{SERS}/N_{surf}}{I_{NRS}/N_{vol}}$$

where I_{SERS} and I_{NRS} are the Raman intensity of 4-nitrobenzenethiol's (4-NBT) 1074 cm^{-1} shift recorded on the AuFON substrate and in solution, respectively. N_{surf} is the number of molecules adsorbed on the substrate and N_{vol} is the number of molecules in the sampled volume for the normal Raman collection. N_{surf} was calculated by using a focused laser spot size of 33 um^2, a surface coverage of 3.2 x 10^6 molecules/um^2 for 4-NBT molecules on gold,[2] and an estimated increased surface area factor of 2, which accounts for the hemispherical shape of the gold metal surface.

We were not able to obtain an off-resonant Raman signal for 4-NBT in water under our experimental conditions, in part due to its low solubility. Fortunately, a previous study estimated the differential Raman cross section for the 1074 cm^{-1} peak of 4-NBT with 785 nm excitation as 0.05 x 10^{-30} cm^2/sr.[3] We converted this differential cross section to an absolute cross section by multiplying by 4π steradians, to get a value of 0.63 x 10^{-30} cm^2. To account for the collection efficiency of our particular Raman system, we measured the Raman intensity of cyclohexane's 801 cm^{-1} stretching mode, which has an absolute Raman cross section value of 0.969 x 10^{-30} cm^2 for 785 nm excitation.[4] The measured cyclohexane spectral intensity was 825 counts/mW*s. Scaling by the absolute cross sections, we would anticipate that the intensity of the normal Raman signal of 4-NBT's 1074 cm^{-1} mode should be 5.78 x 10^{-3} counts/mW s, a value below our detection limits. The equivalent value for the nitro group stretch, the most intense peak in the spectrum, scaled by the relative intensity seen in SERS, is 9.60 x 10^{-3} counts/mW s. This value was used for I_{NRS} in equation 1.

A.2 Kinetic Traces

In addition to the three kinetic traces provided in **Figure 3.5**, we have provided the traces for all 26 studied photochemical reactions below (**Figures A1-A26**). Data analysis and fitting were performed as described in the main text of Chapter 3.

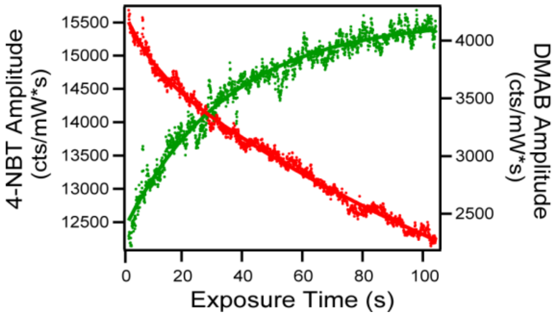

Figure A1. Reaction kinetics of the 4-NBT plasmon-induced photoreaction. The initial EF of this sampled region was 3.03 x 10^7.

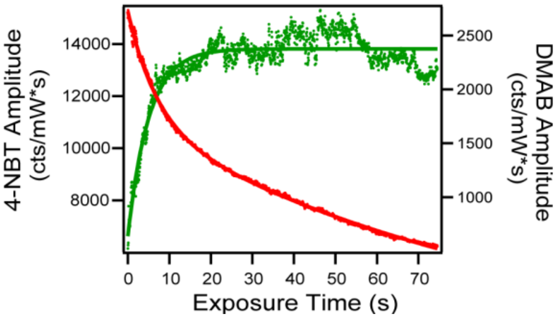

Figure A2. Reaction kinetics of the 4-NBT plasmon-induced photoreaction. The initial EF of this sampled region was 2.80 x 10^7.

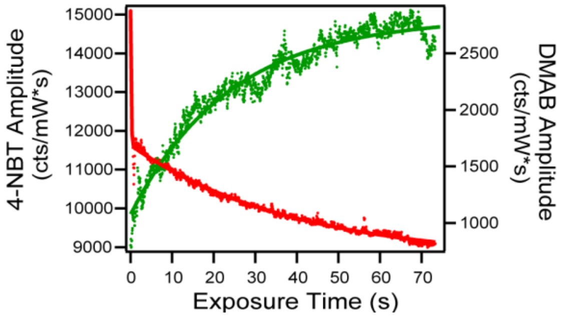

Figure A3. Reaction kinetics of the 4-NBT plasmon-induced photoreaction. The initial EF of this sampled region was 2.77 x 10^7.

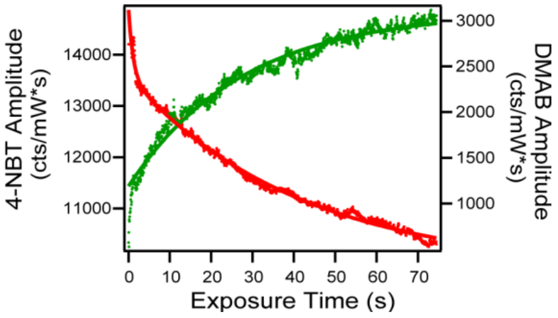

Figure A4. Reaction kinetics of the 4-NBT plasmon-induced photoreaction. The initial EF of this sampled region was 2.72 x 10^7.

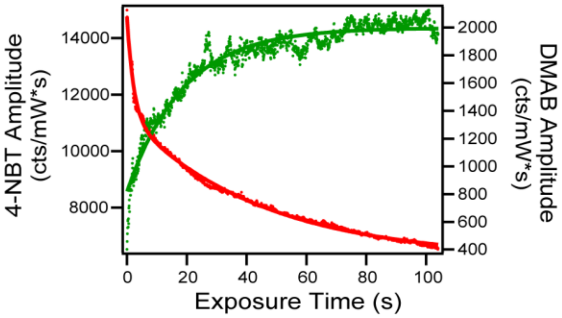

Figure A5. Reaction kinetics of the 4-NBT plasmon-induced photoreaction. The initial EF of this sampled region was 2.44 x 10^7.

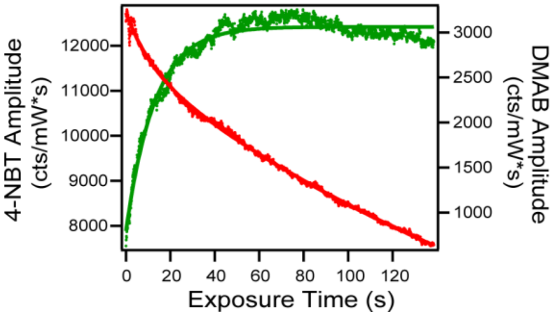

Figure A6. Reaction kinetics of the 4-NBT plasmon-induced photoreaction. The initial EF of this sampled region was 2.42 x 10^7.

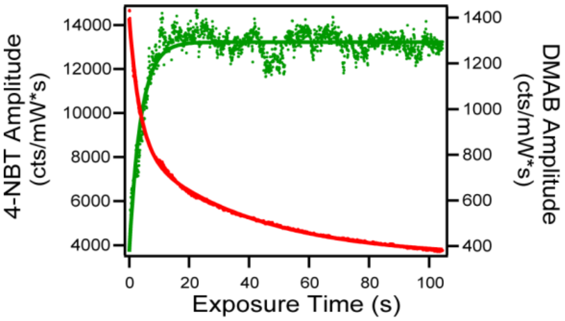

Figure A7. Reaction kinetics of the 4-NBT plasmon-induced photoreaction. The initial EF of this sampled region was 2.31 x 10^7.

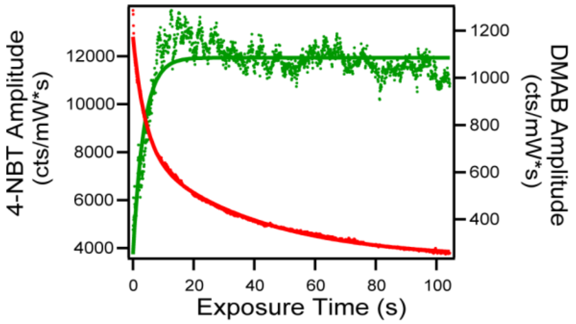

Figure A8. Reaction kinetics of the 4-NBT plasmon-induced photoreaction. The initial EF of this sampled region was 2.15 x 10^7.

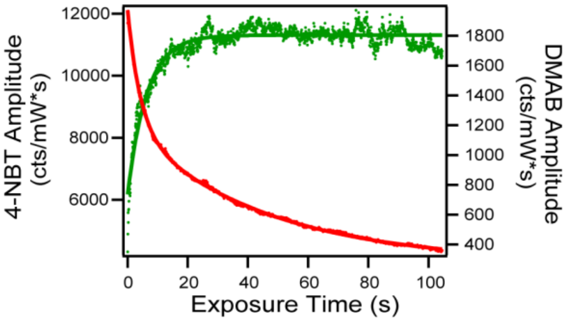

Figure A9. Reaction kinetics of the 4-NBT plasmon-induced photoreaction. The initial EF of this sampled region was 2.06 x 10^7.

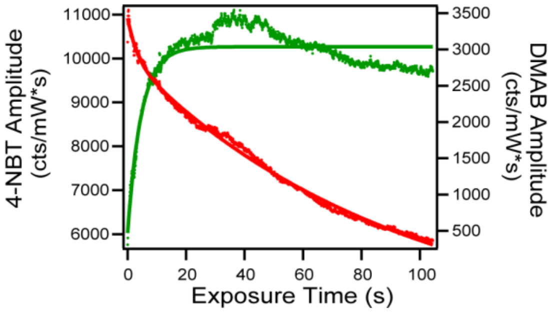

Figure A10. Reaction kinetics of the 4-NBT plasmon-induced photoreaction. The initial EF of this sampled region was 2.03 x 10^7.

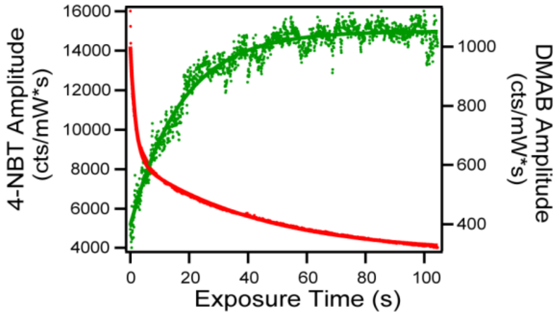

Figure A11. Reaction kinetics of the 4-NBT plasmon-induced photoreaction. The initial EF of this sampled region was 2.02 x 10^7.

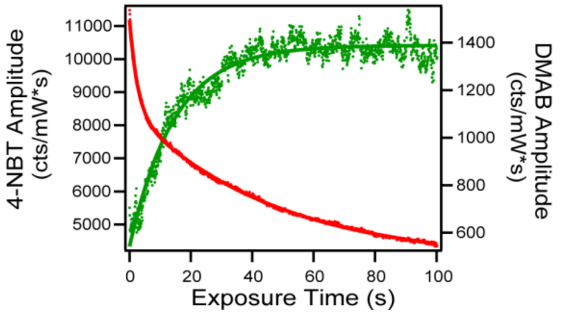

Figure A12. Reaction kinetics of the 4-NBT plasmon-induced photoreaction. The initial EF of this sampled region was 1.86 x 10^7.

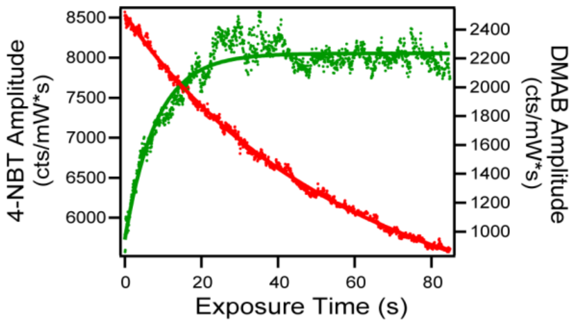

Figure A13. Reaction kinetics of the 4-NBT plasmon-induced photoreaction. The initial EF of this sampled region was 1.69 x 10^7.

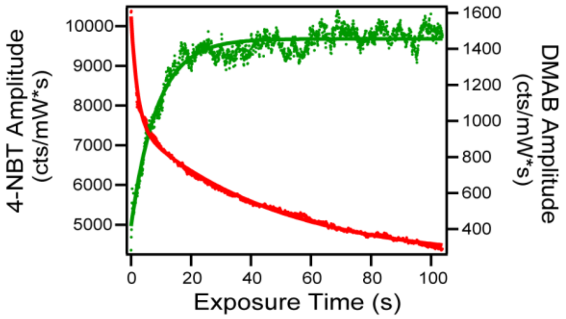

Figure A14. Reaction kinetics of the 4-NBT plasmon-induced photoreaction. The initial EF of this sampled region was 1.65 x 10^7.

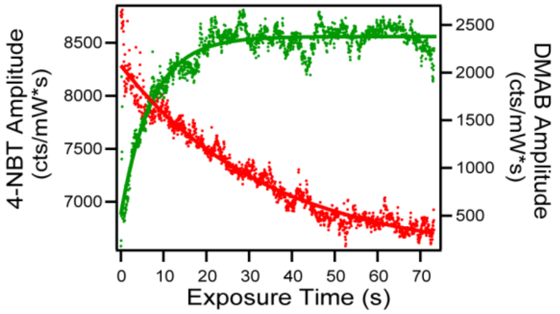

Figure A15. Reaction kinetics of the 4-NBT plasmon-induced photoreaction. The initial EF of this sampled region was 1.65 x 10^7.

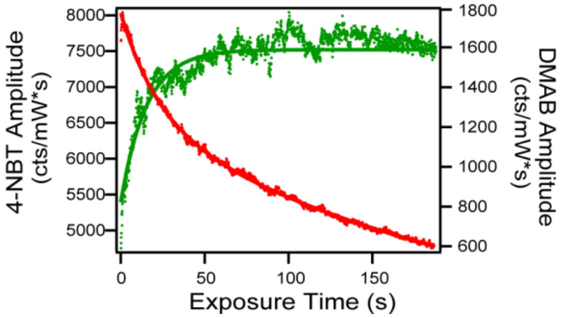

Figure A16. Reaction kinetics of the 4-NBT plasmon-induced photoreaction. The initial EF of this sampled region was 1.48 x 10^7.

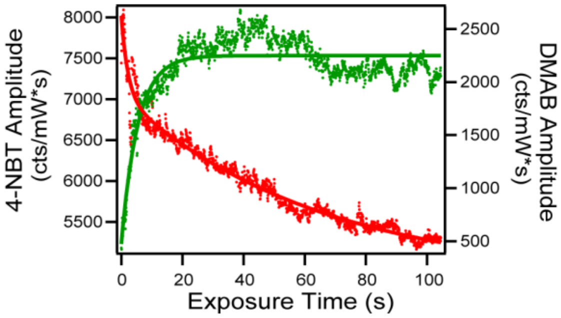

Figure A17. Reaction kinetics of the 4-NBT plasmon-induced photoreaction. The initial EF of this sampled region was 1.44 x 10^7.

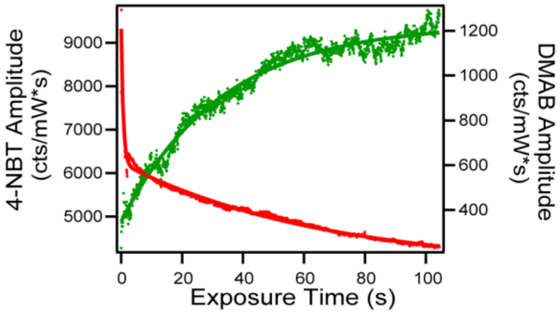

Figure A18. Reaction kinetics of the 4-NBT plasmon-induced photoreaction. The initial EF of this sampled region was 1.29 x 10^7.

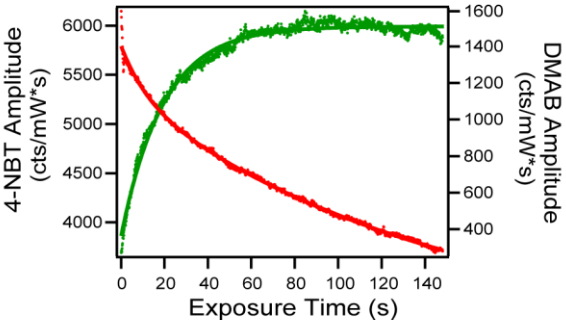

Figure A19. Reaction kinetics of the 4-NBT plasmon-induced photoreaction. The initial EF of this sampled region was 1.11 x 10^7.

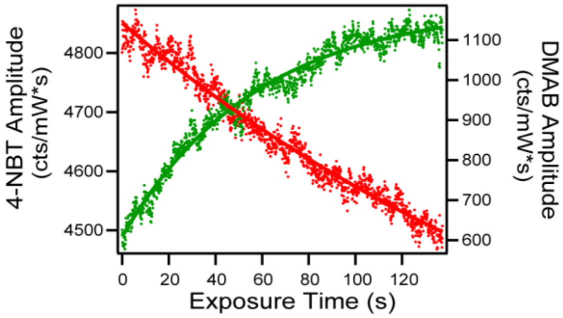

Figure A20. Reaction kinetics of the 4-NBT plasmon-induced photoreaction. The initial EF of this sampled region was 9.57 x 10^6.

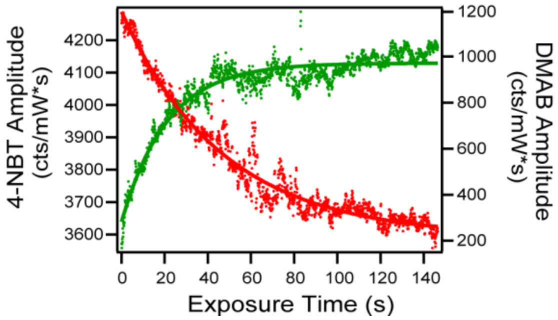

Figure A21. Reaction kinetics of the 4-NBT plasmon-induced photoreaction. The initial EF of this sampled region was 8.46 x 10^6.

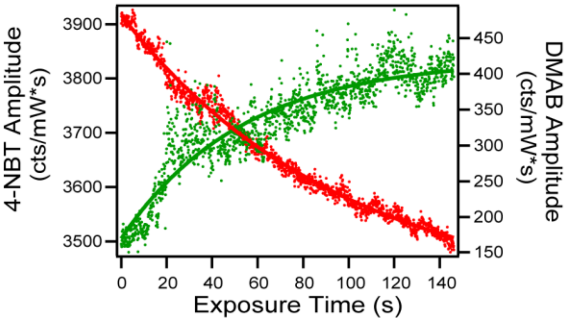

Figure A22. Reaction kinetics of the 4-NBT plasmon-induced photoreaction. The initial EF of this sampled region was 7.73 x 10^6.

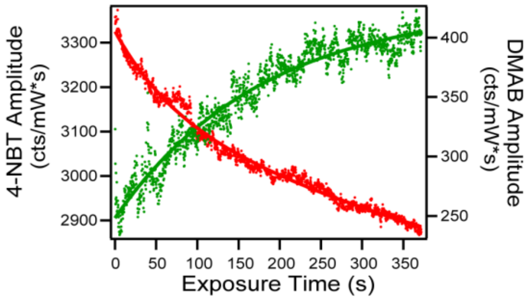

Figure A23. Reaction kinetics of the 4-NBT plasmon-induced photoreaction. The initial EF of this sampled region was 6.52 x 10^6.

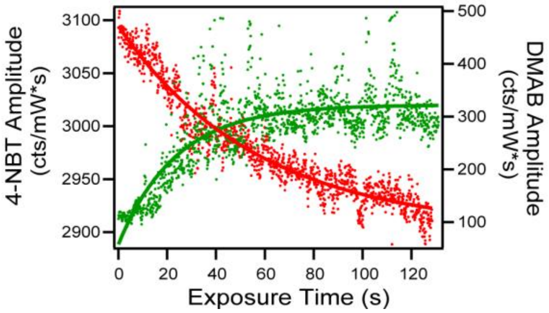

Figure A24. Reaction kinetics of the 4-NBT plasmon-induced photoreaction. The initial EF of this sampled region was 6.11 x 10^6.

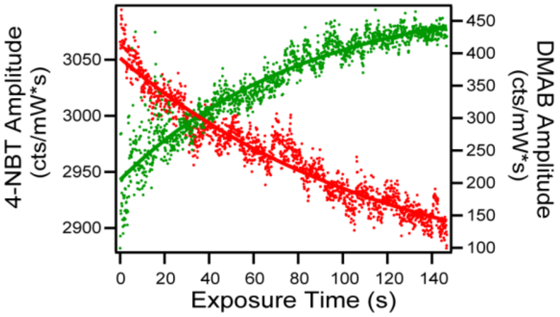

Figure A25. Reaction kinetics of the 4-NBT plasmon-induced photoreaction. The initial EF of this sampled region was 6.02 x 10^6.

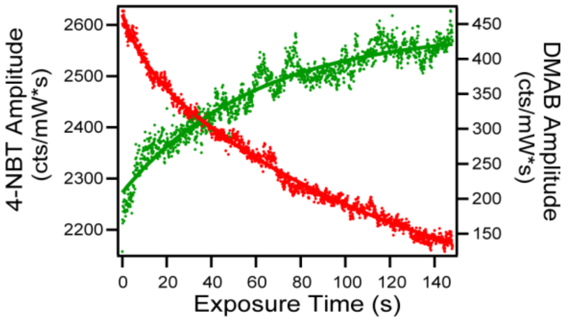

Figure A26. Reaction kinetics of the 4-NBT plasmon-induced photoreaction. The initial EF of this sampled region was 5.11 x 10^6.

A.3 References

(1) Kleinman, S. L.; Frontiera, R. R.; Henry, A. I.; Dieringer, J. A.; Van Duyne, R. P., Creating, Characterizing, and Controlling Chemistry with SERS Hot Spots. *Phys. Chem. Chem. Phys.* **2013,** *15* (1), 21-36.

(2) Wan, L.-J.; Terashima, M.; Noda, H.; Osawa, M., Molecular Orientation and Ordered Structure of Benzenethiol Adsorbed on Gold(111). *J. Phys. Chem. B* **2000,** *104* (15), 3563-3569.

(3) Valley, N.; Greeneltch, N.; Van Duyne, R. P.; Schatz, G. C., A Look at the Origin and Magnitude of the Chemical Contribution to the Enhancement Mechanism of Surface-Enhanced Raman Spectroscopy (SERS): Theory and Experiment. *J. Phys. Chem. Lett.* **2013,** *4* (16), 2599-2604.

(4) McCreery, R. L., *Raman Spectroscopy for Chemical Analysis*. John Wiley and Sons, Inc: 2000.

Appendix B

Supporting Information for Manuscript:

Plasmon-Mediated Intramolecular Methyl Migration

B.1 Estimation of Laser Spot Size and Molecular Packing Density

We calculated the laser spot size by performing a 90:10 razor-edge power study and determined the focused spot size to be 15.9 um^2. With this approximate value, we were able to convert our laser power measurements to a more easily comparable laser flux. Our original power measurements with a 785 nm continuous wave laser and their corresponding fluxes are 0.8, 2, and 5 mW and 5,000, 12,500, and 31,500 W/cm^2, respectively.

Additionally, we were able to generate an estimation of the number of NMP molecules we deposited onto the AuFON's surface. To do so, we used a molecular packing density for a similar heterocyclic amine (pyridine), which was 4.03 x 10^6 molecules / um^2 on a gold surface[1]. Also, we implemented an increased surface area factor of 2, which accounts for the hemispherical shape of the gold metal surface. The number of molecules that we deposited onto the AuFON substrates in our experiments was ~2.11 x 10^{15}. Our calculations also show that a theoretical monolayer coverage would require ~2.05 x 10^{15} molecules. Therefore, we conclude that our measurements were performed at a near-monolayer coverage, with an approximate 2% excess of molecules deposited on the substrate.

B.2 4-Methylpyridine Normal Mode Calculations

Figure B1 displays the normal mode calculations for the six 4-methylpyridine vibrational modes that we observed during the plasmon-mediated reaction. The observed experimental vibrational frequencies and their corresponding theoretical counterpart were

797, 1010, 1077, 1219, 1377, 1620 cm^{-1} and 802, 995, 1080, 1226, 1383, and 1609 cm^{-1}, respectively.

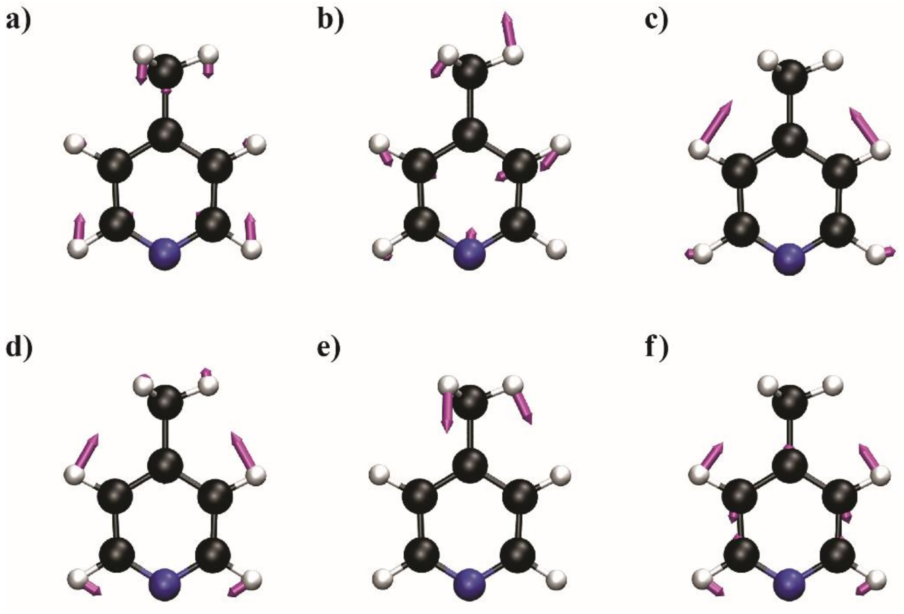

Figure B1. Normal mode calculations for 4-methylpyridine. The observed experimental and theoretical frequencies for these modes were (a) 797/802 cm^{-1}, (b) 1010/995 cm^{-1}, (c) 1077/1080 cm^{-1}, (d) 1219/1226 cm^{-1}, (e) 1377/1383 cm^{-1}, (f) 1620/1609 cm$^{-1.}$

B.3 NMP Kinetic Traces

Below, we have provided the kinetic traces for the 15 studied photochemical reactions of NMP adsorbed to the surface of AuFON substrates (**Figures B2-B4**). The five collections for each flux are displayed on the same plot. We fit all of the individual data sets to a single exponential function to determine the various trials' rates. As the fluxes increased, we noticed slight deviations away from single exponential fits. This is a phenomenon that we have previously observed[2] and we postulate it is due to a competing degradation pathway that is introduced at intense laser fluxes. A more detailed discussion pertaining to the distribution of the product's production and rate can be found in the main text.

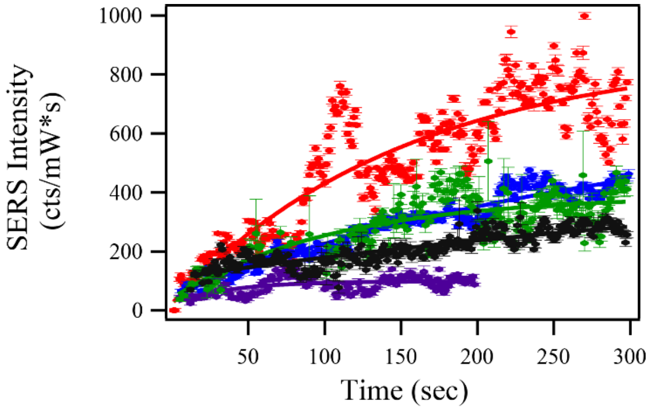

Figure B2. Reaction kinetics of the photoproduct's 1077 cm^{-1} mode during the 5,000 W/cm^2 flux experiments. The purple fit's truncated fit window is due to a dramatic collapse in the entire SER spectrum after 200 sec of laser exposure.

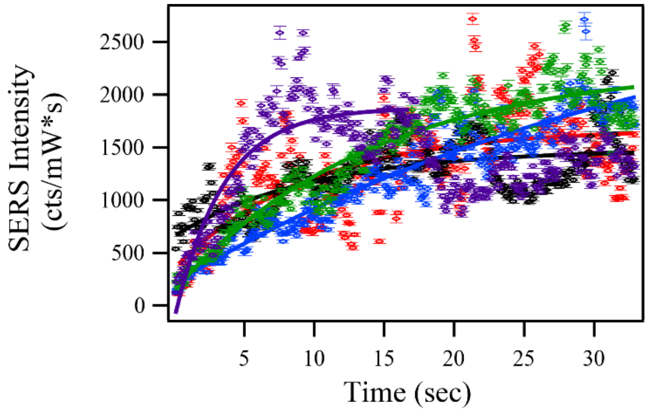

Figure B3. Reaction kinetics of the photoproduct's 1077 cm^{-1} mode during the 12,500 W/cm^2 flux experiments.

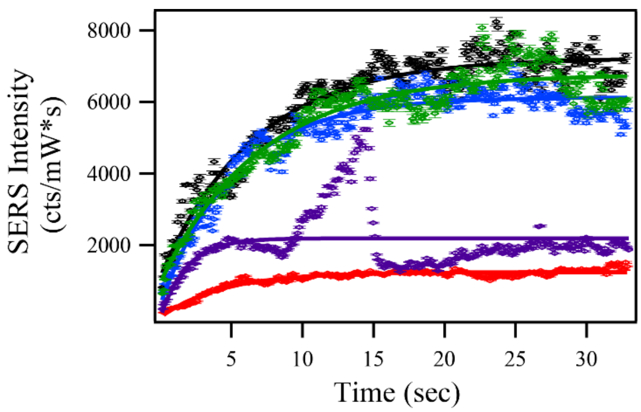

Figure B4. Reaction kinetics of the photoproduct's 1077 cm^{-1} mode during the 31,500 W/cm^2 flux experiments.

B.4 References

(1) Stolberg, L.; Morin, S.; Lipkowski, J.; Irish, D. E., Adsorption of Pyridine at the Au(111)-Solution Interface. *J. Electroanal. Chem.* **1991,** *307* (1-2), 241-262.

(2) Brooks, J. L.; Frontiera, R. R., Competition between Reaction and Degradation Pathways in Plasmon-Driven Photochemistry. *J. Phys. Chem. C* **2016,** *120* (37), 20869-20876.

Appendix C

Supporting Information for Manuscript:

Plasmon-Driven C-N Bond Cleavage Across a Series of Viologen Derivatives

C.1 Estimation of Spot Size and Molecular Packing Density

We estimated the focused laser's spot size by performing a 90:10 razor-edge power study and calculated the focused spot size to be 15.9 um^2. With this approximation, we were able to convert our laser power measurements to a standardized laser flux. Our original power measurements with a 785 nm laser and their corresponding fluxes are 0.8, 2, 5, and 10 mW and 5,000, 12,500, 31,500, and 62,900 W/cm^2, respectively.

Additionally, we were able to generate an estimation of the number of viologen molecules that we deposited onto the AuFON's surface. To do so, we estimated a molecular packing density for methyl viologen by multiplying a known value for pyridine by 2.[1] We calculated an estimated molecular packing density of ~1.11 x 10^5 molecules / um^2 on the gold surface. Also, we implemented an increased surface area factor of 2, which accounts for the hemispherical shape of the gold metal surface. The number of molecules that we deposited onto the AuFON substrates in our experiments was ~2.11 x 10^{15}. In addition, our calculations show that a theoretical monolayer coverage would require ~5.64 x 10^{13} molecules. In these studies, we had an abundance of viologen molecules on and near the surface, further ensuring that we had a fully saturated gold substrate for the SERS measurements.

C.2 4,4'-Bipyridine Normal Mode Calculations

Figure C1 displays the normal mode calculations for the six 4,4'-bipyridine vibrational modes that we observed during the plasmon-driven photoreaction. The observed experimental vibrational frequencies and their corresponding theoretical counterpart were 1020, 1070, 1224, 1294, 1512, 1608 cm^{-1} and 1002, 1096, 1245, 1283, 1513, and 1599 cm^{-1}, respectively.

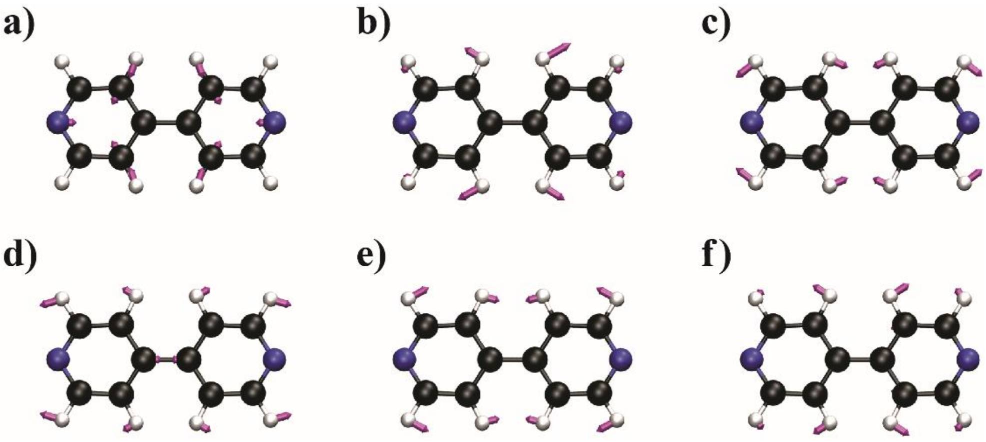

Figure C1. Normal mode calculations for 4,4-bipyridine. The observed experimental and theoretical frequencies for these modes were (a) 1020/1002 cm^{-1}, (b) 1070/1096 cm^{-1}, (c) 1224/1245 cm^{-1}, (d) 1294/1283 cm^{-1}, (e) 1512/1513 cm^{-1}, (f) 1608/1599 cm$^{-1.}$

C.3 Methyl Viologen Studies

In an attempt to accurately determine the true chemical identity of the methyl viologen plasmon-mediated photoproduct, we performed additional theoretical calculations on a series of logical photoproducts. **Figure C2** displays the calculated SER spectra of fully reduced methyl viologen (MV^0), 4,4'-bipyridine, single demethylated MV^+, and N-methylpyridinium. Unfortunately, we did not observe a strong overlap between the MV photoproduct vibrational signatures and the calculated SER spectra.

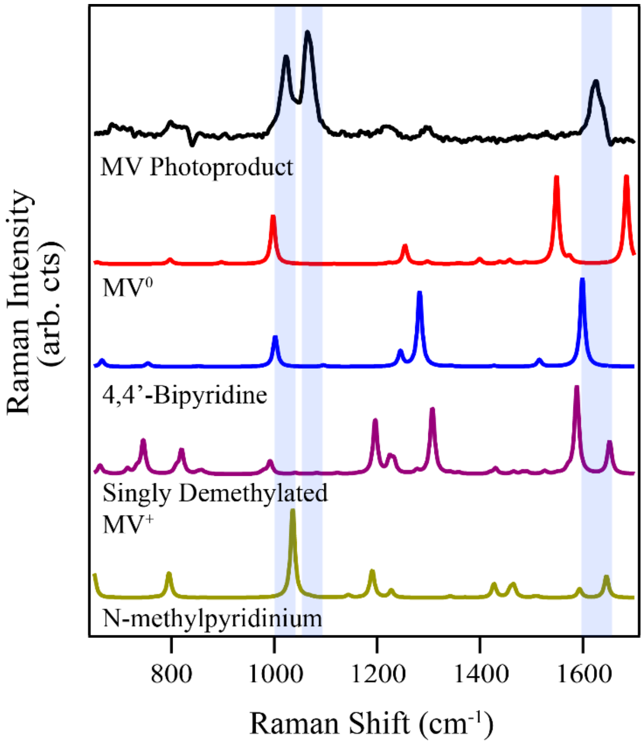

Figure C2. Spectral comparison of the MV photoproduct (black) and the calculated SER spectra of MV^0 (red), 4,4'-biypridine (blue), singly demethylated MV^+ (purple), and N-methylpyridinium (gold).

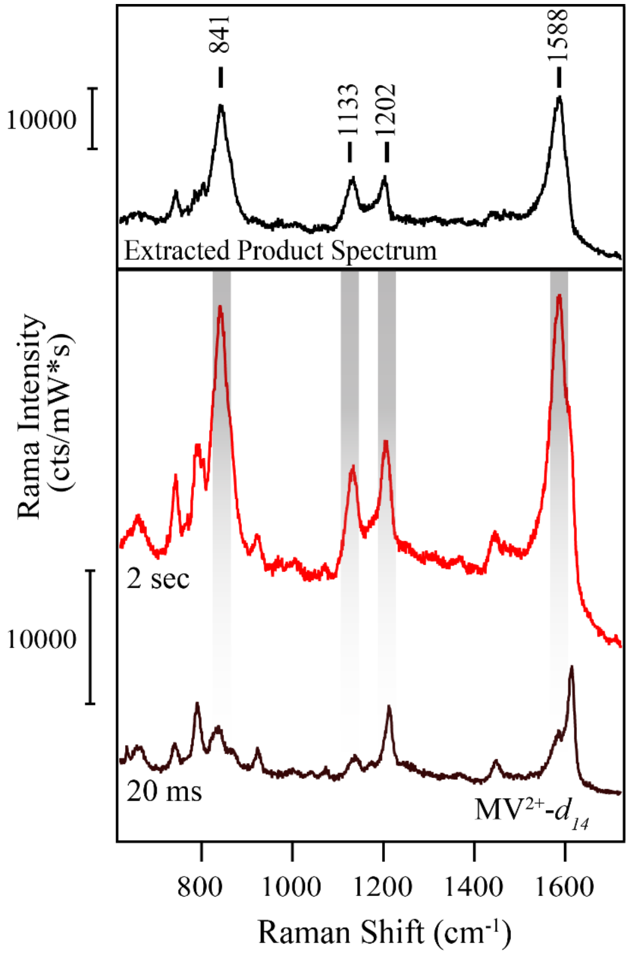

Figure C3. Time-dependent evolution of the SER spectra of MV-d_{14} on the surface of an AuFON substrate. As seen in the extract product spectrum, we observed the formation of four new Raman vibrational modes at 841, 1133, 1202, and 1588 cm^{-1}.

In addition to the theoretical calculations, we also performed SERS measurements on a fully-deuterated analog of methyl viologen (MV-d_{14}). **Figure C3** displays the time-dependent spectra of MV-d_{14} on an AuFON substrate. While the substrate is exposed to resonant photons, we observed the formation of four distinct, new Raman modes. The Raman signatures had vibrational frequencies of 841, 1133, 1202, and 1588 cm^{-1}. The 841 cm^{-1} vibrational feature is comparably broad, and it is entirely possible that the mode is comprised of two or more overlapped signatures. However, when compared to a previously reported SER spectrum of BPY-d_8,[2] we found that the two spectra were not in agreement. Specifically, the reported SER spectrum did not contain the 841 and 1133 cm^{-1} modes that we observed during the plasmon-mediated reaction of MV-d_{14}. With this comparison, we determined that the photoproduct being produced in the MV-d_{14} exposures, and in the non-deuterated MV studies, was not BPY.

C.4 Benzyl Viologen Kinetic Traces

Below, we have provided the kinetic traces for the 20 studied photochemical reactions of benzyl viologen as it transforms to 4,4’-bipyridine on the surface of the AuFON substrates (**Figures C4-C7**). The five collections for each flux are displayed on the same plot and differ by color. We fit all of the time-dependent data sets to a single exponential function to determine the reaction’s rates. A more detailed discussion on the rates can be found in the main text.

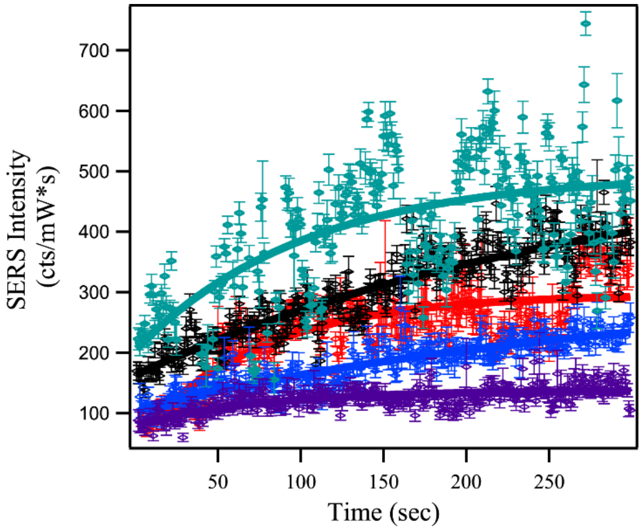

Figure C4. Reaction kinetics of the BV photoproduct’s 1608 cm^{-1} mode during the 5.0 kW/cm^2 flux experiments.

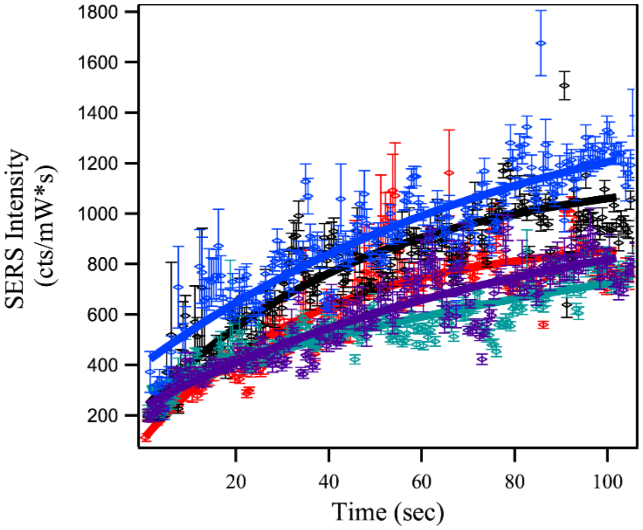

Figure C5. Reaction kinetics of the BV photoproduct's 1608 cm^{-1} mode during the 12.5 kW/cm^{2} flux experiments.

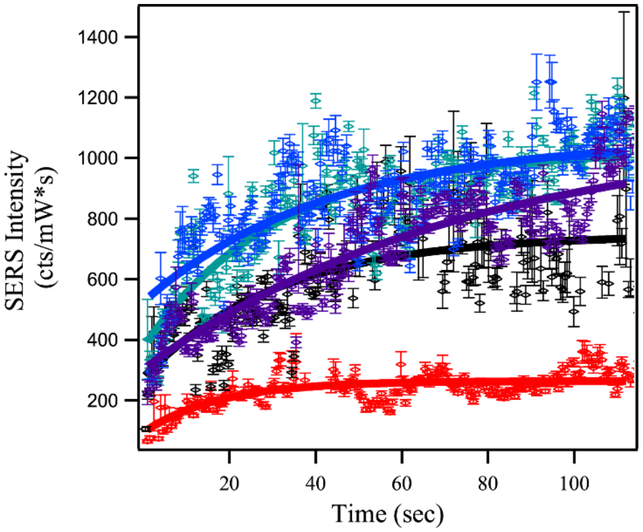

Figure C6. Reaction kinetics of the BV photoproduct's 1608 cm^{-1} mode during the 31.5 kW/cm^{2} flux experiments.

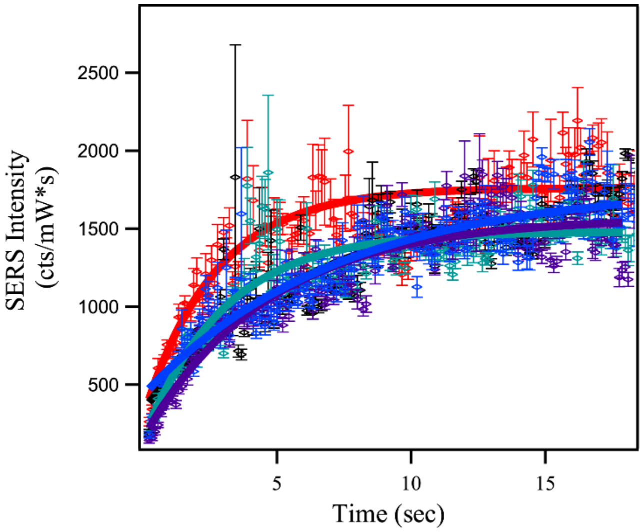

Figure C7. Reaction kinetics of the BV photoproduct's 1608 cm^{-1} mode during the 62.9 kW/cm^2 flux experiments.

C.5 References

(1) Stolberg, L.; Morin, S.; Lipkowski, J.; Irish, D. E., Adsorption of Pyridine at the Au(111)-Solution Interface. *J. Electroanal. Chem.* **1991,** *307* (1-2), 241-262.

(2) Sprague-Klein, E. A.; McAnally, M. O.; Zhdanov, D. V.; Zrimsek, A. B.; Apkarian, V. A.; Seideman, T.; Schatz, G. C.; Van Duyne, R. P., Observation of Single Molecule Plasmon-Driven Electron Transfer in Isotopically Edited 4,4'-Bipyridine Gold Nanosphere Oligomers. *J. Am. Chem. Soc.* **2017,** *139* (42), 15212-15221.

Appendix D

Supporting Information for Chapter 6:

Ultrafast Surface-Enhanced Raman Spectroscopy to Study Hot Electron Transfer in Plasmonic Materials

D.1 Substrate Fabrication for Ultrafast SERS Experiments

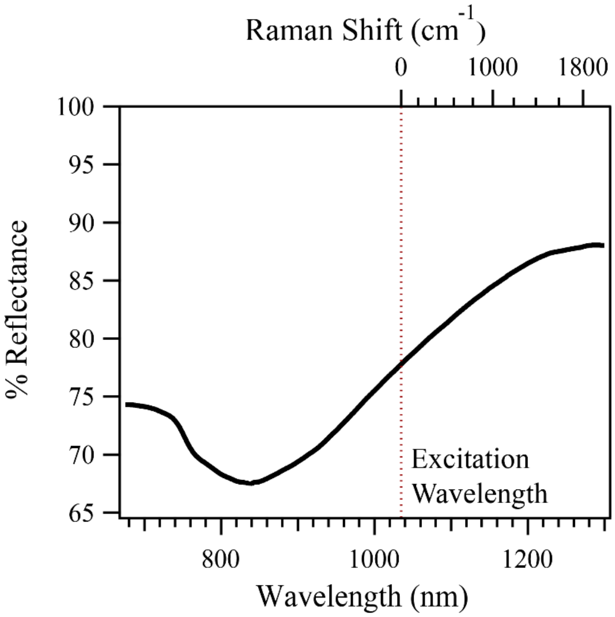

Figure D1. Extinction spectrum of the AuFON substrates. In the ultrafast SERS measurements, we used a 1035 nm excitation source to collect the SERS signal (red dashed line). The top axis displays the corresponding Raman shifts for a 1035 nm excitation.

All of the ultrafast SERS measurements in Chapter 6 were performed with AuFON substrates. We prepared the substrates by slightly modifying previously published procedures.[1-2] We oxygen plasma cleaned glass coverslips (Fisherbrand, 18 mm diameter, 0.13-0.17 thick) to etch the surface for the silica nanosphere deposition. We rinsed the glass coverslips with deionized water both before and after the plasma etching. Then, we displaced the solvent of a stock solution of 600 nm diameter silica microspheres (NanoCym, 10% by volume) with Millipore ultrapure H_2O (18 MΩ). We fabricated other substrates with varying particle sizes, but ultimately, we experimentally found that the 600 nm silica microspheres provided the most intense SERS amplification at 1035 nm excitation. We drop-casted and manually dispersed 3 μL of the silica solution across the surface of the glass coverslip. We allowed the microspheres to dry and they formed into a close-packed monolayer on the surface. Following the application of the silica microspheres, we deposited 200 nm of gold on the silica-coated substrates using a thermal evaporation system (Denton Vacuum, DV-502). We set the instrument to rotate the substrates at 16 rpm during the deposition process.

To quantitatively understand the substrate's localized surface plasmon resonance (LSPR), we measured the extinction spectrum with a UV-2600/2700 equipped with an integrating sphere attachment (Shimadzu). The data acquisition time for each collection was 4 milliseconds. The corresponding extinction spectrum can be found in **Figure D1**. The broad depletion between ~700 to ~1300 nm corresponds to the substrate's LSPR.

D.2 Instrument Response – Optical Kerr Effect Measurements

We characterized the instrument's response by determining the spatial and temporal overlap of the pump and probe pulses. To do so, we found the optimal spatial overlap by aligning the two focused laser beams through a 50-µm pinhole. Additionally, we obtained an accurate temporal overlap by performing an optical Kerr effect (OKE) measurement on cyclohexane with a lock-in amplifier. For this to occur, we set the polarization of the pump beam to a position 45° relative to the probe beam with a λ/2 or λ/4 waveplate (Thorlabs).

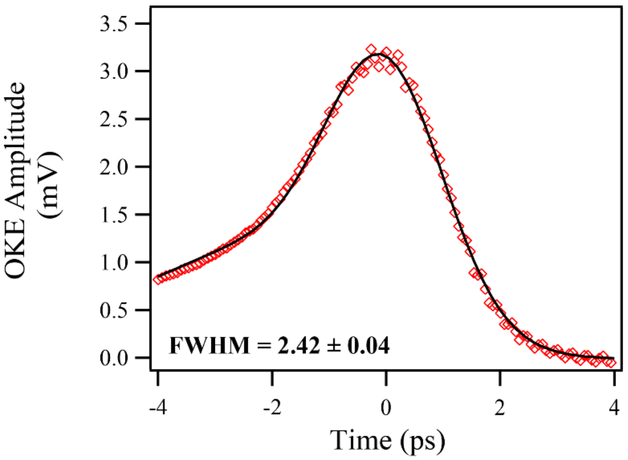

Figure D2. Cyclohexane OKE response on the ultrafast SERS setup. Here, we used a femtosecond pump pulse to optically induce birefringence in the sample and a picosecond probe pulse to measure the transient dynamics. We measured the instrument response, or FWHM, to be 2.42 ± 0.04 ps.

An induced birefringence occurs within a material with a large Kerr constant when the high intensity pump beam is sent through material. This birefringence causes the polarization of the probe beam to be slightly rotated as it passes through the material. We placed a photodiode detector after an optical polarizer to measure the polarization change of the probe beam as the automatic delay stage moved. As an example, we have provided an OKE measurement of the ultrafast apparatus using the standard experimental setup. This measurement can be found in **Figure D2**, and we calculated the corresponding instrument response to be 2.42 ± 0.04 ps.

D.3 References

(1) Dick, L. A.; McFarland, A. D.; Haynes, C. L.; Van Duyne, R. P., Metal Film Over Nanosphere (MFON) Electrodes for Surface-Enhanced Raman Spectroscopy (SERS): Improvements in Surface Nanostructure Stability and Suppression of Irreversible Loss. *J. Phys. Chem. B* **2002,** *106* (4), 853-860.

(2) Greeneltch, N. G.; Blaber, M. G.; Henry, A. I.; Schatz, G. C.; Van Duyne, R. P., Immobilized Nanorod Assemblies: Fabrication and Understanding of Large Area Surface-Enhanced Raman Spectroscopy Substrates. *Anal. Chem.* **2013,** *85* (4), 2297-2303.